MARMARA UNIVERSITY

INSTITUTE FOR GRADUATE STUDIES

REUSE OF SPENT INVESTMENT CASTING FOUNDRY SANDS IN THE PRODUCTION OF STRUCTURAL CERAMICS

CELAL AVCIOĞLU

Ph.D. THESIS

Department of Metallurgical and Materials Engineering

Thesis Supervisor

Prof. Dr. Recep Artır

ISTANBUL, 2023

MARMARA UNIVERSITY

INSTITUTE FOR GRADUATE STUDIES

REUSE OF SPENT INVESTMENT CASTING FOUNDRY SANDS IN THE PRODUCTION OF STRUCTURAL CERAMICS

CELAL AVCIOĞLU

(724715002)

Ph.D. THESIS

Department of Metallurgical and Materials Engineering

Thesis Supervisor

Prof. Dr. Recep Artır

ISTANBUL, 2023

ACKNOWLEDGEMENT

I wish to express my sincere gratitude to Prof. Dr. Recep Artır for his continous support, patience, valuable ideas, useful discussions and constructive suggestions.
I am also extremely greatful to all my family, especially my mother Hülya Avcıoğlu for giving me the opportunities which led me here. Without their support this thesis would not have been possible.

February, 2023 **Celal AVCIOĞLU**

TABLE OF CONTENTS

ACKNOWLEDGEMENT ..... **i**
TABLE OF CONTENTS ..... **ii**
ABSTRACT ..... **v**
CLAIM FOR ORIGINALITY ..... **vi**
SYMBOLS ..... **vii**
ABBREVIATIONS ..... **viii**
LIST OF FIGURES ..... **ix**
LIST OF TABLES ..... **xii**
1. INTRODUCTION **1**
1.1. Objectives of Thesis 2
1.2. Thesis Structure 3
2. LITERATURE REVIEW **4**
2.1 Investment Casting 4
2.2 Mullite Ceramics 6
2.2.1 Reaction synthesis of mullites from industrial wastes 8
2.2.2 Sintering additives for mullite ceramics 10
2.2.3 Mullite-based composites 11
2.3 Cordierite Ceramics 12
2.3.1 Reaction synthesis of cordierite ceramics from industrial wastes 14
2.3.2 Sintering additives for cordierite ceramics 15
2.3.3 Cordierite-based composites 15
3. MATERIALS AND METHODS **18**
3.1 Raw Materials 18
3.2 Fabrication of Ceramic Composites 18
3.2.1 Fabrication of mullite-zirconia composites 19
3.2.2 Fabrication of cordierite-based composites 20
3.3 Characterization Methods 23
4. RESULTS AND DISCUSSION **26**
4.1 Characterization of Investment Casting Shell Waste 26
4.1.1 Particle size distribution analysis 26
4.1.2 Microstructural analysis by SEM 27
4.1.3 Elemental analysis by EDS and XRF 27
4.1.4 XRD analysis 29
4.2 Characterization of Mullite-Zirconia composites 29

4.2.1 XRD analysis 29
4.2.2 Microstructural analysis by SEM 32
4.2.3 Bulk density, apparent porosity, and linear shrinkage 33
4.2.4 Flexural strength 33
4.2.5 Theoretical radiation shielding properties 35
4.3 Characterization of Cordierite-based composites 41
4.3.1 Ceramics Composites Fabricated from CW Without Any Additive 42
4.3.1.1 XRD analysis 42
4.3.1.1 Bulk density, apparent porosity, and linear shrinkage 43
4.3.1.2 Flexural strength 44
4.3.1.3 Microstructural analysis by SEM 45
4.3.2 Cordierite-based composites without any additive 46
4.3.2.1 XRD analysis 46
4.3.2.2 Bulk density, apparent porosity, and linear shrinkage 47
4.3.2.3 Flexural strength 48
4.3.2.4 Microstructural analysis by SEM 49
4.3.3 Influence of La_2O_3 additive 50
4.3.3.1 XRD analysis 50
4.3.3.2 Bulk density, apparent porosity, and linear shrinkage 51
4.3.3.3 Flexural strength 52
4.3.3.4 Microstructural analysis by SEM 53
4.3.4 Influence of Y_2O_3 additive 59
4.3.4.1 XRD analysis 59
4.3.4.2 Bulk density and apparent porosity 60
4.3.5 Influence of Bi_2O_3 additive 61
4.3.5.1 XRD analysis 61
4.3.5.2 Bulk density and apparent porosity 61
4.3.6 Influence of Ta_2O_5 additive 63
4.3.6.1 XRD analysis 63
4.3.6.2 Bulk density and apparent porosity 64
4.3.7 Influence of WO_3 additive 64
4.3.7.1 XRD analysis 64
4.3.7.2 Bulk density and apparent porosity 65
4.3.8 Radiation shielding properties of cordierite-based composites 66
5. CONCLUSION AND FUTURE SUGGESTIONS 88
6. REFERENCES 91

ÖZET

HASSAS DÖKÜM ATIK KUMLARININ YAPISAL SERAMİKLERİN ÜRETİMİNDE KULLANIMI

Hassas döküm yöntemi ile metal ürünlerin artan küresel üretimi, üretimde kullanılan seramik kalıp atıklarının miktarını artırmaktadır. Hassas döküm kalıplarının bertarafı, su ve toprak kirliliği dahil olmak üzere önemli çevresel sorunlara neden olmaktadır. Bu çalışma, hassas döküm kalıp atıklarının yüksek performanslı seramik kompozitlerin üretiminde hammadde olarak kullanımını araştırmaktadır. Öncelikle, hassas döküm kalıp atıkları 63 μm elekten geçebilecek toz haline getirildi. XRD analizi ile atığın büyük oranda, silis, mullit ve zirkondan oluştuğunu saptandı. Atığın elemental bileşimi XRF ve EDS analizleri ile tespit edildi. Elde edilen sonuçlara doğultusunda mullit-zirkonya ve kordierit bazlı kompozitler olmak üzere iki farklı seramik kompozit sistemi formüle edildi. Sinterleme sıcaklığının ve çeşitli metal oksit katkı maddelerinin seramik kompozit sistemlerin sinterlenme ve yoğunlaşma davranlışları üzerindeki etkisi incelendi. Ayrıca, üretilen seramik kompozit sistemlerinin radyasyon kalkanlama özellikleri deneysel ve teorik olarak literatürde ilk defa bu çalışma kapsamında incelendi. 1600°C'de ağırlıkça 1% MgO katkısı ile üretilen müllit-zirkonya kompoziti diğer birçok atık malzemeden hazırlanan mullit seramiklerle karşılaştırılabilir ve hatta onlardan daha iyi olan sırasıyla 190 ve 308 MPa'lık kayda değer bir eğilme ve basma dayanımı değerleri göstermiştir. Ayrıca, bu numune radyasyon kalkanı uygulamaları için umut verici sonuçlar vermiştir. Diğer yandan, ağırlıkça 1% ile 10% oranları arasında değişen Bi_2O_3, La_2O_3, Y_2O_3, Ta_2O_5, and WO_3 olmak üzere beş farklı katkı, kordiyerit esaslı seramik kompozit üretimi için çalışılmıştır. Bu katkılar arasında arasında en iyi radyasyon kalkanlama özelliğini La_2O_3 katkısı sağlamıştır. Bunun nedeni La_2O_3 katkısı ile daha yüksek yığınsal yoğunluk ve daha düşük porozite değerlerinin elde edilmesidir. Bu tez, hassas döküm kabuğu atıklarının hafif, toksik olmayan ve yüksek mukavemete sahip radyasyon kalkanlama malzemelerinin üretiminde hammadde olarak kullanılabileceğini göstermektedir.

Anahtar Kelimeler: Hassas döküm kumu, seramik geri dönüşüm, müllit-zirkonya kompozit, kordiyerit-müllit-zircon kompozit, radyasyon kalkanlama.

Şubat, 2023 **Celal AVCIOĞLU**

ABSTRACT

REUSE OF SPENT INVESTMENT CASTING FOUNDRY SANDS IN THE PRODUCTION OF STRUCTURAL CERAMICS

The growing global production of high-precision metal products via investment casting increases the amount of ceramic shell waste produced. The disposal of investment casting shell waste causes significant environmental issues, including water and soil pollution. The present study assesses the feasibility of investment casting foundry waste as a raw material in producing high-performance ceramic composites. Initially, large chunks of investment-casting foundry waste are processed into powders. XRD analysis revealed that the waste powder mainly comprises silica, mullite, and zircon crystal phases. XRF and EDS analysis were conducted to determine the elemental composition. Then, based on the acquired results, two different ceramic composite systems were formulated, mullite-zirconia composites and cordierite-based composites. The influence of sintering temperature and several additives on sintering behavior, degrees of densification, and radiation shielding performance of the composite systems were investigated.

The mullite-zirconia composite was sintered at 1600°C with 1wt.% MgO presented promising results, with considerable flexural and compressive strength values of approximately 190 and 308 MPa, respectively, which are comparable to or even better than the mullite ceramics prepared from most other waste materials. On the other hand, five different additives, including Bi_2O_3, La_2O_3, Y_2O_3, Ta_2O_5, and WO_3, with concentrations varying from 1 to 10 wt.%, were studied for cordierite-based composites. Among them, the La_2O_3 additive, despite its relatively lower atomic mass, provided the best densification behavior and radiation shielding ability. This thesis demonstrates the possibility of utilizing investment casting shell waste in producing light and non-toxic radiation shielding materials.

Keywords: Investment casting shell waste, foundry sand, mullite-zirconia composite, cordierite-mullite-zircon composite, ceramic recycling, radiation shielding.

February, 2023 **Celal AVCIOĞLU**

CLAIM FOR ORIGINALITY

Although waste disposal-related difficulties cause significant concerns about environmental issues and problems, manufacturing facilities continue to produce/generate an extensive amount of solid waste. Despite that, the foundry industry generates more than 100 million tons of waste foundry sand every year. However, efforts on recycling and reusing investment casting shell waste have been unsuccessful.

This thesis assesses the feasibility of investment casting shell waste as a raw material in producing high-performance ceramic composites. A successful approach has been proposed for fabricating novel ceramic composites from investment-casting shell waste. To the best of our knowledge, investment casting shell waste has not been utilized before to synthesize mullite-zirconia composites with the addition of MgO, TiO_2, and V_2O_5 additives. Meanwhile, investment casting shell waste is again, for the first time, used as a raw material for the fabrication of cordierite-based composites with and without any additives. In this work, the influence of Bi_2O_3, La_2O_3, Y_2O_3, Ta_2O_5, and WO_3 additives on physicochemical and radiation shielding properties of cordierite-based composites investigated. It is also worth mentioning that, the radiation shielding characteristics of investment casting shell waste and composites derived from it were unexplored. This thesis presents a reasonable way to utilize investment casting shell waste to obtain higher value-added products from waste.

I, Celal Avcıoğlu, also declare that this thesis submitted for a doctoral degree at Marmara University is a result of my work. All information derived from other sources has been fully acknowledged. All the work is original, and no part of the work has been taken from elsewhere.

SYMBOLS

ε_r : Dielectric permittivity

ρ : Bulk density

φ : Open porosity

Z_{eff} : Effective atomic number

N_{eff} : Effective electron density

μ : Linear attenuation coefficient

μ/d : Mass attenuation coefficient

ΣR : Fast neutron removal cross section

ABBREVIATIONS

AMW : Average molecular weight

MAC : Mass attenuation coefficient

LAC : Linear attenuation coefficient

HVL : Half value layer

TVL : Tenth value layer

MFP : Mean free path

ACS : Atomic cross section

EABF : Energy absorption buildup factor

EBF : Exposure buildup factor

FNRCS : Fast neutron removal cross section

ST : Sintering Temperature

W : Investment casting shell waste powder

LIST OF FIGURES

Figure 2.1. Investment Casting Process 5
Figure 2.2. Crystal structure of mullite from (a) [001] and (b) [110] directions. 7
Figure 2.3. Alumina-silica phase diagram. 8
Figure 2.4. Crystal structures of the cordierite, (a) orthorhombic system with the *Cccm* No.66 space group and (c) hexagonal system with the *P*6/*mcc* No.192 space group. (b) ordered Si/AlO_4 tetrahedra in among the rings 12
Figure 2.5. Phase diagram of $MgO–Al_2O_3–SiO_2$ ternary system 13
Figure 3.1. Experimental setup for gamma-ray shielding 25
Figure 4.1. Particle size distribution of investment casting shell waste powder. 26
Figure 4.2. Scanning electron microscopy (SEM) images of milled sample 27
Figure 4.3.SEM/EDS Micrographs of the ceramic waste sample showing the Morphology and its chemical composition. 28
Figure 4.4. XRD pattern of investment casting shell waste powder powder. 29
Figure 4.5. XRD patterns of the CW1450, CW1450-T, CW1450-V, and CW1450-M, samples. (★ = zircon, ● = mullite, ▼ = m-ZrO_2, and ☆ = t-ZrO_2) 30
Figure 4.6. XRD patterns of the (a) CW1500-M, (b) CW1550-M, and (c) CW1600-M samples. 31
Figure 4.7. SEM images of the (a, c, d) fractured and (b, d, f) polished surfaces of the (a, b) CW1500-M, (c, d) CW1550-M, and (e, f) CW1600-M samples. 32
Figure 4.8. (a) Linear shrinkage, (b) bulk density, and (c) apparent porosity values of the CW1500-M, CW1550-M, and CW1600-M samples. 33
Figure 4.9. (a) The relative variations of the total cross section for the CW1500-M, CW1550-M, and CW1600-M samples vs. photon energy. The relationship between the photon energy and cross-section of (b) CW1500-M, (c) CW1550-M, and (d) CW1600-M in the energy range from 1 to 10^6 keV 37
Figure 4.10. The relative variations of (a) linear attenuation coefficient and (b) mass attenuation coefficient for the CW1500-M, CW1550-M, and CW1600-M samples vs. photon energy. The insets in (a) show amplified graphs of emphasized regions. 38
Figure 4.11. The relative variations of (a) the mean free path (MFP), (b) half-value layer (HVL), (c) effective atomic number (Zeff), (d) electron density (Neff), (e) energy absorption buildup factor (EABF), and (f) exposure buildup factor (EBF) for the CW1500-M, CW1550-M, and CW1600-M samples vs. photon energy. 39
Figure 4.12.(a) Comparison of the mass attenuation coefficient variations of commonly used radiation shielding materials with CW1600-M (b) The fast neutron removal cross-sections of CW1500-M, CW1550-M, and CW1600-M samples computed using the PhysX software. 41
Figure 4.13. XRD patterns of the W, W-1250, W-1300, and W-1350 samples. (★ = quartz, ● = mullite, ▼ = zircon, ■ = cristobalite, and ◊ = corundum) 42
Figure 4.14. Bulk density, apparent porosity, and linear shrinkage for W-1250, W-1300, and W-1350. 44
Figure 4.15. Flexural strength for W-1250, W-1300, and W-1350. 44
Figure 4.16. SEM images of (a,b) W-1250, (c,d) W-1300, (e,f) W-1350. Inset: EDS results for W-1350. 45
Figure 4.17. XRD patterns of the MAW-1250, MAW-1300, and MAW-1350 samples.

(✦ = cordierite, ● = mullite, ▼ = zircon, ■ = cristobalite, and ◊ = corundum)..... 46
Figure 4.18. Bulk density, apparent porosity, and linear shrinkage for MAW-1250, MAW-1300, and MAW-1350 47
Figure 4.19 Flexural strength for MAW-1250, MAW-1300, and MAW-1350..... 48
Figure 4.20 SEM images of (a,b) MAW-1250, (c,d) MAW-1300, (e,f) MAW-1350. Inset: EDS results for MAW-1350. 49
Figure 4.21. XRD patterns of the MAW-1350 and MAW-La1-10 samples 50
Figure 4.22. Variations of bulk density, apparent porosity, and linear shrinkage as a function of La_2O_3 additive content 52
Figure 4.23. Variations of flexural strength as a function of La_2O_3 additive content 53
Figure 4.24. SEM images of MAW-1350-La1 54
Figure 4.25. SEM images of MAW-1350-La3 55
Figure 4.26. SEM images of MAW-1350-La5 56
Figure 4.27. SEM images of MAW-1350-La7 57
Figure 4.28. SEM images of MAW-1350-La10 58
Figure 4.29. XRD patterns of the MAW-1350 and MAW-Y1-10 samples. 59
Figure 4.30. Variations of bulk density and apparent porosity as function of Y_2O_3 additive content..... 60
Figure 4.31. XRD patterns of the MAW-1300, and MAW-Bi1-10 samples..... 61
Figure 4.32. Variations of bulk density and apparent porosity as a function of Bi_2O_3 additive content..... 62
Figure 4.33. XRD patterns of the MAW-1300, and MAW-1300-La1-Ta1-10 samples .. 63
Figure 4.34. Variations of bulk density and apparent porosity as a function of Bi_2O_3 additive content..... 64
Figure 4.35. XRD patterns of the MAW-1300 and MAW-1300-La1-W1-10 samples.... 65
Figure 4.36. Variations of bulk density and apparent porosity as a function of WO_3 additive content..... 66
Figure 4.37. The relative variations of MAC for the cordierite based composites vs. photon energy. (a) W series, (b) MAW series, (c) MAW with La additive, (d) MAW with Y additive, (e) MAW with Bi additive, (f) MAW with La-Ta additive, (g) MAW with La-W additive, (h) camparison of MAC. 68
Figure 4.38. The relative variations of linear attenuation coefficient for the cordierite based composites vs. photon energy. (a) W series, (b) MAW series, (c) MAW with La additive, (d) MAW with Y additive, (e) MAW with Bi additive, (f) MAW with La-Ta additive, (g) MAW with La-W additive, (g) camparison of LAC..... 70
Figure 4.39. The relative variations of atomic cross section for the cordierite based composites vs. photon energy. (a) W series, (b) MAW series, (c) MAW with La additive, (d) MAW with Y additive, (e) MAW with Bi additive, (f) MAW with La-Ta additive, (g) MAW with La-W additive 72
Figure 4.40 The relative variations of electronic cross section for the cordierite based composites vs. photon energy. (a) W series, (b) MAW series, (c) MAW with La additive, (d) MAW with Y additive, (e) MAW with Bi additive, (f) MAW with La-Ta additive, (g) MAW with La-W additive 73
Figure 4.41. The relative variations of effective atomic number for the cordierite based composites vs. photon energy. (a) W series, (b) MAW series, (c) MAW with La additive, (d) MAW with Y additive, (e) MAW with Bi additive,

(f) MAW with La-Ta additive, (g) MAW with La-W additive 74
Figure 4.42. The relative variations of effective electron density for the cordierite based composites vs. photon energy. (a) W series, (b) MAW series, (c) MAW with La additive, (d) MAW with Y additive, (e) MAW with Bi additive, (f) MAW with La-Ta additive, (g) MAW with La-W additive 75
Figure 4.43. The relative variations of mean free path for the cordierite based composites vs. photon energy. (a) W series, (b) MAW series, (c) MAW with La additive, (d) MAW with Y additive, (e) MAW with Bi additive, (f) MAW with La-Ta additive, (g) MAW with La-W additive 77
Figure 4.44. The relative variations of half-value layer (HVL) for the cordierite based composites vs. photon energy. (a) W series, (b) MAW series, (c) MAW with La additive, (d) MAW with Y additive, (e) MAW with Bi additive, (f) MAW with La-Ta additive, (g) MAW with La-W additive, (g) camparison of HVL. 78
Figure 4.45. The relative variations of tenth-value layer (TVL) for the cordierite based composites vs. photon energy. (a) W series, (b) MAW series, (c) MAW with La additive, (d) MAW with Y additive, (e) MAW with Bi additive, (f) MAW with La-Ta additive, (g) MAW with La-W additive. 79
Figure 4.46. A comparative presentation of the fast neutron removal cross-sections of W- and MAW-series samples. 81
Figure 4.47. A comparative presentation of the fast neutron removal cross-sections of La containing samples. 81
Figure 4.48. A comparative presentation of the fast neutron removal cross-sections of Y containing samples. 82
Figure 4.49. A comparative presentation of the fast neutron removal cross-sections of Bi containing samples. 82
Figure 4.50. A comparative presentation of the fast neutron removal cross-sections of La-W containing samples. 83
Figure 4.51. A comparative presentation of the fast neutron removal cross-sections of La-Ta containing samples. 83
Figure 4.52 Comparative values of linear attenuation coefficients calculated with experimental and computational data. (a) W-1350, (b) MAW-1350, (c) MAW-1350-Y10 and (d) MAW-1350-La10 86
Figure 4.53 Comparative values of mass attenuation coefficients calculated with experimental and computational data. (a) W-1350, (b) MAW-1350, (c) MAW-1350-Y10 and (d) MAW-1350-La10 87
Figure 4.54 The I/I0 and shielding percent values of the samples 87

LIST OF TABLES

Table 3.1. Batch compositions of ceramic bodies for mullite/zirconia composites and their sintering temperatures..... 20
Table 3.2. Batch compositions of ceramic bodies and their sintering temperatures..... 22
Table 4.1. The mechanical properties of mullite/zirconia composites prepared in this work and different mullites reported in the literature. 34
Table 4.2. Sample codes, measured density, the weight fraction of constituent compounds 36
Table 4.3. Experimental gamma shielding results of selected ceramics for Ba133-1, Ba133-2, and Cs-137 radioactive sources..... 84
Table 4.4. Experimentally obtained linear attenuation coefficient (μ) values of selected ceramics..... 84
Table 4.5. Experimentally obtained mass attenuation coefficient (μ/d) values of selected ceramics..... 85

1. INTRODUCTION

The booming global economy and fierce industrial competition have led to severe environmental deterioration and the unsustainable exploitation of natural resources. To achieve a greener and sustainable economy, shifting toward sustainable production patterns with low ecological footprints is essential. In this regard, developing efficient reuse and recycling systems is of vital importance. Investment casting, also known as lost wax casting, is one of the most widely used manufacturing processes of high-precision metal components. The process relies on hollow ceramic shell molds for molten metal to be poured in and solidified. After solidification, ceramic shell molds are broken off, and the casted metals are collected [1]. Accordingly, the investment casting industry generates millions of tons of ceramic shell mold waste every year and requires special attention [2]. Although valuable constituents such as silica, mullite, and zircon, the vast majority of waste ceramic shell molds are being disposed to landfills while the rest is being used as a road pavement subgrade which does not capture the full value of this material; therefore, developing an economically feasible recycling process that brings value to this material and returns it to the economy is highly desirable.

The use of radiation in a wide range of applications, such as nuclear power generation, security, healthcare, agriculture, space exploration, geology, and aerospace, is rapidly increasing. Radiation can be described as energy or particles that emanate from one source and travels through space at the velocity of light, and can penetrate materials. Radiation can be useful, but it is also extremely dangerous for the environment and potentially fatal to living beings [3]. Therefore, radiation shielding materials are commonly placed between a radiation source and the target to reduce the impact of the radiation. Materials composed of a large atomic number of elements are commonly used for radiation attenuation. Owing to its large atomic number of 82 and good gamma attenuation ability, Lead (Pb) is the most commonly employed radiation shielding material [4,5]. Gamma rays (direct ionizing radiation) and neutrons (indirect ionizing radiation) are the most common types of radiation discussed in the literature [6–8]. Nevertheless, metallic lead exhibits considerably low neutron absorption ability and has poor mechanical strength. Furthermore, it is extremely toxic to living beings and the environment. Therefore, there is a growing demand for cheap, environmentally friendly, reliable materials. Other large atomic number elements such as tungsten and bismuth containing materials have also

been recently explored as efficient materials for radiation shielding [4]. Furthermore, these materials can be dispersed in structural ceramics to obtain desired shapes and mechanical properties. Besides, adding various metal oxides into ceramic matrixes can also boost their densification behavior, mechanical properties, and radiation shielding performance.

1.1. Objectives of Thesis

The investment casting industry produces a high amount of solid foundry waste. Recycling of these wastes is challenging and requires multiple separation and purification processes. Despite these costly processes, investment casting shell molds produced from recycled raw materials may not provide the properties required for investment casting. Therefore, investment-casting foundry wastes are usually sent to landfills. The primary goal of this study is to bring value to investment casting foundry waste.

Initially, large pieces of investment casting foundry waste material obtained from a local investment casting plant are processed into powders and then characterized. XRD results showed that investment casting foundry waste is mainly composed of mullite, silica, and zircon, and XRF analysis revealed elemental composition. Then, considering the crystalline phase and elemental composition of the investment casting foundry waste material, two major aims are determined.

- Utilization of investment casting shell waste as a raw material in producing high-performance mullite/zirconia composites as structural materials for radiation shielding applications.
- Utilization of investment casting shell waste as a raw material in producing high-performance cordierite/mullite-based composites as structural materials for radiation shielding applications.

Objectives regarding the former aim are listed below,

- Complete dissociation of zircon from investment casting foundry waste into silica and zirconia
- Investigating the influence of MgO, TiO_2 and V_2O_5 additives on zircon dissociation
- Determination of batch composites for the conversion of both free silica from investment casting foundry waste and silica from zircon dissociation into mullite

- To obtain proper microstructural development, i.e., cross-linked mullite grains to improve mechanical properties
- Optimization of process parameters to enhance physicochemical and radiation shielding properties.

Objectives regarding the latter aim are listed below,

- Determination of batch composites for the conversion of the free silica from investment casting foundry waste into cordierite
- Determination of sintering additives and their concentration to attain improved densification behavior and radiation shielding properties.
- Optimization of process parameters to enhance physicochemical and radiation shielding properties.

1.2. Thesis Structure

This thesis is structured as follows: First, the investment casting process and investment casting shell waste are briefly introduced. Second, various properties of mullite and cordierite ceramics are discussed. Experimental procedures for developing ceramic composites and the methodology are given in the next section. Afterward, characterization data for the investment casting shell waste are presented. Crystal phase analysis results, radiation shielding, and physicochemical properties for the mullite-zirconia composites and cordierite-based composites are discussed in sections 4.2 and 4.3, respectively. Finally, the main conclusions discussed and perspectives for future research are highlighted.

2. LITERATURE REVIEW

2.1 Investment Casting

Investment casting (lost wax casting), which can be traced back to 5000 B.C., is a commonly used process for producing complex-shaped ferrous and non-ferrous materials with excellent surface finish. This method is employed to fabricate a wide range of industrial and consumer products, including turbine blades, machine, and engine parts, implants, jewelry, artwork, etc. The fundamental steps of investment casting processes are depicted in Figure 2.1. In the first step of the investment casting process, molten wax is injected into a metallic die to create a wax pattern of the required shape. The pattern is then confined to a central wax sprue, along with a group of similar patterns [9]. To create a shell around the wax design, ceramic or refractory slurry is coated onto the stimulated pattern and solidified. The pattern is then melted out of the shell. The ceramic shell is then sintered to attain sufficient strength that can withstand the molten metal. Following that, molten metal is poured into the robust refractory shell and then solidified. Finally, the shell is fractured to obtain near-net shape solidified casting [10].

The proper processing in each investment casting process, including the formation of wax patterns, construction of ceramic shells, dewaxing and sintering of the ceramic shells, and pouring of the molten metal into the shells, determines the accuracy and precision of the casting components [11]. Some other process variables also influence the accuracy and precision of the final product. A Particular factor is the type and properties of the investment casting mold. Indeed, the chemical composition of the ceramic shell, firing temperature, duration, and surface smoothness directly impact the finished part's dimensional accuracy and strength. Several layers of ceramic coatings are put on to the pattern tree assemblages or pattern clusters to form investment shell molds. Each coating layer comprises fine ceramic particles embedded in "stucco" (coarse ceramic particles). A crucial step in the ceramic shell-forming process is the application of the primary refractory slurry to the pattern assembly's surface to capture its surface details. It should exhibit a smooth surface so the casting component can have an acceptable surface finish. Although expensive, zircon powder is employed in the primary refractory slurry. Nevertheless, some cheap filler materials can be added to the primary refractory slurry to reduce its cost. To obtain a homogeneous coating layer, the tree assembly or cluster is

initially submerged in primary refractory slurry, with any excess slurry then drained off. To ensure that the casting has an excellent surface quality, the initial coating layer is typically composed of fine powers.

The moist coating layer is then quickly covered by coarser ceramic particles, either through submerging it in a fluidized bed of the particles or sputtering. The inner layer of the investment casting shell molds is made of a fine ceramic particle that can replicate every small feature, including the pattern's smooth surface. It is also worth mentioning that a small amount of bonding agent is usually added into the slurry to attain strength to the investment casting shell molds. The applied outer layer of coarse stucco particles also provides structural integrity to the investment casting shell molds [13].

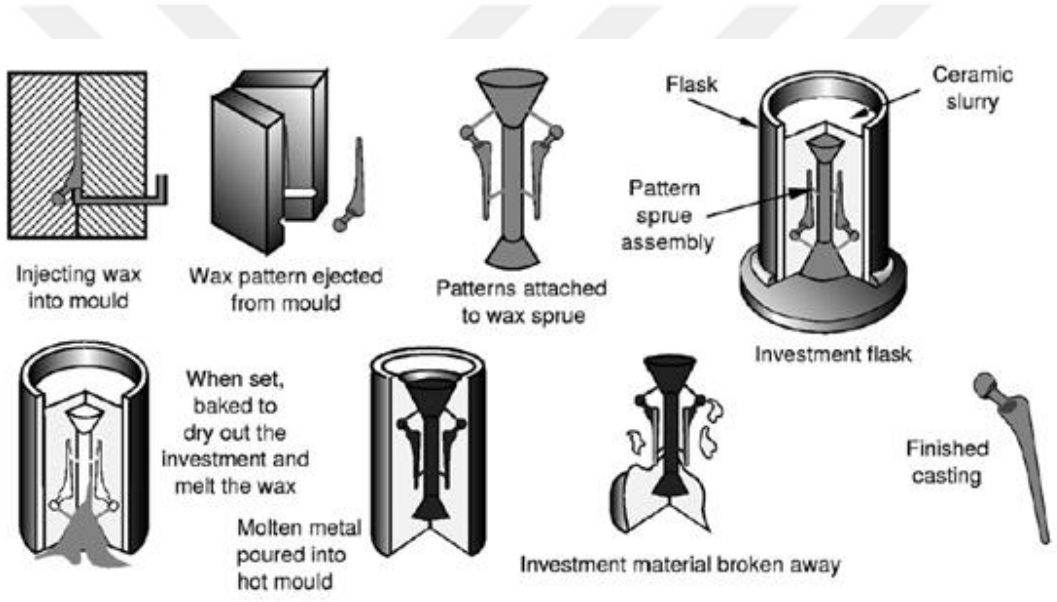


Figure 2.1. Investment Casting Process [12].

A particular challenge in this process is to provide sufficient bonding between individual coating layers and rapidly enlarging shell thickness. Therefore, each coating should be hardened before applying the follow-up coating layer. Drying, chemical gelling, or combining these methods can achieve this. Up until the desired shell thickness is reached, the coating, stuccoing, and hardening processes are repeatedly carried out. The number of coating layers in the shell typically ranges from five to eight, depending on the necessary cooling speed as well as the type of casting component. To prevent the appearance of loose particles on the surface of the shell mold, the last coat, which is frequently referred to as a seal coat, is left unstitched. The chemical composition of the

refractory slurry, fabrication procedure, sintering temperature, and duration influences ceramic shell quality. Typically, dewaxed refractory shell molds are fired at 1000°C to withstand the molten metal pouring process mechanically. Commonly utilized refractories for slurry and stucco in the fabrication of investment casting molds include silica, zircon, alumina, and different aluminum silicates such as mullite [14]. For example, molochite, a calcined clay at about 1500°C, is the standart refractory material used in the fabrication of investment casting ceramic shells. Molochite typically supplies about 55% mullite and 45% silica but it may also contain small amounts of TiO_2 and Fe_2O_3.

Despite high cost of production and valuable refractory components, investment casting shell molds are only one-time use items [15]. Indeed, after the metal casting and solidification processes, they are broken off and discarded. Therefore, the main waste generated from the whole investment casting process is the used refractory shell molds with about almost 60% of all wastes.

2.2 Mullite Ceramics

Mullite is an important phase of the SiO_2–Al_2O_3 binary system owing to its high melting point (1840℃), low thermal expansion coefficient ($6 \cdot 10^{-6}$/°C), low density (3.20 g/cm^3), good thermal shock and creep resistance, high corrosion resistance, and chemical stability[16]. Therefore, mullite ceramics are commonly used in structural and functional applications such as refractories, catalysts, catalytic supports, membranes, and radiation shielding [17–21].

The crystal structure of mullite is comprised of edge-sharing AlO_6 octahedra chains, which are parallel to the c-axis. Meanwhile, $(Al,Si)O_4$ tetrahedra units bridge AlO_6 octahedral chains, as seen in Figure 2.2.

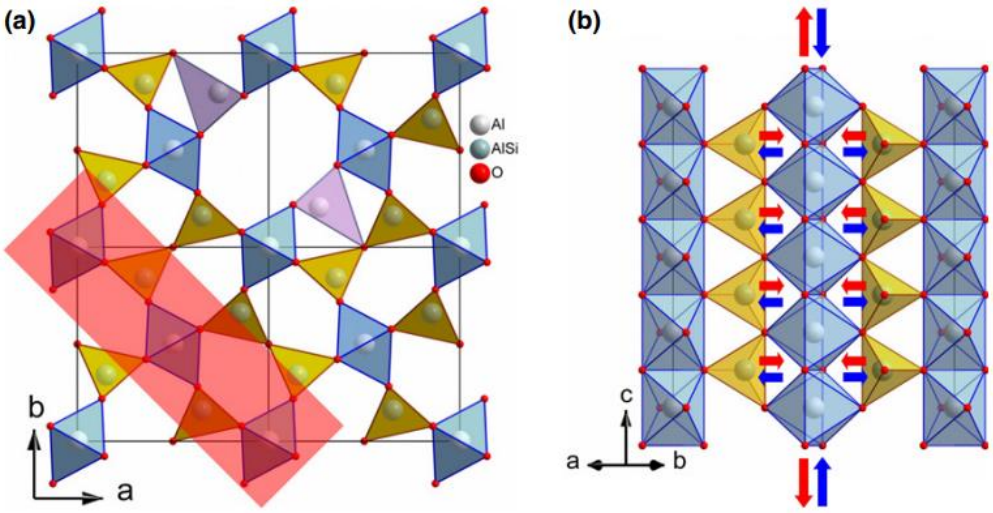


Figure 2.2. Crystal structure of mullite from (a) [001] and (b) [110] directions.[16]

One important feature of mullite is its compositional flexibility originating from its (Al,Si)O4 units. Figure 2.3 depicts the Al_2O_3-SiO_2 phase diagram. It can be seen that mullite phases boundary at 1800°C corresponds to 77.2 wt.% Al_2O_3 and 22.8 wt.%SiO_2 indicating a chemical formula of $2Al_2O_3SiO_2$. $2Al_2O_3SiO_2$. This composition of mullite is known as 2:1 mullite. Nevertheless, with decreasing temperature from 1800°C to 1620°C and below, the silica content in the mullite increases and chemical compositions shift to $3Al_2O_3{\cdot}2SiO_2$, and this composition of mullite is known as 3:2 mullite and stoichiometric mullite.

Mullites are not so abundant in nature. Therefore, they are synthesized artificially. Various methods have been developed for mullite ceramics, such as sintering of green bodies of mullite powders, reaction sintering of alumina and silica-containing raw materials, reaction bonding and transient viscous sintering [22].

Nevertheless, reaction synthesis is the most common route to mullite ceramics. In this process, mullite formation reaction among silica and alumina regents and the densification of green compacts simultaneously occurs. Industrial-grade regents are commonly employed for this process. On the other hand, several studies have been conducted to reduce the fabrication cost of mullite ceramics by utilizing industrial wastes.

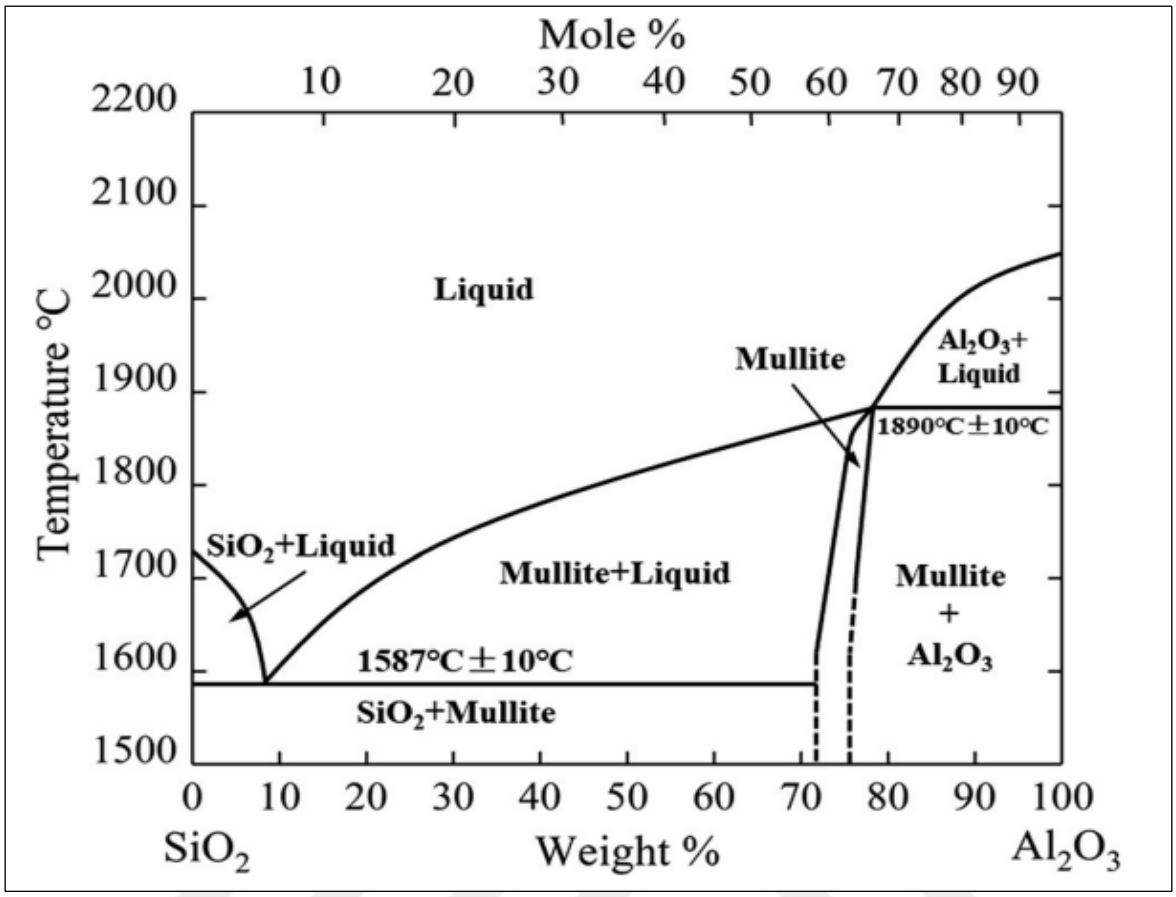


Figure 2.3. Alumina-silica phase diagram.

2.2.1 Reaction synthesis of mullites from industrial wastes

Hitherto, wastes such as aluminum sludge, aluminum dross, metakaolin, coal fly ash, rice husk, waste glasses, and slate waste have been used as raw materials for mullite synthesis. [23] For example, coal fly ash is an abundant byproduct of thermal power plants and contains a large amount of silica. Therefore, comprehensive studies have been conducted on mullite production from coal fly ash using it as a silica source. Generally, researchers have reaction sintered coal fly ash with alumina sources such as alumina, aluminum dross, aluminum hydroxide, and bauxite at elevated temperatures (>1500°C) [22,24,25]. Bauxite was the most commonly used alumina source due to its low cost. However, it is worth noting that mullite ceramics produced from coal fly ash usually exhibited high porosity and low mechanical properties. For example, mullite ceramics obtained by reaction synthesized at 1500°C from the mixture of alumina and coal fly ash only exhibited 63% of theoretical density [22]. In another study, Dong et al.[26] demonstrated that mullite ceramics fabricated from a dry-pressed mixture of coal fly ash and bauxite at

1550°C had about 44% open porosity and flexural strength of 65 MPa. Due to their porous nature, mullite ceramics produced from coal fly ash usually employed for membrane applications [27,28].

Aluminum sludge is a by-product of waste water treatment plants. When wastewater contains aluminum-based salts, a large amount of aluminum sludge can be obtained. For example, wastewater from aluminum anodizing, cutting and polishing, and surface coating processes might yield a large amount of aluminum sludge. It is mostly made up of 80% water and aluminum hydroxides. Nevertheless, upon heating at high temperatures, it yields α-alumina and γ-alumina. Riberio et al.[21] showed that mullite ceramics could be obtained from mixtures of aluminum sludge and various low-cost silica sources, including ball clay, kaolin, and diatomite. It has been observed that palletization starts at 1250°C, but temperatures higher than 1450°C were required to produce single-phase mullite ceramics. Besides, Al-rich sludge waste has been combined with various silica-containing wastes such as soda lime, pyrex waste, and slate waste to produce mullite ceramics [29,30]. Choo et al.[23] suggested that the benefits of employing aluminum sludge as a raw material for mullite synthesis include its fine particulate sizes and high aluminum hydroxide content which is comparatively less thermally stable than other aluminum sources. Thereby, aluminum sludge can easily mix and react with silica components during the reaction sintering process.

Waste from cutting and polishing processes in slate quarries is referred to as slate. The main slate components of the wastes are mud-like lubricants, water, and broken slate rock. Although it is mainly composed of alumina and silica, it may also contain other oxide compounds such as iron, titanium, magnesium, calcium, sodium, potassium, and manganese oxides. Therefore, it has been considered a potential raw material for mullite synthesis [31]. It is worth noting that the silica content of slate waste is usually higher than its alumina content. Therefore, it needs to be added with an additional alumina source. For example, Oliveira et al.[32] synthesized 2:1 mullite ceramics by reaction sintering slate waste with fine alumina powders at 1450°C. In addition to the wastes mentioned above, several other wastes, including schist, glass, kaolin, sago, and silica fume, have also been employed in mullite synthesis [33–37]. However, it is worth noting that the mechanical strength of mullite ceramics fabricated from industrial wastes was generally lower than those synthesized from reagent-grade raw materials [23].

2.2.2 Sintering additives for mullite ceramics

It is widely acknowledged that mullite formation reaction among silica and alumina precursors starts at around 1000°C, and the mullite content in the final ceramic increases with increasing sintering temperature. For instance, Sembiring et al.[35] demonstrated that mullite phase content increases from 31 wt.% to 68 wt.% when the sintering temperature was increased from 1150°C to 1350°C.

On the other hand, sintering temperatures typically higher than 1450°C are required to obtain single-phase mullite ceramics. Nonetheless, a sintering temperature above 1600°C is necessary to obtain fully dense mullite ceramics [38].

The rationale for using sintering additives is to decrease the formation temperature of mullite, improve densification, proper microstructural development and enhance the mechanical strength of the sintered mullite ceramics. Indeed, sintering additives such as TiO_2, Y_2O_3, MgO, La_2O_3, CaF_2, H_3BO_3, Na_2SO_4, MoO_3, and boehmite have been reported to decrease the mullite formation temperature and improve the densification [23,39,40].

For example, Souto et al.[40] reported that the addition of 1 wt.% MgO increased the relative density from 65% to 97% for mullite ceramics sintered at 1500°C. In another study, Viswabaskaran et al.[39] showed that adding 2 wt.% MgO enhances the density from 2.69 to 2.82 $g \cdot cm^{-3}$ for mullite ceramics sintered at 1500°C. Meanwhile, 5 wt.% Y_2O_3 or boehmite were required to achieve similar degrees of densification. Poor sinterability of mullite originates from low interdiffusion rates of Si^{2+} and Al^{3+} ionic components in the lattice. These additives form liquid phases during the sintering and enhance the diffusion rates and densification. One important note is that sintering aids also increase the glassy phase content in the matrix. Therefore, the amount of sintering aid should be kept minimum to suppress the loss in the mechanical properties [41].

Of further note, sintering aids can also be used for microstructural development. Indeed, the mechanical properties of mullite ceramics can be improved via self-strengthening through microstructure tailoring, in which columnar grains with interlocking structures are attained during synthesis. Several studies demonstrated that cross-linked mullite grains could be obtained by adding various sintering additives such as CeO_2 and Cr_2O_3, La_2O_3, MgO, and Y_2O_3 [42–44].

2.2.3 Mullite-based composites

Typically, mullite ceramics already suffer from low bending strength and fracture toughness at room temperature. To overcome this drawback, mullite matrices are commonly reinforced with second-phase enhancers such as carbon fiber, Al_2O_3, ZrO_2, B_4C Al_2O_3, SiC, TiC, WC, etc [45–50]. Among them, mullite-zirconia composites are extensively used in the industry. The addition of zirconia into the mullite matrix enhances thermo-mechanical properties such as high hardness and melting point, wear resistance, and elastic modulus. The enhancement in the mechanical properties can be ascribed to multiple mechanisms, stress-induced phase transformation leading to lattice expansion, microcrack toughening, crack deflection, and bowling [49,51].

Ample studies have been conducted on fabricating zirconia-dispersed mullite composites from a comprehensive library of raw materials. Early work on zirconia-mullite was devoted to the sintering of mullite and zirconia mixtures and the reaction sintering of alumina, silica, and zirconia. Nevertheless, recent studies focussed on zircon ($ZrSiO_4$) as a zirconia and silica source because it costs much less than zirconia [52,53]. This reaction relies on the dissolution of zircon into silica and zirconia. Then, the revealed silica reacts with alumina to yield mullite, as shown in the equation below.

$$2ZrSiO_4+3Al_2O_3 \rightarrow 2ZrO_2+3Al_2O_3 \cdot 2SiO_2 \quad (2.1)$$

It has been reported that the dissociation of zircon into ZrO_2 and SiO_2 starts at 1673±10ºC [54]. Nevertheless, the presence of impurities may promote zircon dissociation at lower temperatures [54–56]. For example, Kim Hwan demonstrated that zircon does not dissociate at 1550ºC but adding 5 wt.% alumina provides slight dissociation [57].

Therefore, researchers could obtain mullite-zirconia composites from alumina and zircon at lower temperatures. For example, Garrido et al.[58] reported mullite-zirconia composites from compacted alumina and zircon powder mixture through reaction sintering at temperatures ranging from 1450 to 1600°C. Additionally, the MgO additive was also found to promote zircon dissociation. Prusty et al.[43] observed that the MgO additive not only enhances zircon decomposition but also stabilizes the zirconia in the cubic phase and results in the formation of cross-linked mullite grains; both are beneficial for mechanical properties.

2.3 Cordierite Ceramics

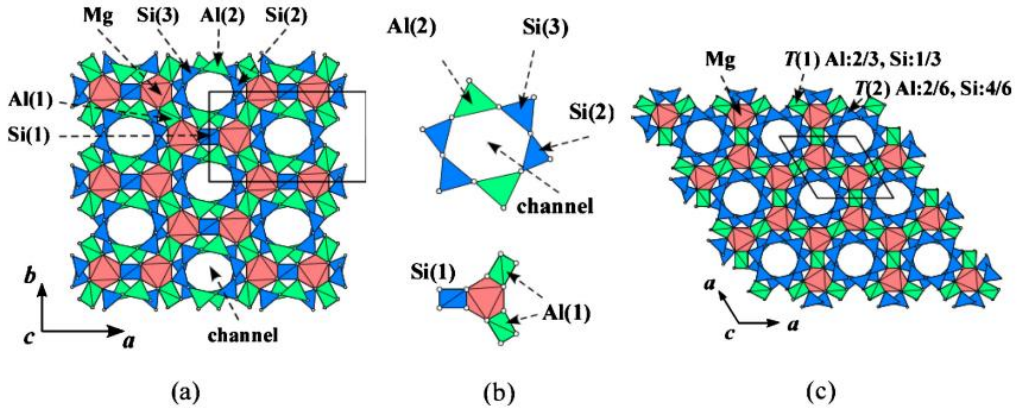


Figure 2.4. Crystal structures of the cordierite, (a) orthorhombic system with the *Cccm* No.66 space group and (c) hexagonal system with the *P*6/*mcc* No.192 space group. (b) ordered Si/AlO_4 tetrahedra in among the rings [59].

Cordierite with the $Mg_2Al_4Si_5O_{18}$ chemical formula has two stable polymorphs, high-temperature α-cordierite, and low-temperature β-cordierite. β-cordierite crystallizes in the orthorhombic structure and is stable at temperatures lower than 1450°C. On the other, α-cordierite, the high-temperature stable phase, crystallizes in a higher-symmetry hexagonal structure. Most ceramics used in the industry are β-cordierite, and its crystal structure is composed of six-membered hexagonal rings of [$(Si_4Al_2)O_{18}$] units linked by MgO6 octahedrons. Meanwhile, SiO4 tetrahedrons and AlO4 tetrahedrons connect the hexagonal rings in a way to form two structural cavities per formula, which are perpendicular to the c-axis, as demonstrated in Figure 2.4 [59].

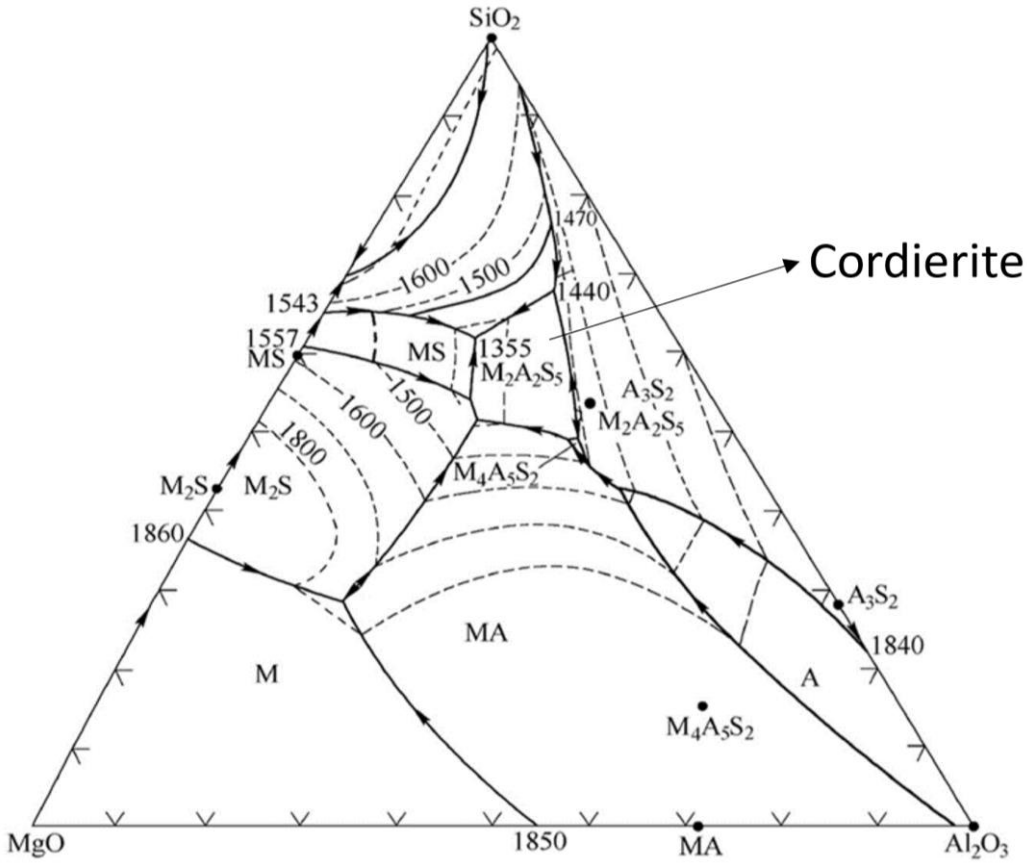


Figure 2.5. Phase diagram of $MgO–Al_2O_3–SiO_2$ ternary system.[63]

Cordierite is a well-known structural ceramic in the $MgO–Al_2O_3–SiO_2$ ternary system (Figure 2.5) with a wide range of applications due to its excellent thermal shock resistance, chemical durability, low thermal expansion coefficient ($0.7*10^{-6} K^{-1}$, 25-1000^{o}C), and dielectric permittivity ($\varepsilon_r \approx 4$ at 1 MHz).[32,60,61] Due to these characteristics, cordierite ceramics are commonly used as refractories in kilns and furnaces, catalytic converters in exhaust systems, electro-ceramics, integrated circuit boards, membranes, and tableware. Nevertheless, despite its wide use, cordierite rarely occurs in nature. Therefore, most cordierite used in the industry is produced synthetically. Although several methods have been developed for cordierite syntheses, such as solid-state reaction, sol-gel and glass crystallization, solid-state reaction proved to be the most economical way. In this respect, reaction sintering natural raw materials containing oxides of MgO, Al_2O_3, and SiO_2 is often conducted for cordierite production. Commonly used raw materials are the clay, talc, kaolin, alumina, silica sand, feldspar, and quartz. For example, kaolinite and clay can serve as Al_2O_3 and SiO_2 sources, and talc provides MgO and SiO_2 [62].

2.3.1 Reaction synthesis of cordierite ceramics from industrial wastes

Several industrial wastes have been used as raw materials to fabricate cordierite ceramics, such as serpentine, kiln rollers, kaolin waste, waste aluminum sludge, fly ash, aluminum slag, and silica fume waste. Most of these wastes generally served as Al_2O_3 or SiO_2 resources. Contrarily, Aşkın et al.[64] recently utilized the waste magnesite powder as a magnesia source for the synthesis of cordierite ceramics. It is well known that a large amount of waste magnesite powder is generated during magnesite processing. Quartz and kaolin were other raw materials, and samples were sintered at different temperatures ranging from 1250-1325ºC. Nevertheless, sintering temperatures below 1325ºC did not yield single-phase cordierite. The sample sintered at 1325ºC was also highly porous; its porosity and bulk density were 1.64 g/cm^3 and 36.5%, respectively. In another study, Almedia et al.[65] investigated kaolin waste's feasibility in synthesizing cordierite. A dry pressed mixture of kaolin waste, talc, and magnesium oxide powders reaction sintered at temperatures from 950 to 1350ºC. However, cordierite phase formation was only observed at temperatures above 1250ºC.

On the other hand, Hajjou et al.[66] could observe the cordierite phase formation from fly ash, magnesium chloride, and silica gel raw materials at 1200°C. However, the sample also contained several secondary phases, including mullite, cristobalite, silicon oxide, enstatite, and spinel. Pure phase cordierite in this study could only be obtained at 1350ºC. Recently, Khattab et al.[67] used calcined alumina, fine amorphous silica fume, and talc powder mixtures to prepare cordierite ceramics. Similar to the abovementioned study, high-purity cordierite samples could only be obtained at sintering temperatures above 1350ºC. The sample sintered at 1350ºC exhibited 0.323% apparent porosity and 2.112 g/cm^3 bulk density. Its fracture toughness and microhardness were 71 MPa m0.5 and 5.38 GPa, respectively.

Further, Wang et al.[68] prepared cordierite ceramic from fly ash, quartz, and magnesite at 1300 °C with an open porosity of 33.16% and a bulk density of 1.61 g/cm^3. Considering its low density, it exhibited fairly good mechanical properties with a compressive strength of 72.64 MPa and flexural strength of 23.92 MPa.

2.3.2 Sintering additives for cordierite ceramics

It is worth noting that obtaining high-density cordierite ceramics with good-phase purity is challenging. The problem arises from its narrow sintering temperature. Indeed, as discussed in the previous section, sintering temperatures higher than 1300°C are often required to obtain single-phase cordierite ceramics. Still, the melting temperature of cordierite is just 1455°C, and impurities lower this temperature. Hence, the sintering temperature cannot be increased significantly to improve its density. Several attempts have been made to decrease the sintering temperature of cordierite ceramics to overcome this drawback. This is also beneficial for reducing production costs.

Different sintering additives such as TiO_2, Bi_2O_3, B_2O_3, P_2O_5, CeO_2, and K_2O have been reported beneficial to improve the sintering ability of cordierite ceramics.[69–72] For example, adding a small amount of TiO_2 density of cordierite ceramics could be enhanced over ~98% at 1350°C [72] . This value is even higher than the relative theoretical density of 94% for cordierite. Obradovic et al.[69] reported that adding Bi_2O_3 is also beneficial for lowering the sintering temperature. This was because of the low melting temperature of Bi_2O_3 (850 °C), resulting in liquid-phase sintering. Meanwhile, Wu et al.[73] investigated the influence of B_2O_3 and P_2O_5 additives on cordierite formation and suggested that B_2O_3 promotes the formation of high-temperature α-cordierite, whereas P_2O_5 promotes the β-cordierite. Besides, the addition of 4 wt.% CeO_2 was found to promote the conversion of cristobalite to cordierite and suppress the spinel phase formation resulting in a less glassy phase in the cordierite matrix [71].

The influence of excess MgO on the fabrication of cordierite ceramics from waste foundry sand was also investigated [74]. The waste foundry sand was composed mainly of Al_2O_3, SiO_2, and $ZrSiO_4$. Therefore, it was added with MgO powders and fused silica to yield a stoichiometric cordierite phase based on the XRF results. The addition of excess MgO improved the densification behavior considerably. More importantly, the cordierite formation temperature of this system was only 1150°C; this was ascribed to the acceleration effect of $ZrSiO_4$ in the waste foundry sand.

2.3.3 Cordierite-based composites

The main advantages of cordierite are its low thermal expansion coefficient and excellent thermal shock resistance. Nonetheless, cordierite ceramics exhibit relatively poor

mechanical properties. Dispersion of second-phase enhancers into the cordierite matrix has been widely used to alleviate this drawback. For example, dispersing 25 wt.%ZrO_2 into cordierite matrix composites with 25 wt.% ZrO_2 into the cordierite matrix improved fracture strength and toughness from 140 to 290 Mpa and 1.6 to 3.5 Mpa·$m^{1/2}$, respectively.[75] Such enhancements were expected as ZrO_2 exhibit much higher strength than cordierite. In addition, the martensitic transformation toughening effect of the ZrO_2 particles also played a part in the performance enhancement.

Cordierite–zircon ceramic composites fabricated from commercial cordierite powder with 2.5 wt.% zircon resulted in a 30% enhanced flexural strength than pure cordierite ceramics [76] . The flexural strength was about 84±7 MPa. Furthermore, it was revealed that zircon addition also enhances the sintering behavior of cordierite ceramics by forming a liquid phase.

Although mullite has a high-temperature mechanical strength it exhibits low thermal shock resistance due to its high thermal expansion coefficient. Therefore, mullite ceramics have commonly been combined with cordierite for a wide variety of applications ranging from traditional refractories to functional and structural ceramics. Cordierite-mullite composites are currently employed in several commercial applications, such as kiln furniture and catalytic converters [77].

In this way, the mechanical properties of the cordierite can also be improved. Khattab et al.[78] several cordierite-mullite composites with varying cordierite phase concentrations from 50 to 100 wt.% and investigated their physical and mechanical properties. Waste silica fume, calcined ball clay, magnesia, and calcined alumina were used as raw materials and samples were sintered at three different temperatures, 1350, 1400, and 1450°C. XRD results revealed that 1400°C was optimum for producing cordierite-mullite composites through reaction sintering. Additionally, among the synthesized samples, the one containing 70 wt.% cordierite and 30 wt.% mullite exhibited the best mechanical properties. Cold-crushing strength and apparent porosity were about 490 Mpa and 11.5%, respectively. Recently, Brito et al.[79] investigated the formulations based on various low-cost raw materials, including kaolin residue, talc, and magnesium hydroxide, for the fabrication of cordierite-mullite composites. XRD investigations showed that both cordierite and mullite phases were observed as low as 1250°C and 1300°C. Among the different formulations, composites prepared from the richest Al_2O_3 and SiO_2 sources

increased the mullite and cordierite phases content. Nevertheless, the mechanical strength of the composites was better when the MgO content in the formulations was increased [80].

3. MATERIALS AND METHODS

3.1 Raw Materials

This thesis investigates the usability of investment casting foundry sand in the production of structural ceramic composites. The spent investment casting shell waste used in this project comes as large chunks from a local investment casting plant of Marmara province in Turkey. The obtained investment shell waste were ground to a coarse powder for the preparation of a feed for further processing and characterizations. Initially, ceramic waste were crushed into small pieces. Due to the brittle nature of the spent investment shell waste, a manual hammer was employed. In order to generate a suitable feed for the following grinding phase, the size of crushed raw material initially determined by 1mm sieve. The waste that had not been filtered via the sieve was collected and returned to the crushing stage. This process repeated until all the waste material passed the sieve. The second step of raw material preparation was to reduce the size of the ceramic waste from 0-1.00 mm to less than 63 μm. This was necessary for further processing and materials characterization steps. This was accomplished by using a mortar grinder. The size of ground ceramic waste powders were verified by using a 63 μm sieve. Like the crushing process, up until all of the ceramic waste materials passed the 63 m sieve, the grinding operation was repeated. Thereafter, the obtained spent investment casting foundry sand will be denoted as W for convenience.

In addition to the W, high purity alumina (Al_2O_3, Merck, 45 μm mean particle size and ≥99.9% purity), magnesia (MgO, Merck, 10 μm mean particle size and ≥99% purity), lanthanum oxide (La_2O_3, Schuchardt München, ≥99.9% purity) tungsten oxide (WO_3, Roth, ≥99.5% purity) bismuth oxide (Bi_2O_3, Heraeus ≥99.8% purity), yttrium oxide (Y_2O_3, Merck, ≥99% purity) and tantalum oxide (Ta_2O_5, Alfa Aesar, ≥99% purity) are used to make various of mullite and cordierite based composites or employed as additives. Besides, polyvinyl alcohol and stearic acid, which serve as a binder and internal lubricant, were used in the preparation of the green bodies.

3.2 Fabrication of Ceramic Composites

Firstly, ceramic composites from W without any additive are fabricated by the conventional ceramic method. Then, two types of composites from W with various

additives were prepared, mullite-zirconia composites and cordierite-based composites. The following subsections describe the prepared batches' chemical compositions and fabrication methods in detail.

3.2.1 Fabrication of mullite-zirconia composites

Mullite-zirconia composites were synthesized by the ceramic route as follows. To obtain 3:2 mullite ($3Al_2O_3 \cdot 2SiO_2$) in the final composite, W powder and Al_2O_3 were proportioned in mass ratios of 100:82. In this way following reactions may occur:

$$2SiO_2+3Al_2O_3 = Al_6Si_2O_{13} \quad (3.1)$$

$$2ZrSiO_4 +3Al_2O_3 = 2ZrO_2+Al_6Si_2O_{13} \quad (3.2)$$

The aforementioned raw materials were weighed regarding the mass ratio, to which 1 wt. % MgO is added as a sintering additive. The powder mixture was mixed in distilled water via a planetary ball mill at a speed of 400 rpm for 2 h using a zirconia jar and high-purity alumina grinding media. This method was chosen to obtain homogenous mixtures rather than particle size reduction. The obtained mixture was dried overnight at 80°C and crushed in an agate mortar with a pestle. Afterward, the obtained powder mixture was mixed with both 1% wt—polyvinyl alcohol and stearic acid, which serve as a binder and internal lubricant, respectively. First, PVA was dissolved in distilled water at 70°C and stirred for 20 minutes before being added to the powder mixture and continued the stirring process for 2 h, then dried overnight at 70°C and crushed in an agate mortar with pestle. The same procedure was applied for stearic acid, but acetone was used as a solvent. Rectangular (50 mm x 20 mm x 8 mm), disc-shaped (12 mm x 5 mm), and cubic (12mm x 12 mm x 12 mm) green bodies obtained by uni-axial pressing by applying a pressure of 200 Mpa, followed by debinding at 500°C for 2 h with the heating rate of 2°C min-1 in an electrical furnace. Then, the sintering process was conducted in air at temperatures of 1500°C, 1550°C, and 1600°C. The heating and cooling rate was 5°C min^{-1}, and the dwelling period at the maximum temperature was 4 h.

Besides, green bodies with 1 wt.% MgO, TiO_2 or V_2O_5 additives prepared and sintered at 1450°C to determine an efficient additive for zircon decomposition. For convenience, the obtained samples were denoted as W1450, W1450-M, W1450-T, W1450-V, W1500-M,

W1550-M, and W1600-M based on their sintering temperatures and aid, i.e., W1450-M and CW1450 represent the samples synthesized at 1450°C with and without MgO additive, respectively. Batch compositions of ceramic bodies for mullite/zirconia composites and their sintering temperatures are given in Table 3.1.

Table 3.1. Batch compositions of ceramic bodies for mullite/zirconia composites and their sintering temperatures

Sample	Sintering Temperature (°C)	Composition (wt.%)				
		W	Al_2O_3	MgO	TiO_2	V_2O_5
CW1450	1450	54.9	45.1	-	-	-
CW1450-M	1450	54.4	44.6	1	-	-
CW1450-T	1450	54.4	44.6	-	1	-
CW1450-V	1450	54.4	44.6	-	-	1
CW1500-M	1500	54.4	44.6	1	-	-
CW1550-M	1550	54.4	44.6	1	-	-
CW1600-M	1600	54.4	44.6	1	-	-

3.2.2 Fabrication of cordierite-based composites

Firstly, ceramic composites from W without any additive have been prepared for comparison as follows. W was mixed with both wt. 1%—polyvinyl alcohol and stearic acid serve as a binder and internal lubricant, respectively. First, PVA was dissolved in distilled water at 70°C and stirred for 20 minutes before being added to the powder mixture and continued the stirring process for 2 h, then dried overnight at 70°C and crushed in an agate mortar with pestle. The same procedure was applied for stearic acid, but acetone was used as a solvent. Rectangular (50 mm x 20 mm x 8 mm) and disc-shaped (12 mm x 5 mm) green bodies were obtained by uni-axial pressing by applying a pressure of 200 Mpa, followed by debinding at 500°C for 2 hours with the heating rate of 2°C min^{-1} in an electrical furnace. Then, the sintering process was conducted in air at 1250°C, 1300°C, and 1350°C for 3 hours. The heating and cooling rate was 5°C min^{-1}. The obtained samples were denoted as W-1250, W-1300, and W-1350 based on their sintering temperatures.

Cordierite-based composites were synthesized by the ceramic route as follows. Cordierite-based composites were formulated using W, alumina, and magnesia. All the free silica in the investment casting shell waste powder aimed to be converted into cordierite based on the equation 3.1:

$$Al_2O_3\,(s) + MgO\,(s) + SiO_2\,(s) \rightarrow Mg_2Al_4Si_5O_{18}\,(s) \qquad (3.3)$$

To this end, W, alumina, and magnesia with a 100 : 17.7 : 9.8 wt. ratio was thoroughly mixed by planetary ball mill for 2 h in an alumina jar and high-purity alumina grinding media. Then, the obtained mixture was dried overnight at 80°C and crushed in an agate mortar with a pestle. Afterward, rectangular (50 mm x 20 mm x 8 mm) and disc-shaped (12 mm x 5 mm) green bodies were prepared by uni-axial pressing by applying a pressure of 200 MPa. As above, the prepared green bodies were sintered at 1250°C, 1300°C and 1350°C for 3 h. These samples are denoted as MAW-1250, MAW-1300, and MAW-1350 based on their sintering temperatures.

Additionally, 25 samples with five different additives, Bi_2O_3, La_2O_3, Y_2O_3, Ta_2O_5, and WO_3, and with concentrations varying from 1 to 10 wt.%, was mixed with the above composition for making different batches. The samples containing Y_2O_3 and La_2O_3 as a main additive sintered at 1350°C while others sintered at 1300°C for 3 h. Besides, 1 wt.% La_2O_3 was used as a sintering aid when Ta_2O_5 and WO_3 were used as primary additives. Batch compositions of ceramic bodies and their sintering temperatures are presented in Table 3.2.

Table 3.2. Batch compositions of ceramic bodies and their sintering temperatures

Sample	ST (°C)	Composition (wt.%)							
		W	Al_2O_3	MgO	Bi_2O_3	Y_2O_3	La_2O_3	Ta_2O_5	WO_3
W-1250	1250	100	-	-	-	-	-	-	-
W-1300	1300	100	-	-	-	-	-	-	-
W-1350	1350	100	-	-	-	-	-	-	-
MAW-1250	1250	78.4	13.9	7.7	-	-	-	-	-
MAW-1300	1300	78.4	13.9	7.7	-	-	-	-	-
MAW-1350	1350	78.4	13.9	7.7	-	-	-	-	-
MAW-1300-Bi1	1300	77.7	13.7	7.6	1	-	-	-	-
MAW-1300-Bi3	1300	76.1	13.5	7.5	2.9	-	-	-	-
MAW-1300-Bi5	1300	74.7	13.2	7.3	4.8	-	-	-	-
MAW-1300-Bi7	1300	73.3	13	7.2	6.5	-	-	-	-
MAW-1300-Bi10	1300	71.3	12.6	7	9.1	-	-	-	-
MAW-1300-Y1	1350	77.7	13.7	7.6	-	1	-	-	-
MAW-1300-Y3	1350	76.1	13.5	7.5	-	2.9	-	-	-
MAW-1300-Y5	1350	74.7	13.2	7.3	-	4.8	-	-	-
MAW-1300-Y7	1350	73.3	13	7.2	-	6.5	-	-	-
MAW-1300-Y10	1350	71.3	12.6	7	-	9.1	-	-	-
MAW-1300-La1-W1	1300	76.9	13.6	7.5	-	-	1	-	1
MAW-1300- La1-W3	1300	75.4	13.3	7.4	-	-	1	-	2.9
MAW-1300- La1-W5	1300	74	13.1	7.2	-	-	1	-	4.7
MAW-1300- La1-W7	1300	72.6	12.9	7.1	-	-	0.9	-	6.5
MAW-1300- La1-W10	1300	70.7	12.5	6.9	-	-	0.9	-	9
MAW-1300- La1-Ta1	1300	76.9	13.6	7.5	-	-	1	1	-
MAW-1300- La1-Ta3	1300	75.4	13.3	7.4	-	-	1	2.9	-
MAW-1300- La1-Ta5	1300	74	13.1	7.2	-	-	1	4.7	-
MAW-1300- La1-Ta7	1300	72.6	12.9	7.1	-	-	1	6.5	-
MAW-1300- La1-Ta10	1300	70.7	12.5	6.9	-	-	1	9	-
MAW-1350- La1	1350	77.7	13.7	7.6	-	-	1	-	-
MAW-1350- La3	1350	76.1	13.5	7.5	-	-	2.9	-	-
MAW-1350- La5	1350	74.7	13.2	7.3	-	-	4.8	-	-
MAW-1350- La7	1350	73.3	13	7.2	-	-	6.5	-	-
MAW-1350- La10	1350	71.3	12.6	7	-	-	9.1	-	-

3.3 Characterization Methods

This section describes the experimental methods and analytical techniques used to determine the characteristics of both raw materials and sintered ceramics.

X-Ray Diffraction (XRD) is a commonly employed technique for identifying and quantifying crystalline phases of substances. Crystalline materials, contrarily to amorphous ones, are composed of atoms arranged in systematic three-dimensional arrays. They are ordered in a way that forms a string of parallel planes that are spaced apart at certain distances. The distance between such planes is unique for each crystalline phase and can be used as a fingerprint for phase identification. Generally, when a concentrated monochromatic X-ray beam strikes a material's surface with a certain angle, atomic layers will cause them to scatter in various directions. The crystal structure can be identified by analyzing the X-ray diffraction patterns. Here, the phase compositions of samples were analyzed by XRD method by using a D8 Advance X-ray diffractometer (Bruker, Germany) with CuKα radiation ($\lambda = 1.5406$Å). Analysis were performed in the 2θ range of 10–70° with a step size of 0.1° and time intervals of 8s. The elemental composition of the investment casting shell waste was analyzed using an XRF spectrometer (Rigaku, Japan). The XRF analysis was conducted under an air atmosphere, and a 10 mm collimator was used. Particle size distribution of the investment casting shell waste powder was measured using a laser diffraction particle size analyzer. At the same time, they were dispersed in pure water. The compression and three-point bending tests were conducted in a RetroLine testing machine (Zwick/Roell) using cube (10mm x 10 mm x 10 mm) and bar (20mm x 8 mm x 8 mm) shaped gently polished sintered samples, respectively, and a cross head speed of 0.5 mm/min applied. Three replicas of each sample were tested, and their average values were obtained. The microstructural analysis was performed from polished or fractured surfaces of samples upon a 3-Point bending test using scanning electron microscopy (Quanta Feg 250, FEI, USA).

The bulk density and apparent porosity of sintered ceramic composites were determined by the Archimedes method, based on the ASTM C-373-18. Initially, dry weights ($\mathbf{W_d}$) of samples were measured before Archimedes experiment. Afterward, samples were boiled in water at 120°C for 4 h until the open porosity were filled with water. Then, their suspended weights ($\mathbf{W_s}$) were measured while the sample was in the water. Lastly, they were removed from the water, and their surface water was cleaned with paper towels

before being weighted to determine their saturated weights (**W_m**).

The bulk density (ρ) of samples was determined by the following equation;

$$\rho = \frac{W_d}{W_m - W_s} \tag{3.4}$$

The open porosity (φ) was determined by the following equation;

$$\varphi = \frac{W_m - W_d}{W_m - W_s} \tag{3.5}$$

Linear shrinkage of samples was measured by measuring the largest side of the rectangular (50 mm x 20 mm x 8 mm) ceramic bodies before and after sintering using a digital micrometer. Then, the linear shrinkage is determined using following equation.

$$\text{Linear shrinkage } (\%) = \frac{d_0 - d_f}{d_0}\ 100 \tag{3.6}$$

Where, d_0 and d_f are the diameters of samples before and after sintering.

The linear mass attenuation coefficient of the ceramic composites was determined using a home-made gamma-ray shielding experimental setup from Yildiz Technical University, Physics department. The experimental setup is shown in Figure 3.1. It contains a NaI (Tl) scintillation detector with a 3 × 3 inches diameter and a photomultiplier tube. The resolution of the NaI (Tl) crystal is approximately 7% at a photon energy of 662 keV for ^{137}Cs, and the light decay time constant is approximately 0.23 μs. Experiments were carried out from disc-shaped samples with 1.2 cm diameter and varying thicknesses from 0,5318 to 0,627. Samples were placed in front of the collimated γ-rays from ^{133}Ba, ^{137}Cs, and ^{60}Co radioactive point sources. The linear mass attenuation coefficients of the samples were determined for two energy lines for ^{133}Ba (81 keV and 356 keV) and ^{60}Co (1173 keV and 1332 keV) sources and another one for the 137Cs (662 keV) source. Each measurement was performed three times for 20 min, and their average values were obtained. The statistical error was lower than 2%. Furthermore, EpiXS and PhyX/PSD programs were used to explore the radiation shielding ability of manufactured ceramics theoretically. Relevant information on the computation methods can be found in literature [81,82].

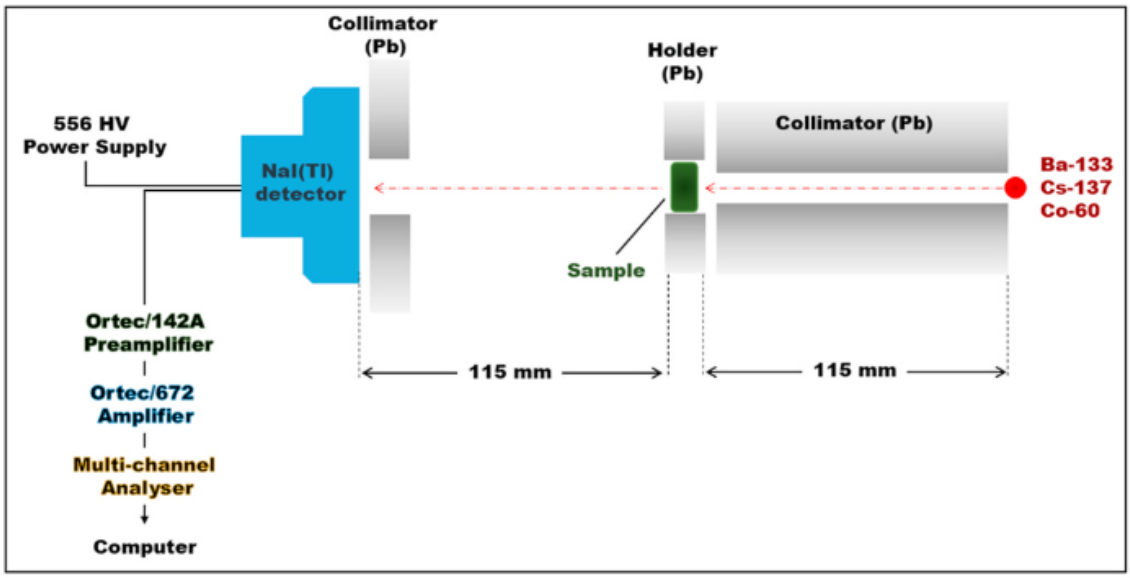


Figure 3.1. Experimental setup for gamma-ray shielding [83].

4. RESULTS AND DISCUSSION

4.1 Characterization of Investment Casting Shell Waste

This chapter presents the material characterization data for W, supplied by a local investment casting plant. All characterization was performed from ground and screened (63 μm sieve) W powders.

4.1.1 Particle size distribution analysis

The particle size distribution of the W powder was determined by laser diffraction technique as described in section 3. The median particle size (D50), As shown in Figure 4.1, were less than 23.74 μm. Meanwhile, 90% of the particles (D90) were smaller than 55 μm whereas 10% of the particles smaller than 3.1 μm. The maximum particle size was aproximately 91 μm. These findings imply that the powder was reasonably fine and acceptable for preliminary chemical and physical analysis.

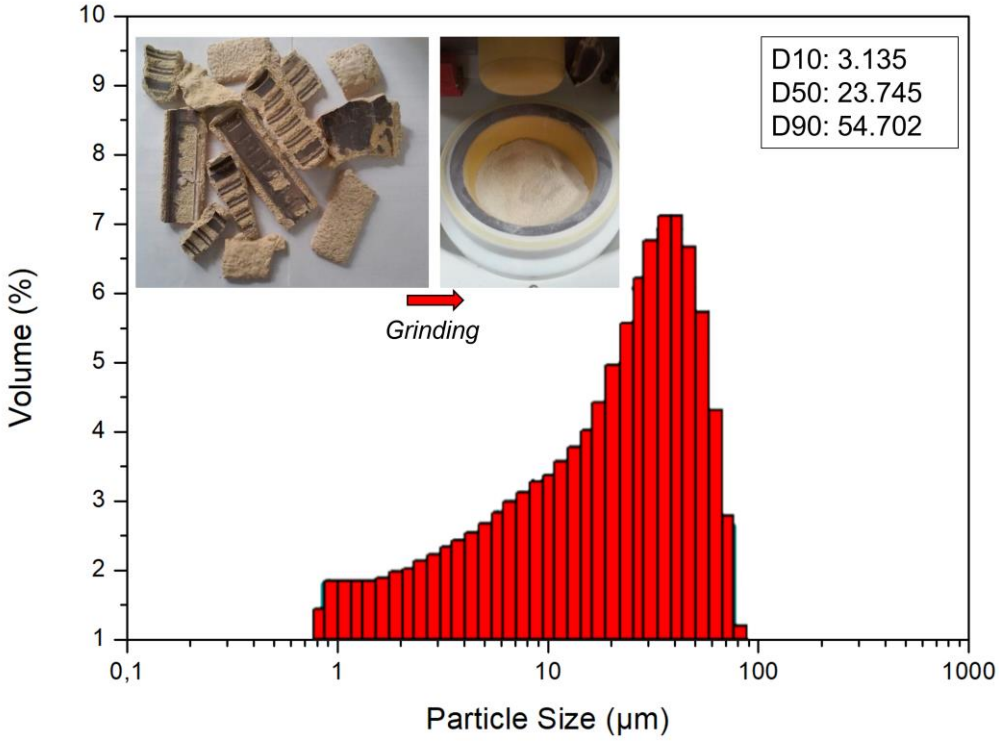


Figure 4.1. Particle size distribution of investment casting shell waste powder.

4.1.2 Microstructural analysis by SEM

A secondary electron image obtained by scanning electron microscopy (SEM) of ceramic waste foundry powder is given in Figure 4.2. The image of the sample shows that particles have angular and complex shaped morphology. Even if it is difficult to calculate and compare the powders' average particle size and particle size distribution from SEM micrographs without using computing software. According to the SEM observations, the powders have wide grain size distribution and are in the range of 1μm to 100 μm, consistent with particle size measurement results.

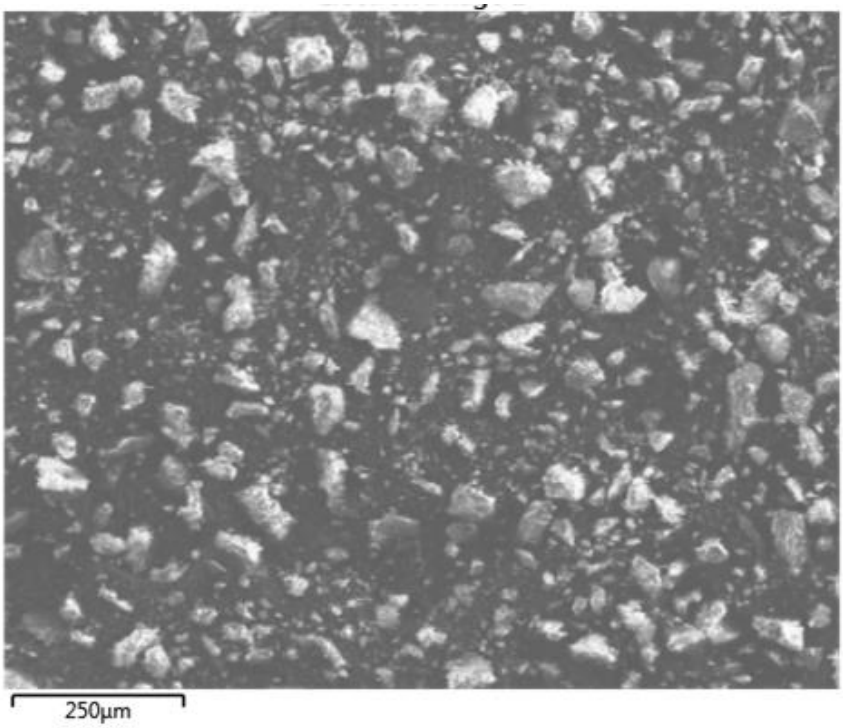


Figure 4.2. Scanning electron microscopy (SEM) images of milled sample

4.1.3 Elemental analysis by EDS and XRF

Figure 4.3 shows the result of the EDS analysis for the ceramic waste sample. It displays chemical compositions at both for mapping and selected locations. Meanwhile, Tablo 4.1 shows the elemental composition determined by the EDS analysis.

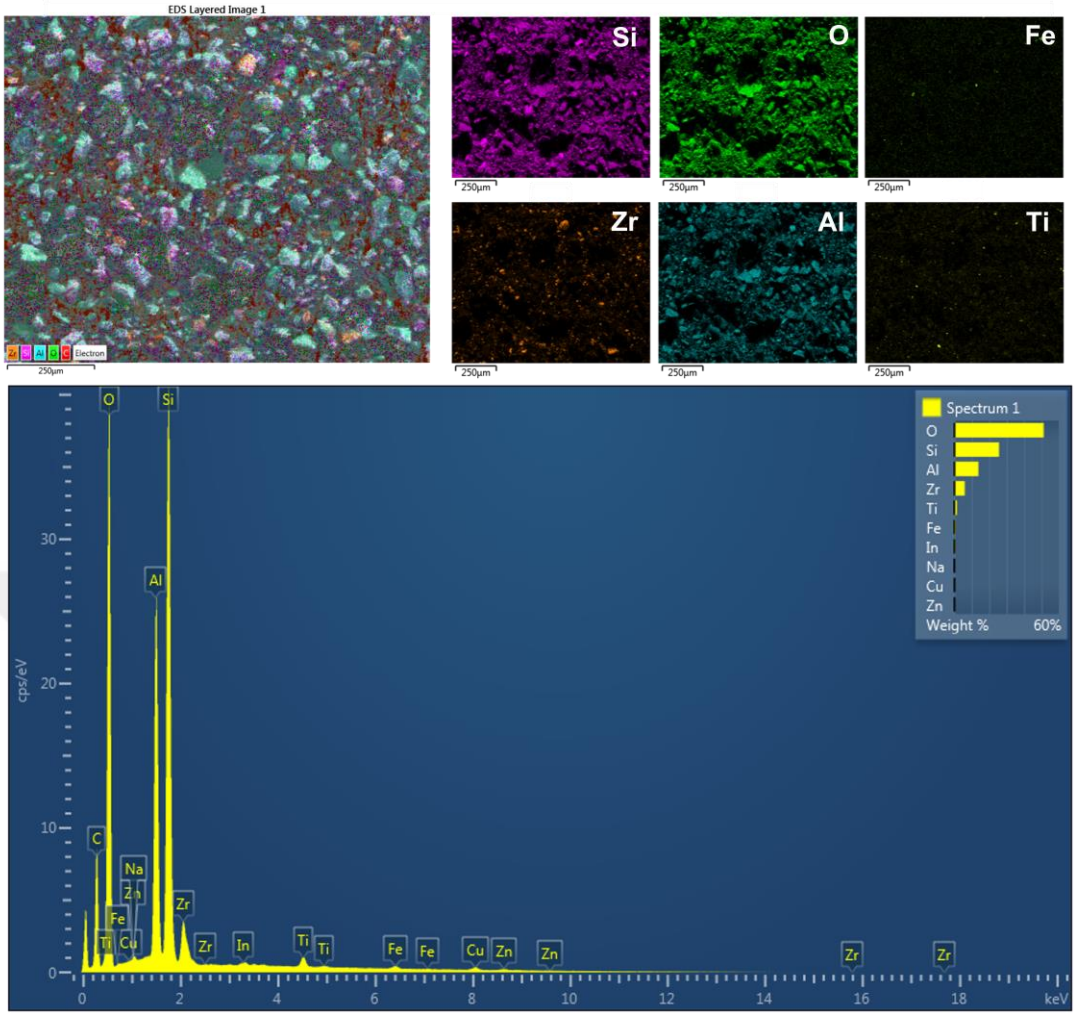


Figure 4.3. SEM/EDS Micrographs of the ceramic waste sample showing the Morphology and its chemical composition.

Tablo 4.1 Elemental composition (wt.%) of investment casting shell waste powder using EDS.

O	NA	Al	Si	Ti	Fe	Cu	Zn	Zr	In
51.27	0.20	13.86	25.60	1.47	0.86	0.13	0.12	5.97	0.50

Tablo 4.2 Chemical composition (wt.%) of investment casting shell waste powder using XRF.

CO_2	Na_2O	Al_2O_3	SiO_2	P_2O_5	K_2O	CaO	TiO_2	Fe_2O_3	Sr	Zr	Nb
0.33	0.16	21.83	40.76	0.13	0.25	0.20	2.41	0.44	0.05	9.66	0.02

The chemical compositions of the investment casting shell waste powder as determined

by XRF (Rigaku RSX, Japan) are listed in Tablo 4.2. EDS and XRF results are in good accord and indicates that W is mainly consists of silicon, aluminum, and zirconium. Besides, a small amount of titanium and iron elements are also notable.

4.1.4 XRD analysis

The crystalline phases present in the W powder were determined by X-ray diffraction technique. The results of XRD are in good agreement with those of XRF. As shown in Figure 4.4. XRD pattern of investment casting shell waste powder. the major crystalline phases in W were quartz (SiO_2), cristobalite (SiO_2), mullite ($Al_6Si_2O_{13}$), and zircon ($ZrSiO_4$).

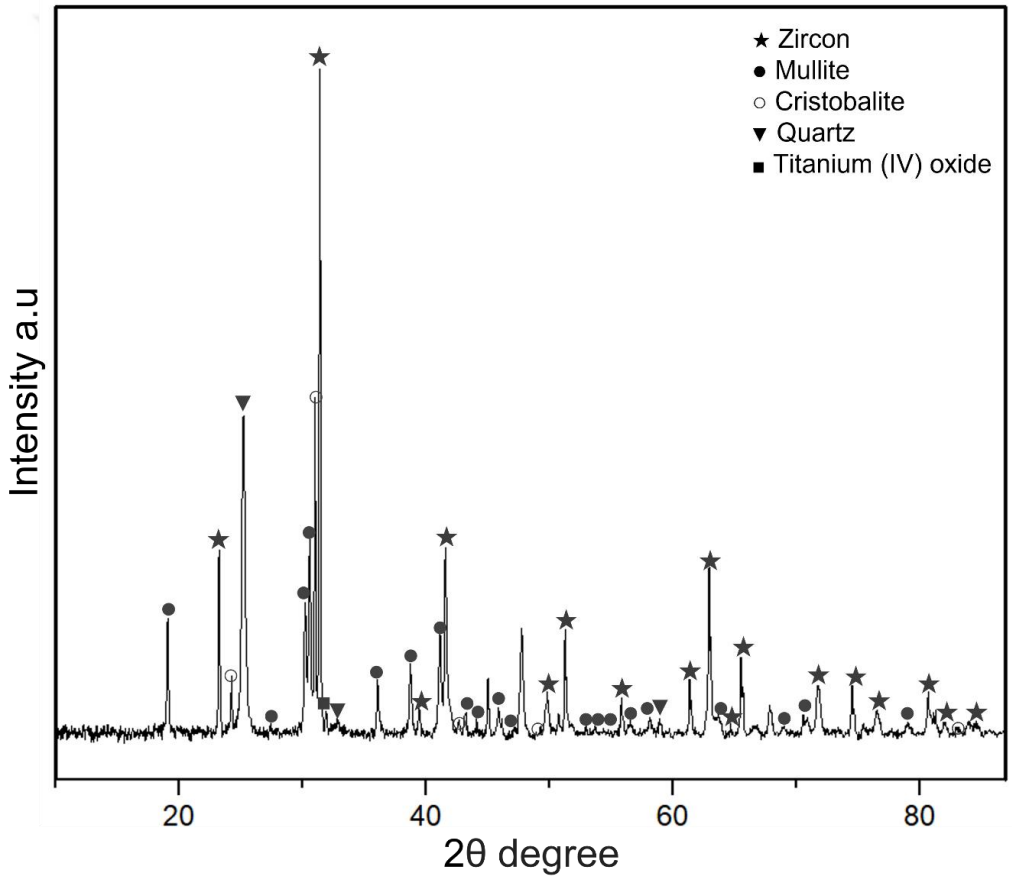


Figure 4.4. XRD pattern of investment casting shell waste powder.

4.2 Characterization of Mullite-Zirconia composites

4.2.1 XRD analysis

To determine an efficient additive for zircon dissociation, the phase compositions of four

samples sintered at 1450°C were analyzed, one without any additive and three with 1 wt% MgO, TiO_2, or V_2O_5 additives. As seen in Figure 4.5a, the sintered sample without using any additive is composed of mullite and zircon ($ZrSiO_4$) phases. No additional peaks and no zircon dissociation was observed for CW1450-T, CW1450-V samples. Contrarily, zircon dissociation was observed in MgO containing sample, evidencing that the mullite formation reactions among the silica and alumina in the starting materials have been completed after the heat treatment at 1450°C. It has been widely stated that the dissociation of zircon into ZrO_2 and SiO_2 starts at 1673±10ºC, yet there is no consensus on this temperature [54]. Besides, the presence of impurities may promote zircon dissociation at lower temperatures [54–56]. Nevertheless, despite the presence of TiO_2, and V_2O_5 additives for the sample sintered using 1% wt MgO additive, four phases belonging to mullite, zircon, tetragonal ZrO_2, and monoclinic ZrO_2 have been identified (Figure 4.5b). It is evident that, with the addition of MgO, the diffraction peaks due to the zircon $ZrSiO_4$ phase became less intense, while peaks attributed to monoclinic and tetragonal phases of zirconia appeared. Therefore, the sintering promoter role of MgO additive on zircon dissociation may be inferred.

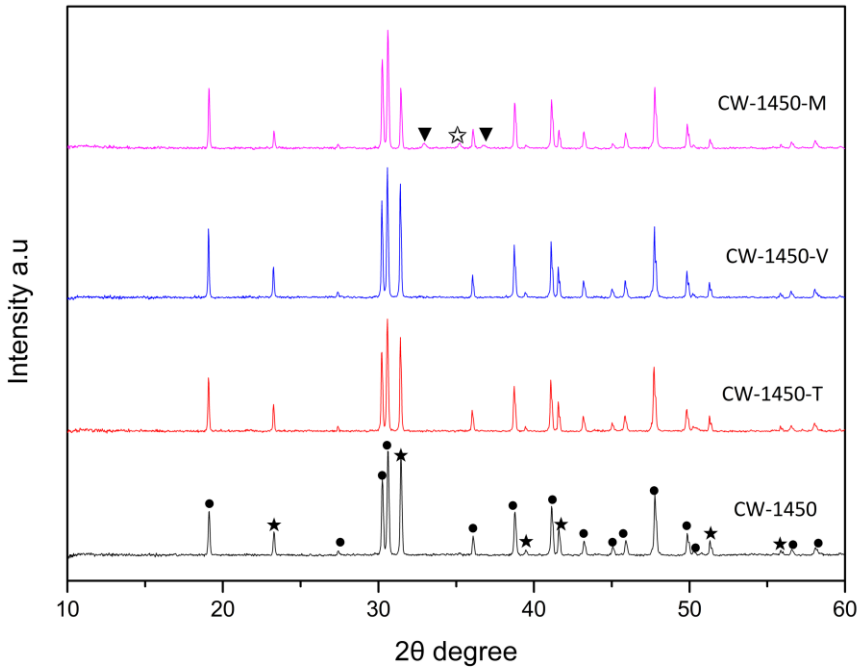


Figure 4.5. XRD patterns of the CW1450, CW1450-T, CW1450-V, and CW1450-M, samples. (★ = zircon, ● = mullite, ▼ = m-ZrO_2, and ☆ = t-ZrO_2)

It is worth noting that, at elevated temperatures, zircon dissociates to silica and tetragonal zirconia because, above 1170°C, the tetragonal phase is the stable phase of zirconia. However, further cooling below 1170°C tetragonal to monoclinic phase transformation occurs [84,85]. Nevertheless, the presence of the tetragonal phase in CW1450-M might be attributed to the stabilization effect of the additive MgO [86]. As the sintering temperature is increased from 1450°C to 1500°C, the zircon content significantly decreases (Figure 4.6). By further increasing the sintering temperature to 1550°C, zircon peaks completely disappear. The zircon decomposition reaction is reversible, and during cooling, zirconia and silica recombine to form zircon. However, no zircon peaks were detectable in the XRD patterns of the CW1550-M and CW1600-M samples. This can be attributed to the alumina additive, which presumably consumed the free silica to yield mullite. It is also worth pointing out that, unlike CW1450-M, which contains both monoclinic and tetragonal zirconia, the samples sintered at 1500°C and above contain zirconia only in the monoclinic phase. The earlier investigations on zirconia ceramics' tetragonal to monoclinic phase transformation have confirmed that increasing the grain size favors this transformation. In contrast, sub-micron grain size is often required to obtain tetragonal phase zirconia [85].

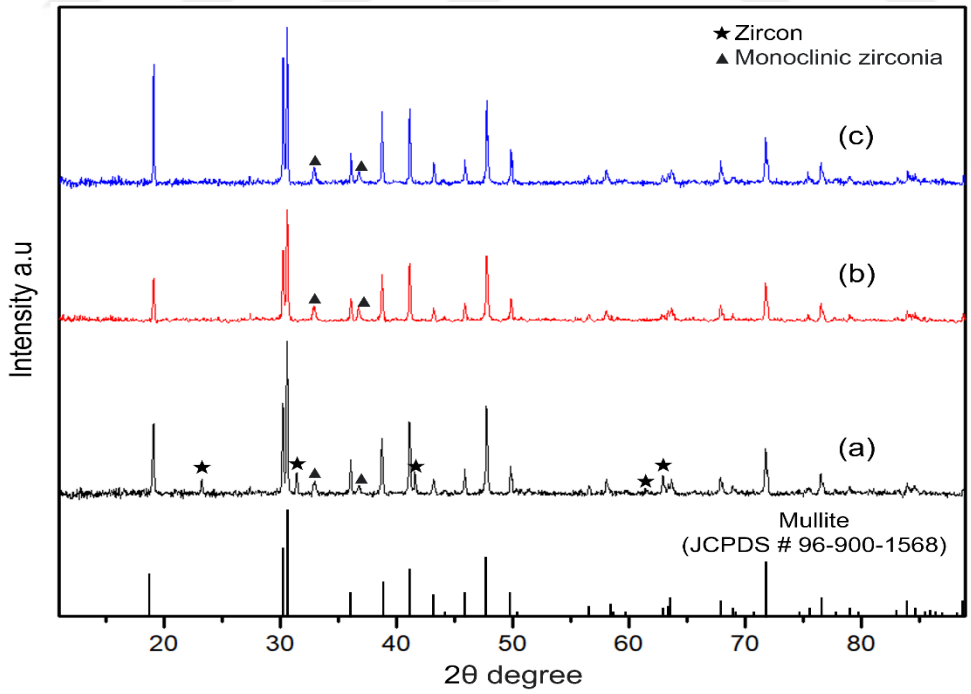


Figure 4.6. XRD patterns of the (a) CW1500-M, (b) CW1550-M, and (c) CW1600-M samples.

4.2.2 Microstructural analysis by SEM

Microstructures analyzed by SEM on fractured surfaces of samples revealed that sintering temperature played a major role in the morphology of mullite crystals. Increasing the sintering temperature from 1500°C to 1550°C led to the formation of elongated mullite crystals with curved edges and corners (Figure 4.7c).

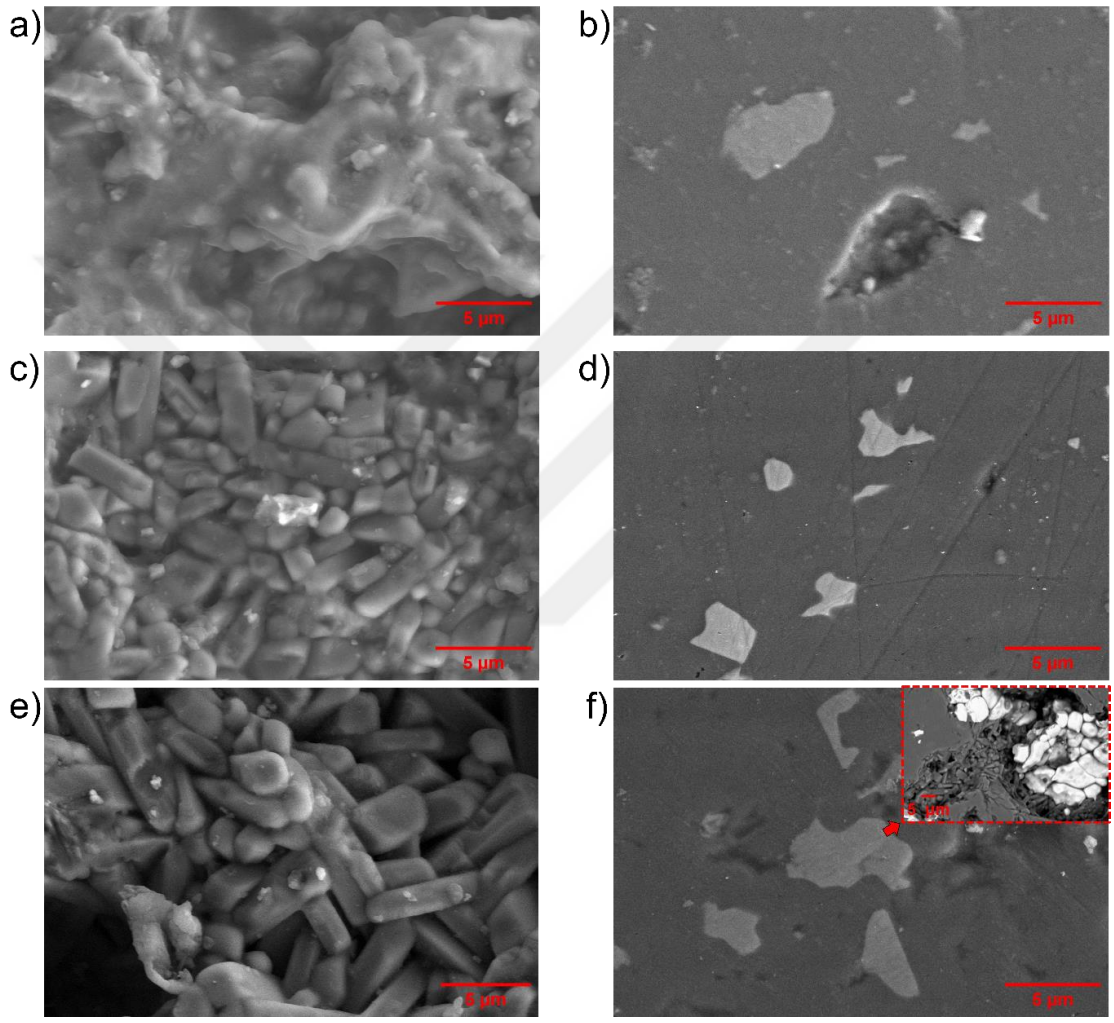


Figure 4.7. SEM images of the (a, c, d) fractured and (b, d, f) polished surfaces of the (a, b) CW1500-M, (c, d) CW1550-M, and (e, f) CW1600-M samples.

On the other hand, the CW1600-M composite show nearly the same microstructure as CW1550-M, but the grain size of mullites is increased due to the Ostwald ripening (Figure 4.7). It is now well established that the elongated morphology is a characteristic of mullites grown in a vitreous phase. Furthermore, the curved edges and corners of mullite grains indicate their formation is realized in the liquid phase. Indeed, the presence of TiO_2

and Fe_2O_3 impurity phases in the ceramic waste and the additive MgO are all reported to form transient liquid phases that promote the growth of mullite grains in elongated morphology [43,87,88]. The micrograph of the polished surface of the samples shows that they consist of irregular zirconia grains distributed in a mullite matrix (Figure 4.7b).

4.2.3 Bulk density, apparent porosity, and linear shrinkage

Figure 4.8 displays the linear shrinkage, bulk density, and apparent porosity values of the sintered composites as a function of sintering temperature. A noticeable linear shrinkage of 15.2% was observed for the sample sintered at 1500°C. The linear shrinkage increases with sintering temperature and reaches 19.4% at 1600°C. Bulk density and apparent porosity results agreed well with the linear shrinkage change. When the sintering temperature increases from 1500 to 1550 °C, the apparent porosity decreases from ~5.4 to ~ 2.3%, while the bulk density adversely increases from 2.62 to 2.66 $g \cdot cm^{-3}$. With the sintering temperature increasing to 1600°C, apparent porosity decreases up to null values (0.3%), whereas bulk density reaches 2.87 $g \cdot cm^{-3}$.

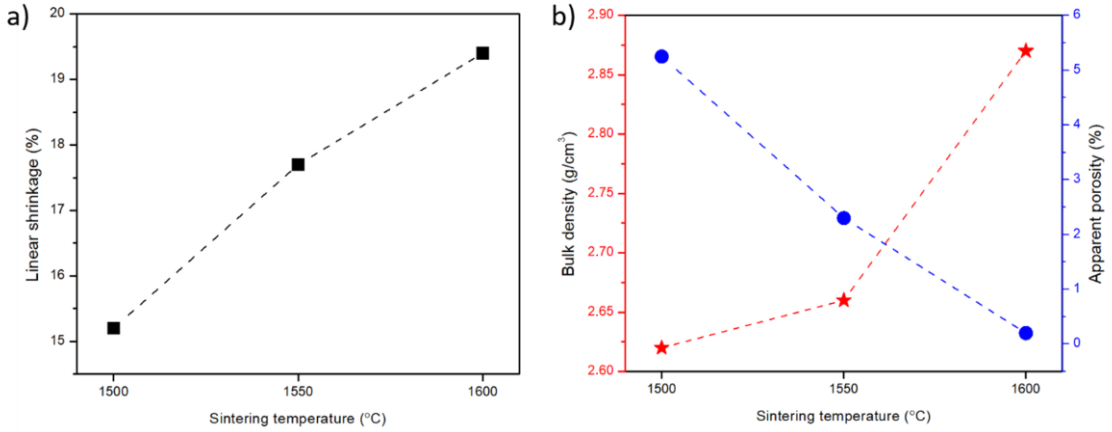


Figure 4.8. (a) Linear shrinkage, (b) bulk density, and (c) apparent porosity values of the CW1500-M, CW1550-M, and CW1600-M samples.

4.2.4 Flexural strength

The compression and flexural strength values of the as-prepared composites and the relevant research on the various mullite ceramics reported in the literature are summarized in Table 4.1. As both the compression and flexural strength were enhanced by increasing the sintering temperature, a correlation between mechanical properties and density can be

inferred. Besides, such enhancement in the mechanical properties might also be ascribed to the formation of elongated-shaped mullite grains with interlocking structures and the toughening effect of zirconia via crack deflection and microcracking mechanisms [89–92]. The highest compression and flexural strengths were obtained by CW1600-M composite, which was 308 and 190 MPa, respectively. These values are comparable to or even better than most other mullite ceramics and mullite-containing composites obtained from recycled raw materials. However, the mechanical properties are slightly low relative to some mullite-zirconia ceramics prepared from fine and pure initial powders. This is probably due to the closed porosities and impurities in the composites. It is also worth stressing that green bodies here were prepared by uniaxial pressing. Besides, the raw materials were coarse; hence, zirconia in these composites was monoclinic. If isostatic or hot pressing would have been applied and zirconia could be stabilized in the tetragonal phase, then higher strength values could be obtained.

Table 4.1. The mechanical properties of mullite-based composites fabricated in this study and various mullites and mullite-based composites reported in the literature.

Final product	Raw materials	Sintering method and temperature	Compression strength (MPa)	Flexural strength (MPa)	Ref.
Mullite/zirconia composite	Investment casting shell waste and alumina	Reaction sintering, 1500°C	164	134	This work
Mullite/zirconia composite	Investment casting shell waste and alumina	Reaction sintering, 1550°C	232	170	This work
Mullite/zirconia composite	Investment casting shell waste and alumina	Reaction sintering, 1600°C	308	190	This work
Mullite	Bauxite and industrial waste fly ash	Reaction sintering, 1600°C	-	186	[38]
Mullite	Alumina and coal fly ash	Reaction sintering, 1500°C	-	169	[93]
V-doped Mullite	High-aluminum fly ash, bauxite and vanadium oxide	Reaction sintering, 1500°C	-	108	[94]
mullite/corundum composite	Industrial waste fly ash, bauxite	Reaction sintering, 1500°C	-	115	[95]
Mullite/zirconia composite	Aluminum nitrate nonahydrate, TEOS, and monoclinic zirconia	Sol-gel method followed by sintering, 1700°C	-	83.30	[96]
Mullite/cordierite composite	Fumed silica, alumina, and magnesia	Reaction sintering, 1400°C	180	-	[97]
Mullite	High-aluminum fly ash	Reaction sintering, 1600°C	169	-	[98]

Y-doped Mullite/zirconia composite	Alumina, silica-gel, zirconia, yttria	Spark plasma sintering, 1400°C	~335		[99]
Ce-doped Mullite	Alumina, silica, and cerium oxide	Reaction sintering, 1650°C	308		[92]
Mullite/zirconia composite	Aluminum sulfate, sodium silicate, zirconium chloride	Spark plasma sintering, 1500°C	-	289	[100]
Mullite/zirconia composite	Mullite and yttria stabilized zirconia	Reaction sintering, 1500°C	-	190	[101]
Mullite/zirconia composite	Electrofused Mullite/zirconia composite and zircon	Reaction sintering, 1600°C	-	~176	[102]
Mullite/zirconia composite	Zircon flour and sillimanite beach sand	Reaction sintering, 1600°C	-	245.9	[103]
Mullite/zirconia/ alumina composite	Zircon and alumina	Reaction sintering, 1650°C	-	~173	[104]
Mullite/zircon composite	Zircon and mullite	Slip casting and sintering, 1600°C	-	~210	[105]
Ti-Mullite/zirconia composite	Alumina, silica, zirconia and titanium oxide	Reaction sintering via hot pressing, 1500°C	-	674.05	[106]
Mullite/alumina/ zirconia/silicon carbide composite	Alumina, silica, yttria stabilized zirconia and silicon carbide	Reaction sintering via hot pressing, 1530°C	-	970	[107]

4.2.5 Theoretical radiation shielding properties

The attenuation of gamma rays occurs through the interaction of the gamma radiation with matter's electrons via multiple absorption and scattering processes. The total cross section is an important feature of radiation shielding materials and can be considered a measure of the probability of photons interacting with a matter. As seen in Figure 4.9a, all samples exhibit similar cross-section variations at given photon energies. This is because all samples' have similar chemical compositions. In the low-energy region, the total cross-sections drastically decrease as photon energy increases for all samples. This rapid decrease proceeds up to the photon energy of approximately 80 keV. The reduction rate slowed in the photon energy range of 80 to 6000 keV. Nevertheless, the cross-section values slowly rise as photon energy further increases. The observed variation in the total cross-section values in different photon energy regions originates from the processes involved in gamma ray-matter interactions. Figure 4.9b-d illustrates

the dominant photon-matter interaction mechanisms for varying energy regions. It can be seen that the photoelectric effect, incoherent scattering (Compton scattering), and pair production are the main processes involved in gamma-ray-matter interactions for all samples. Photoelectric absorption proceeds through the interaction of gamma-ray with an inner shell electron of the matter, which results in the total transfer of gamma-ray energy to the exciting electron. Therefore, elements with higher atomic numbers provide better gamma shielding through the photoelectric absorption mechanism. For the synthesized samples, photoelectric absorption dominates the gamma attenuation process in the low-energy region up to 80 keV. As seen in Table 4.2, CW1600-M and CW1550-M contain slightly higher zirconium than CW1500-M. Zirconium possesses a higher atomic number than aluminum and silicon. Therefore, its abundance in CW1600-M and CW1550-M provides better gamma attenuation relative to CW1500-M (inset of Figure 4.9a). From 80 to 6000 keV, incoherent scattering (Compton scattering) becomes dominant. When a photon interacts with a charged particle, most frequently an electron, it scatters incoherently and losses its energy. This phenomenon is also called the Compton effect. In this process, the photons' energy is partially transferred to the recoiling electron [108]. Figure 4.9d indicates that the CW1600-M sample can attenuate gamma rays via the incoherent scattering mechanism up to approximately 20000 keV. When the photon's energy exceeds 20000 keV, a high-energy pair production phenomenon becomes a dominant attenuation mechanism. In this phenomenon, high-energy photons interact with the nucleus, forming subatomic particle pairs such as an electron and a positron [108].

Table 4.2. Sample codes, measured density, the weight fraction of constituent compounds

Sample codes	Density (g/cm^3)	The weight fraction of constituent compounds (%)		
		$Al_6Si_2O_7$	ZrO_2	$ZrSiO_4$
CW1500-M	2.62	93	4	3
CW1550-M	2.66	93	7	-
CW1600-M	2.87	93	7	-

Linear attenuation coefficient (μ) is a constant that describes the fraction of attenuated gamma rays per unit thickness of matter. The linear attenuation coefficient can be

expressed by Beer-Lambert law as fallow;

$$I = I_0 e^{-\mu x} \quad (3)$$

μ (cm^{-1}) is the material's linear attenuation, x (cm) is the thickness of the material, I_0 is the incident beam intensity, and I is the intensity after attenuation [109,110].Linear attenuation coefficient can further be converted into a material constant called the mass attenuation coefficient (μ_ρ; cm^2/g) by dividing it by the density of the material.

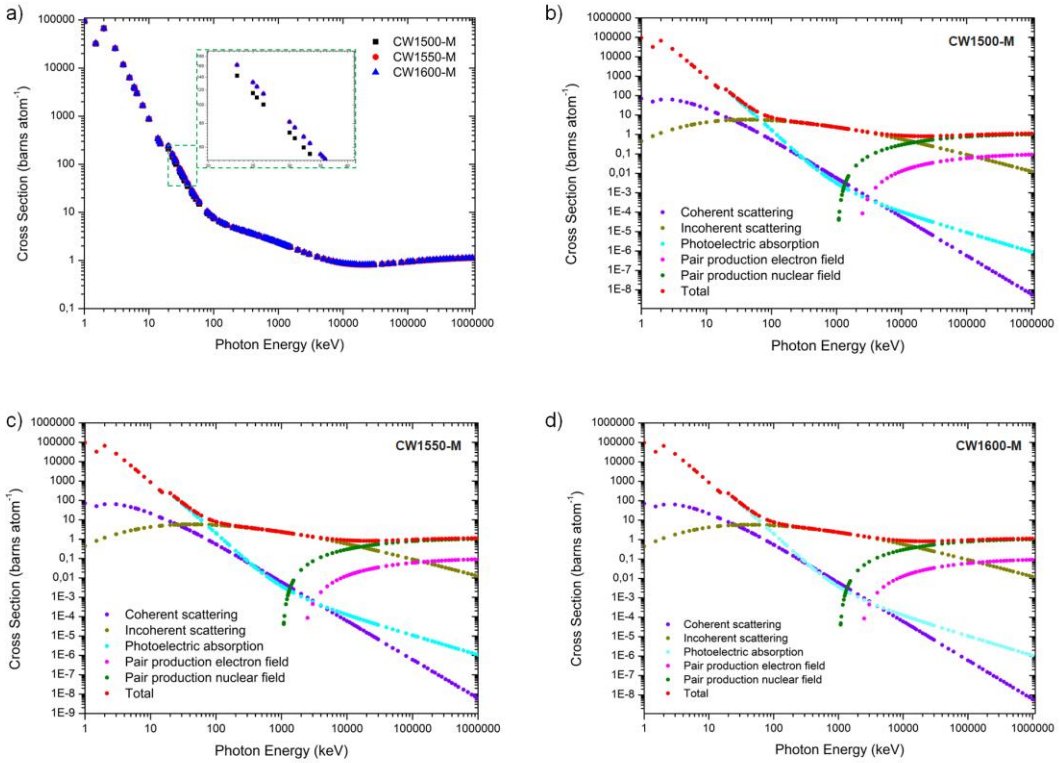


Figure 4.9. (a) The relative variations of the total cross section for the CW1500-M, CW1550-M, and CW1600-M samples vs. photon energy. The relationship between the photon energy and cross-section of (b) CW1500-M, (c) CW1550-M, and (d) CW1600-M in the energy range from 1 to 10^6 keV.

The calculated linear and mass attenuation coefficient variations of samples against varying photon energy values are presented in Figure 4.10. The results show that the samples' linear attenuation coefficient increases with increasing sintering temperature. Indeed, CW1600-M demonstrates a relatively higher linear attenuation coefficient than both CW1500-M and CW1550-M samples in the whole photon energy region. It is

reasonable that a low-density absorber provides less attenuation than a high-density absorber because the probability of an interaction between the radiation and the absorber's atoms decreases with increasing porosity [111]. Nevertheless, all samples exhibit similar mass attenuation coefficient variations due to their similar chemical compositions, as seen in Figure 4.10b.

The mean free path (MFP) is a measure of the average distance that a photon can travel between two collisions. The MFP can be determined from the linear attenuation coefficient using equation 4 [112].

$$\mathrm{MFP} = 1/\mu \tag{4}$$

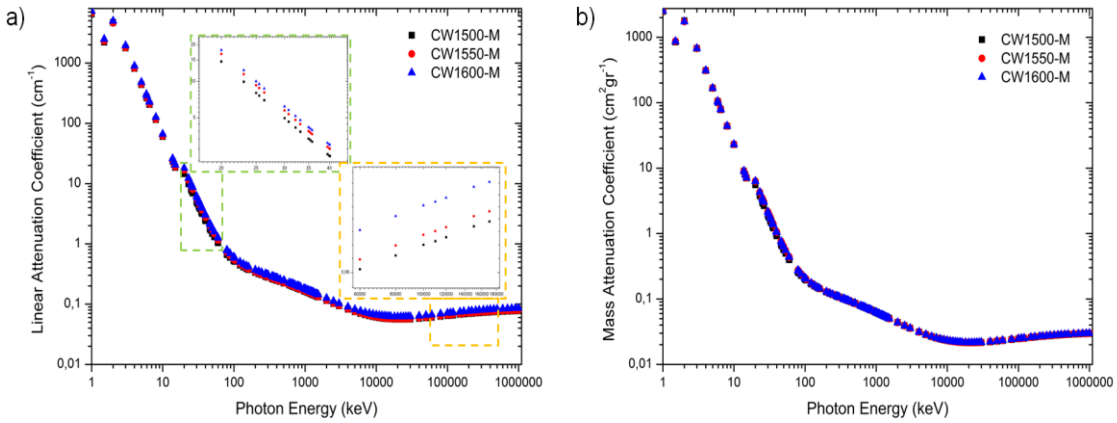


Figure 4.10. The relative variations of (a) linear attenuation coefficient and (b) mass attenuation coefficient for the CW1500-M, CW1550-M, and CW1600-M samples vs. photon energy. The insets in (a) show amplified graphs of emphasized regions.

The MFP variations of fabricated ceramics against photon energy are presented in Figure 4.11a. It has been found that MFP values for all ceramic samples remain almost zero up to photon energies of roughly 30 keV. This means that photons with energies less than 30 keV cannot penetrate the fabricated ceramics. Although the MFP values steadily rise from photon energy of 30 keV to 100 keV, they remain lower than 2 cm for all ceramics. Beyond the photon energy of 100 keV, a sharper increase is observed. Meanwhile, the difference between the MFP values of the ceramic samples enlarged. For the photon energy at around 20000 keV, MFP values of CW1500-M, CW1550-M, and CW1600-M were determined as 17.8, 17.4, and 16.1 cm, respectively.

The half-value layer (HVL) is another important parameter for radiation shielding

materials, that is, the required material thickness to reduce the radiation intensity by 50%. HVL can be expressed using the following equation [112].

$$\mathrm{HVL} = \ln(2)/\mu \tag{4.1}$$

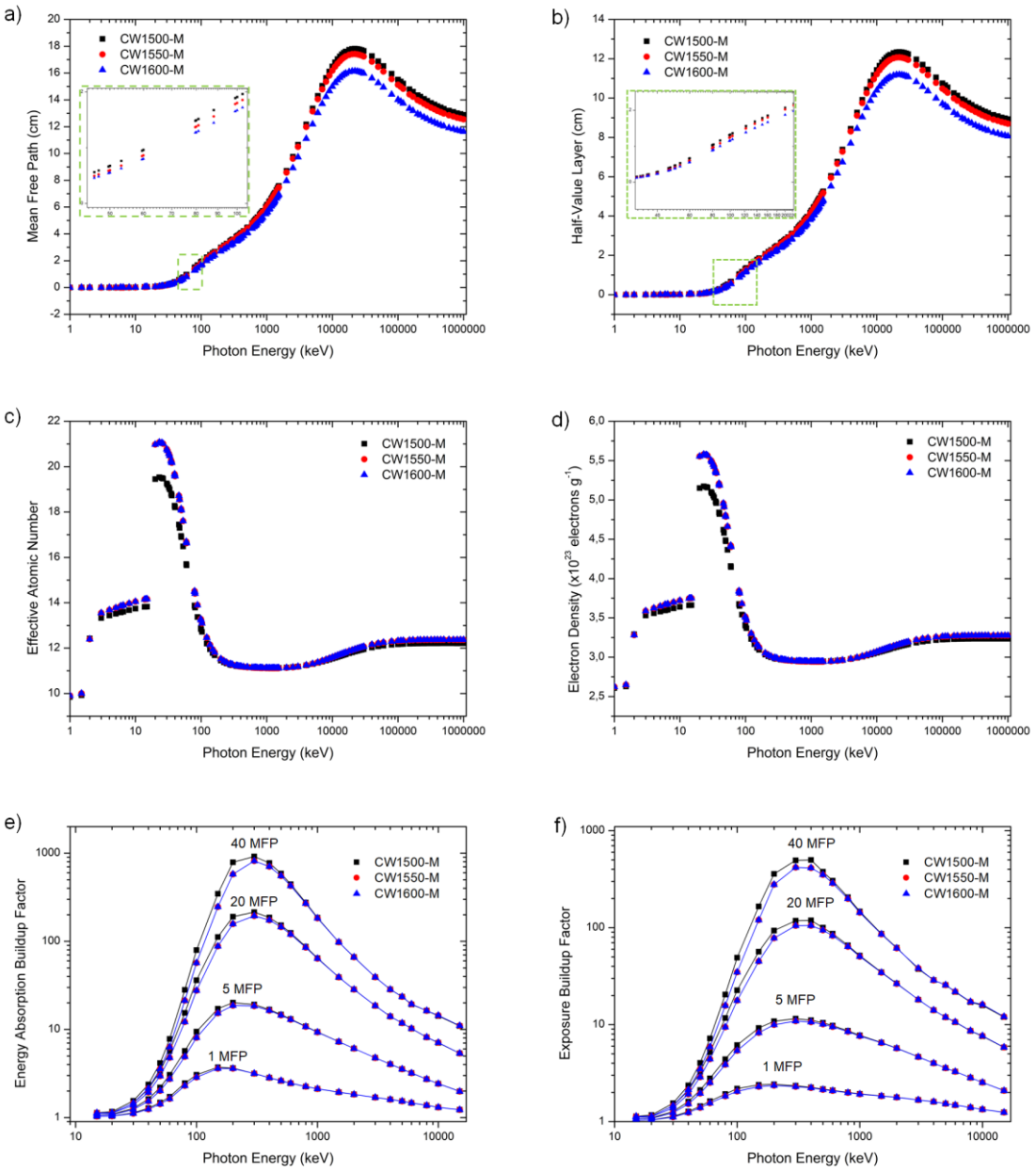


Figure 4.11. The relative variations of (a) the mean free path (MFP), (b) half-value layer (HVL), (c) effective atomic number (Zeff), (d) electron density (Neff), (e) energy absorption buildup factor (EABF), and (f) exposure buildup factor (EBF) for the CW1500-M, CW1550-M, and CW1600-M samples vs. photon energy.

As shown in Figure 4.11b, HVL values demonstrate a similar trend as the MFP values for all ceramics. The highest HVL thickness of ceramics was observed at around 22000 keV. The HVL values of 12.35, 12.07, and 11.19 cm were measured for CW1500-M, CW1550-M, and CW1600-M, respectively. Among all samples, CW1600-M possesses the lowest MFP and HVL values in the whole photon energy range owing to its higher density and zirconium content.

The effective atomic number (Z_{eff}) and electron density (N_{eff}) variations of ceramics are also investigated (Figure 4.11c-d). The results indicate that Z_{eff} and N_{eff} reach their maximum value at around 23 keV photon energy due to a K-shell absorption edge. Following the maxima, a gradual decrease in Z_{eff} and N_{eff} is observed with the increase of the photon energy. Because CW1550-M and CW1600-M have the same chemical composition, their Z_{eff} and N_{eff} variations were similar. On the other hand, due to its lower zirconium content, CW1500-M showed slightly lower Z_{eff} and N_{eff} values in the all-energy range.

The variation of the energy absorption build-up factor (EABF) and exposure build-up factor (EBF) at various penetration depths are depicted in Figure 4.11e and Figure 4.11f, respectively. These figures demonstrate that the EABF and EBF values initially rise with the increasing photon energy, reaching their peak value at the photon energy of approximately 300 keV, then start to decline. The observed trend relates to varying photon-matter interaction mechanisms in different energy regions [113,114]. Lower EABF and EBF values indicate a greater radiation shielding performance. Figure 4.9b-d show that the photoelectric effect is predominated in the low-energy region. Because the photoelectric effect is highly efficient for gamma attenuation, EABF and EBF values up to around 100 keV are fairly low for all ceramic samples. Then, Multiple scattering events occur at higher photon energies when Compton scattering is the dominating process, where EABF and EBF values reach their peaks. With a further increase in photon energy, the pair production mechanism becomes dominant in the attenuation process, which results in a reducing trend in the EABF and EBF values [113,114]. Moreover, when the penetration depth increased from 1 MFP to 40 MFP, it is seen a dramatic increase in the EABF and EBF values. This can be ascribed to increased scattering effects within the ceramics. It is also worth mentioning that there is a direct correlation between total cross-sections and Z_{eff} with the EABF and EBF values. Furthermore, we have compared the

mass attenuation coefficient variations of commonly used radiation shielding materials with the CW1600-M sample. As seen in Figure 4.12a, the CW1600-M sample exhibit similar mass attenuation coefficient values to that of high alumina cement, which are greater than portland cement and water for the whole photon energy region.

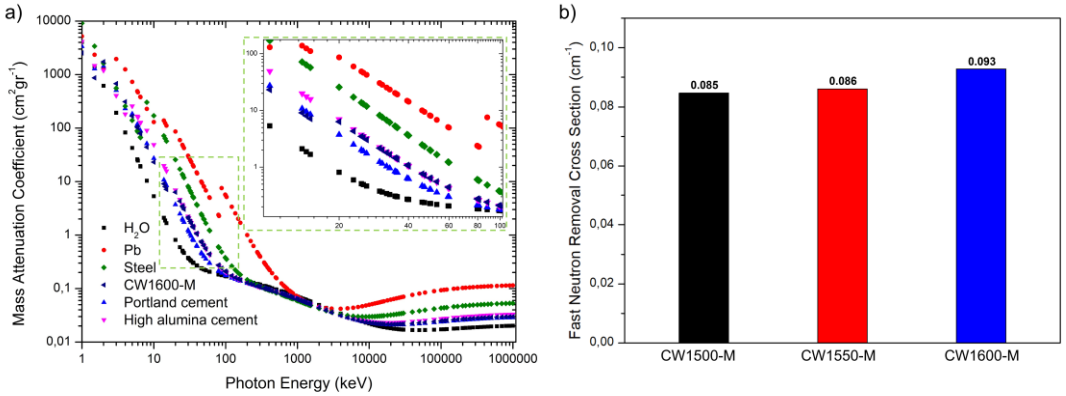


Figure 4.12. (a) Comparison of the mass attenuation coefficient variations of commonly used radiation shielding materials with CW1600-M (b) The fast neutron removal cross-sections of CW1500-M, CW1550-M, and CW1600-M samples computed using the PhysX software.

Figure 4.12b displays ceramic samples' fast neutron removal cross-sections computed using the PhysX software. It was observed that the CW1600-M sample (ΣR=0.093 cm−1) provides a relatively higher fast neutron removal cross-section than other samples mainly because of its higher density. Graphite (ΣR=0.077 cm^{-1}) and paraffin (ΣR=0.0773 cm^{-1}), two extensively used neutron shielding materials, have been outperformed by ceramics made from investment casting shell waste. Most notably, the CW1600-M sample (ΣR=0.093 cm^{-1}) has almost the same fast neutron removal cross-section as concrete (ΣR=0.094 cm^{-1}) [115,116].

4.3 Characterization of Cordierite-based composites

This subsection will introduce characterization data, including crystalline phase and microstural analysis, bulk density, apparent porosity, linear shrinkage, and flexural strength, and both theoretical and experimental radiation shielding properties for cordierite-based composites obtained from a mixture of CW, alumina, and magnesia. For a better assesment results, the chapter starts with characterization data of ceramic

composites fabricated from CW without any additive. Additionally, the influence of five different additives, Bi_2O_3, La_2O_3, Y_2O_3, Ta_2O_5, and WO_3, with concentrations varying from 1 to 10 wt.% on the various properties of the cordierite-based composites are also presented in this chapter.

4.3.1 Ceramics Composites Fabricated from CW Without Any Additive

4.3.1.1 XRD analysis

The crystal phase of the investment casting shell waste powder reveals that it is mainly composed of zircon, quartz, cristobalite, mullite, and corundum, as shown in Figure 4.13. It is now well established that quartz transforms into amorphous silica and then to cristobalite as the sintering temperature increases. From 1250 to 1350˚C, the peak intensity of quartz indeed decreases where almost no quartz was detected for the W-1350 samples.

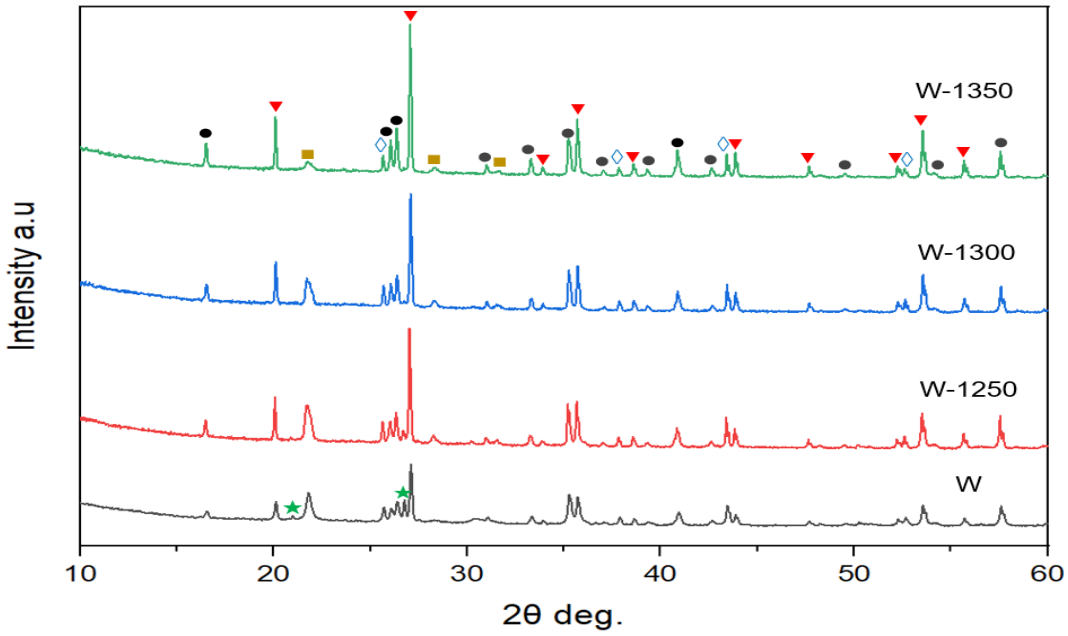


Figure 4.13. XRD patterns of the W, W-1250, W-1300, and W-1350 samples. (★ = quartz, ● = mullite, ▼ = zircon, ■ = cristobalite, and ◊ = corundum)

However, as seen in Figure 4.13, the peak intensity of cristobalite along with that of corundum, also declined. This observation is probably due to the mullite formation reaction between silica and alumina, which starts at about 1250˚C and accelerates with increasing firing temperature. It is also evident that the relative peak intensity of mullite

slightly increases while that of quartz and alumina decreases. Nevertheless, both corundum and cristobalite phases are still evident for W-1350. This indicates that firing investment casting shell waste at 1350˚C for 4 h is not sufficient to achieve complete mullitization among its silica and corundum components of investment casting shell waste.

4.3.1.1 Bulk density, apparent porosity, and linear shrinkage

The bulk density of ceramic composites first decrease slightly with increasing sintering temperature and then increases (Figure 4.14). The bulk densities of ceramic composites prepared from investment casting shell waste without any additive are 1.77, 1.74, and 1.80 g/cm^3 for 1250˚C, 1300˚C, and 1350˚C, respectively. XRD results demonstrated the presence of quartz in the investment casting shell waste. Silica experinces sequance of phase transofmations when heated. These phase transformations involves, α-quartz to β-quartz at 573◦C, β-quartz to tridymite at 870◦C and formation of cristobalite (1470◦C). Nonetheless, the presense of impurities can significantly lower the cristobalite formation temperature, i.e., to below 1000◦C. It is now well establieshed that cristobalite has a lower density than quartz. Therefore, microcracks often develops in ceramic bodies during the quartz to cristobalite phase transfomartion, leading to lower density values. XRD results have shown that quartz peaks in the investment casting waste gradually decreases with increasing sintering temperature. Hence, the observed decrease in the density from 1.77 g/cm^3 of W-1250 to 1.74 g/cm^3 of W-1300 can be ascribed to the phase changes occurring in samples. However, the increase from 1.74 g/cm^3 to 1.80 g/cm^3 can be attributed to the enhanced densification behaviour. Nevertheless, it is worth stressing that the densification of all these samples were considerably low. Indeed, although the apparent porosity slightly decreases with increasing sintering temperature, it varies in the range of 39.84-41.10 %. Meanwhile, the linear shrinkage increases from 0.9 to 2.1 with increasing sintering temperature.

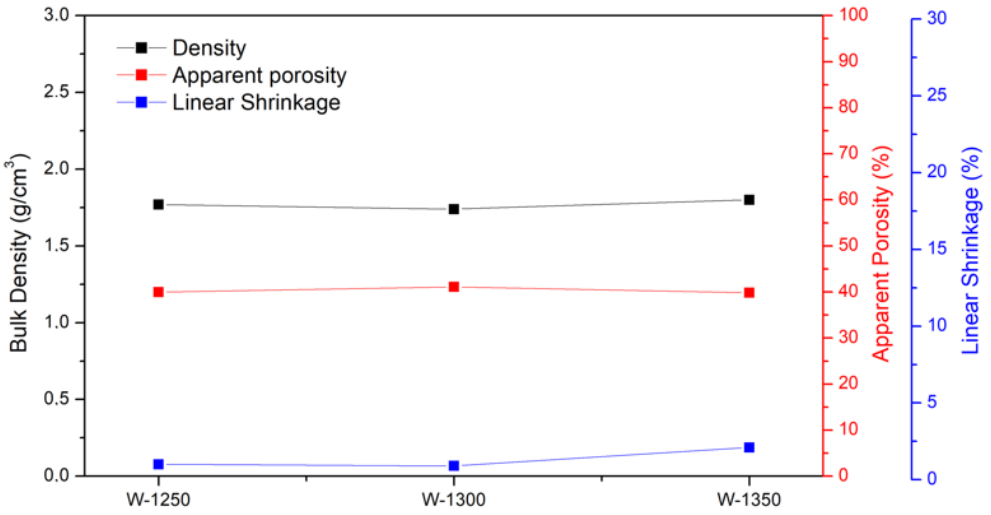


Figure 4.14. Bulk density, apparent porosity, and linear shrinkage for W-1250, W-1300, and W-1350.

4.3.1.2 Flexural strength

The influence of sintering on the mechanical properties of composite materials are shown in Figure 4.15. It is evident that, flexural strength of composite materials increased with rising sintering temperature, albeit in a low rate. Indeed, flexural strength values of these samples range only in between 8.35-8.86 MPa.

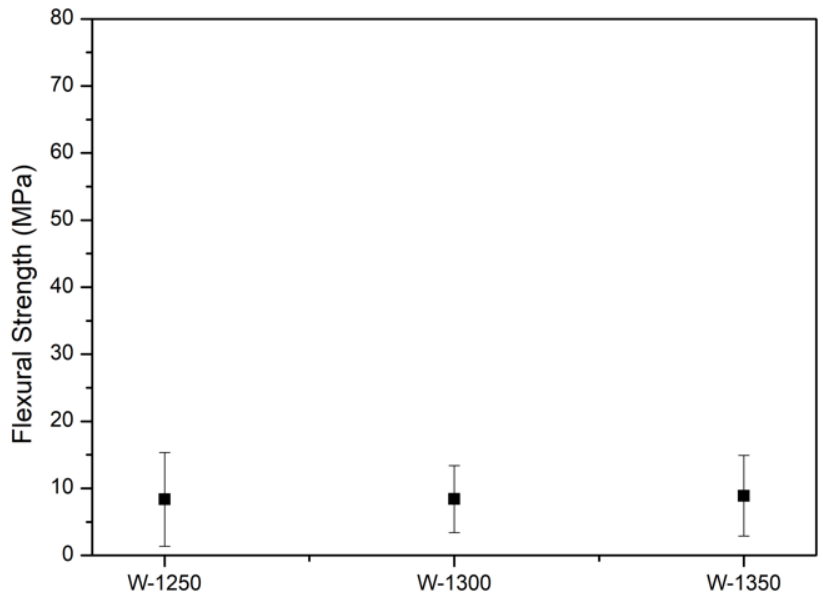


Figure 4.15. Flexural strength for W-1250, W-1300, and W-1350.

In general, a number of factors, including the composition of the material, the sintering temperature, and the porosity, affect the mechanical properties of ceramic materials. Low mechanical properties of these composites primarily due to the poor grain to grain

interraction and lack of bonding between particles low and orginates their low densification behavior. In addition, it is possible that the thermal mismatch of different phases in the investment casting shell waste cause the formation of microcracks which deteriorates mechanical properites.

4.3.1.3 Microstructural analysis by SEM

Scanning electron microscopy images of the fructured surfaces of W-1250, W-1300, and W-1350 composites are presented in Figure 4.16. It can be seen that all samples have highly porous microstructure, which is in good agreement with the obtained density and apparent porosity values. Nevertheless, particle sizes increases with increasing sintering temperature due to Ostwald ripening. Indeed, particles with sizes larger than 5 μm are apperent for W-1300 and W-1350. Furthermore, sharp edges of particles of W-1250 and W-1300 become round for W-1350.

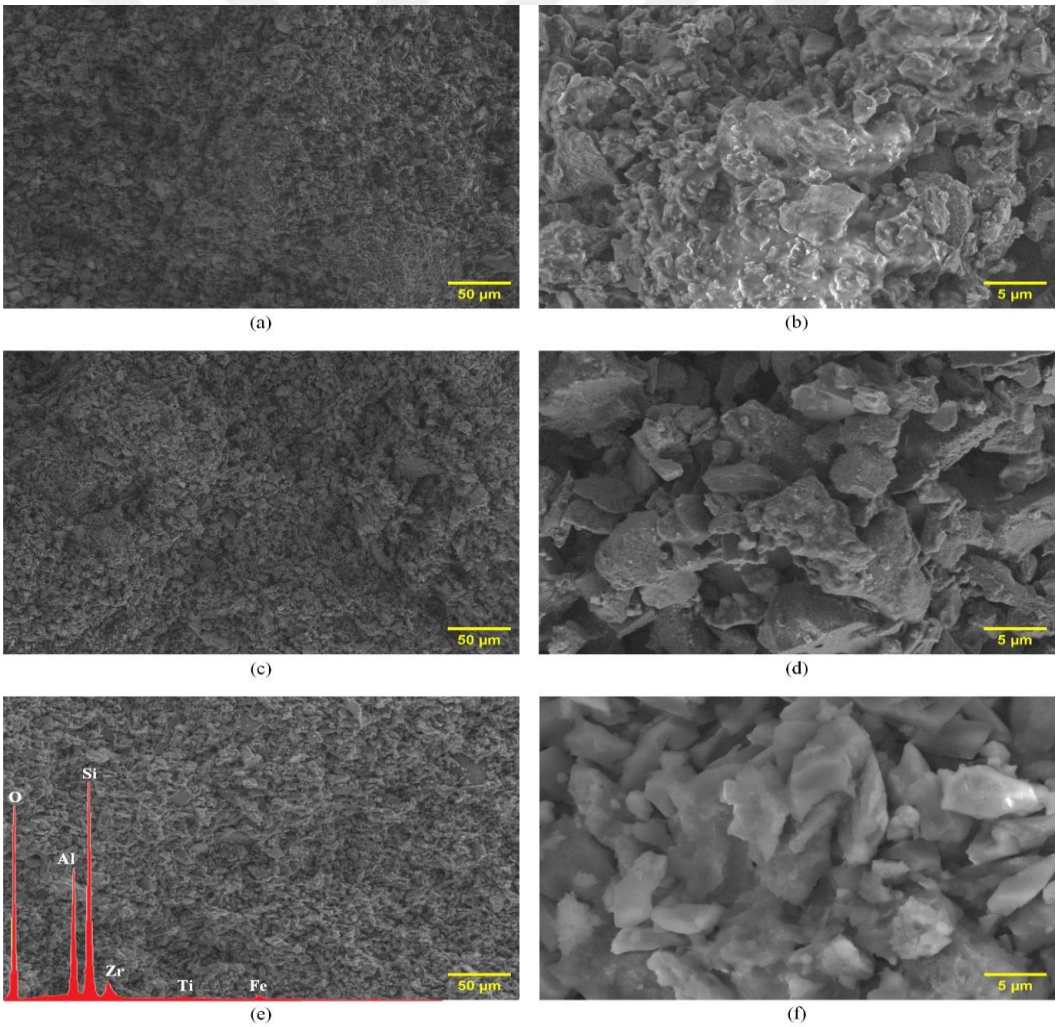


Figure 4.16. SEM images of (a,b) W-1250, (c,d) W-1300, (e,f) W-1350.

4.3.2 Cordierite-based composites without any additive

4.3.2.1 XRD analysis

In the section 4.1.4, XRD analysis of W has shown that it is composed of mullite, zircon, and silica. Ceramics investigated in this section are formulated for the conversion of free silica from W into cordierite. Figure 4.17 shows the XRD patterns of the fired pellets prepared from alumina, magnesia, and investment casting shell waste powder mixture to obtain cordierite-containing composites at 1250-1350°C for 3 h. The formation of cordierite was first observed at 1250°C. This might be attributed to the reaction between corundum, magnesia, and silica:

$$Al_2O_3\ (s) + MgO\ (s) + SiO_2\ (s) \rightarrow Mg_2Al_4Si_5O_{18}(s) \qquad (4.1)$$

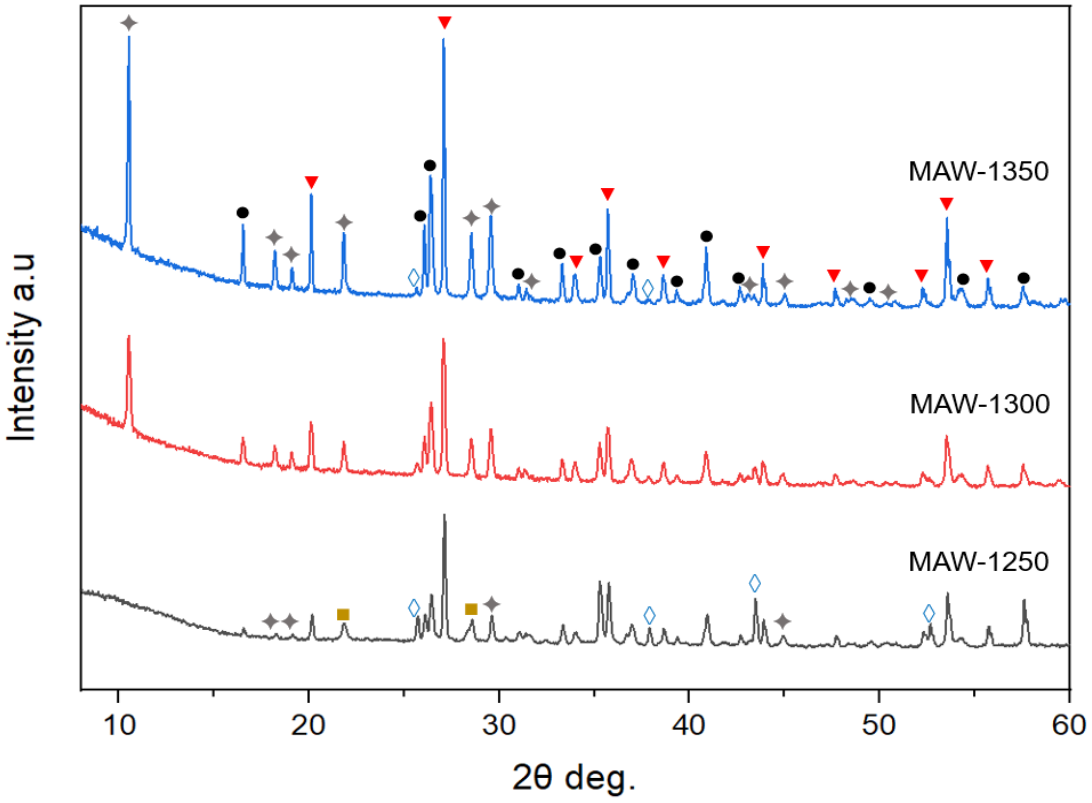


Figure 4.17. XRD patterns of the MAW-1250, MAW-1300, and MAW-1350 samples. (✦ = cordierite, ● = mullite, ▼ = zircon, ■ = cristobalite, and ◊ = corundum

Nevertheless, the fraction of formed cordierite was low. Besides, a large amount of cristobalite and corundum phases are still present. As temperature increases, the corresponding cordierite peaks become stronger and narrower. Meanwhile, cristobalite

disappears first and then almost corundum. Thereby, ceramic composites mainly composed of cordierite, mullite, and zircon are obtained.

4.3.2.2 Bulk density, apparent porosity, and linear shrinkage

The physicomechanical properties of the MAW-1250, MAW-1300, and MAW-1350 ceramic composites are presented in Figure 4.18. It can be seen that the bulk density of composites slightly decreases with increasing sintering temperature then increases. Besides, the bulk density values of the MAW-1250, MAW-1300, and MAW-1350 samples are comparatively lower than ceramic composites fabricated directly from W without any additive. The relatively lower bulk density values of cordierite-based composites might be ascribed to its comparatively light magnesia constituent and the formation of cordierite phase because the formation of cordierite leads to volume expansion which results in a decrease in bulk density [117]. This also correlates well with linear shrinkage values because linear shrinkage values of cordierite-based composites are also lower than those of ceramic composites fabricated from W without any additive. Apparent porosities of the MAW-1250, MAW-1300 and MAW-1350 samples are 39.78, 41.1, and 39.79, respectively. Although the apparent porosities of these samples are high, this is typical for cordierite-based composites.

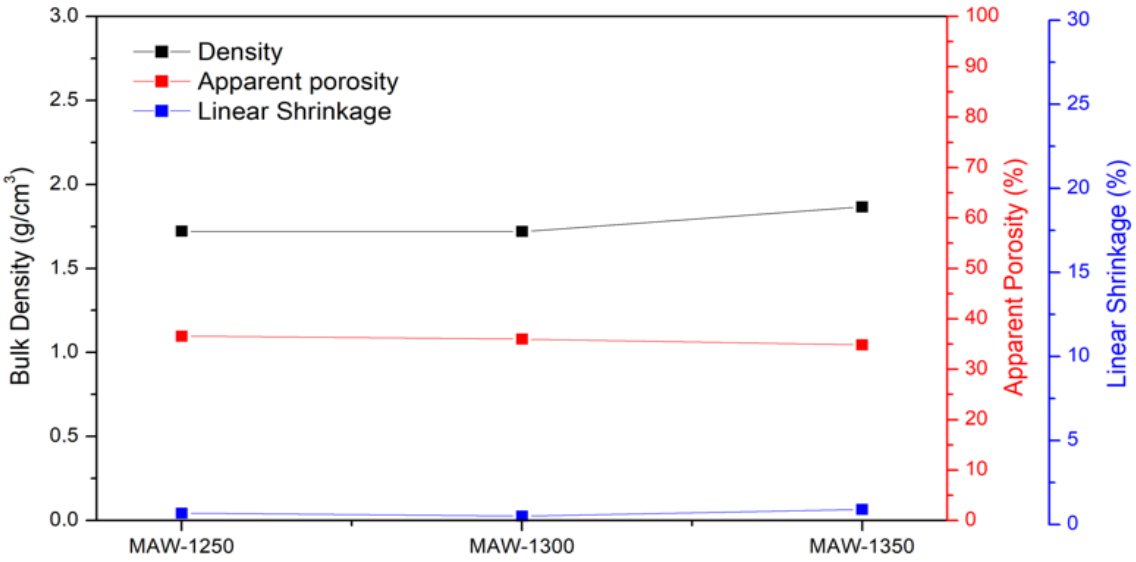


Figure 4.18. Bulk density, apparent porosity, and linear shrinkage for MAW-1250, MAW-1300, and MAW-1350

4.3.2.3 Flexural strength

The influence of sintering on the mechanical properties of the cordierite-based composite materials are demonstraded in Figure 4.19. The flexural strength of cordierite-based composites is considerably improved compared to ceramic composites fabricated from W without any additive. Flexural strength improved with increasing sintering temperature. It is worth stressing that MAW-1350 sample demonstrated almost 6-fold higher flexural strength than W-1350. This enhancement can be attributed to the formation of the interlocking structure of mullite whiskers, reduction in liquid silica phase and enhanced densification behavior.

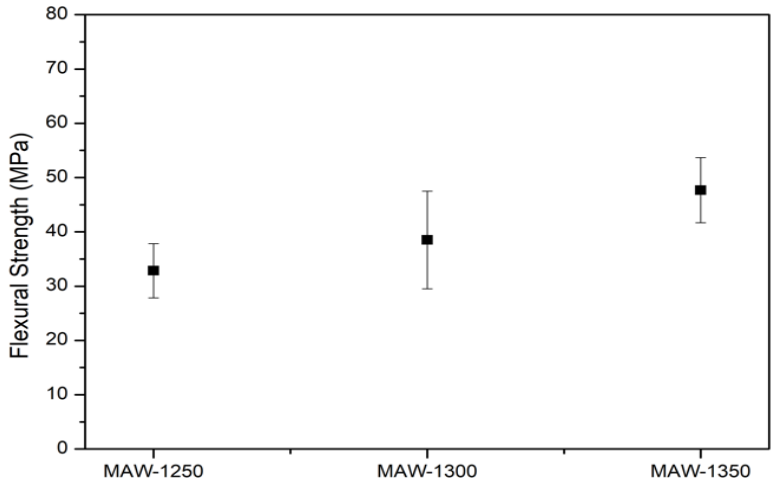


Figure 4.19 Flexural strength for MAW-1250, MAW-1300, and MAW-1350

4.3.2.4 Microstructural analysis by SEM

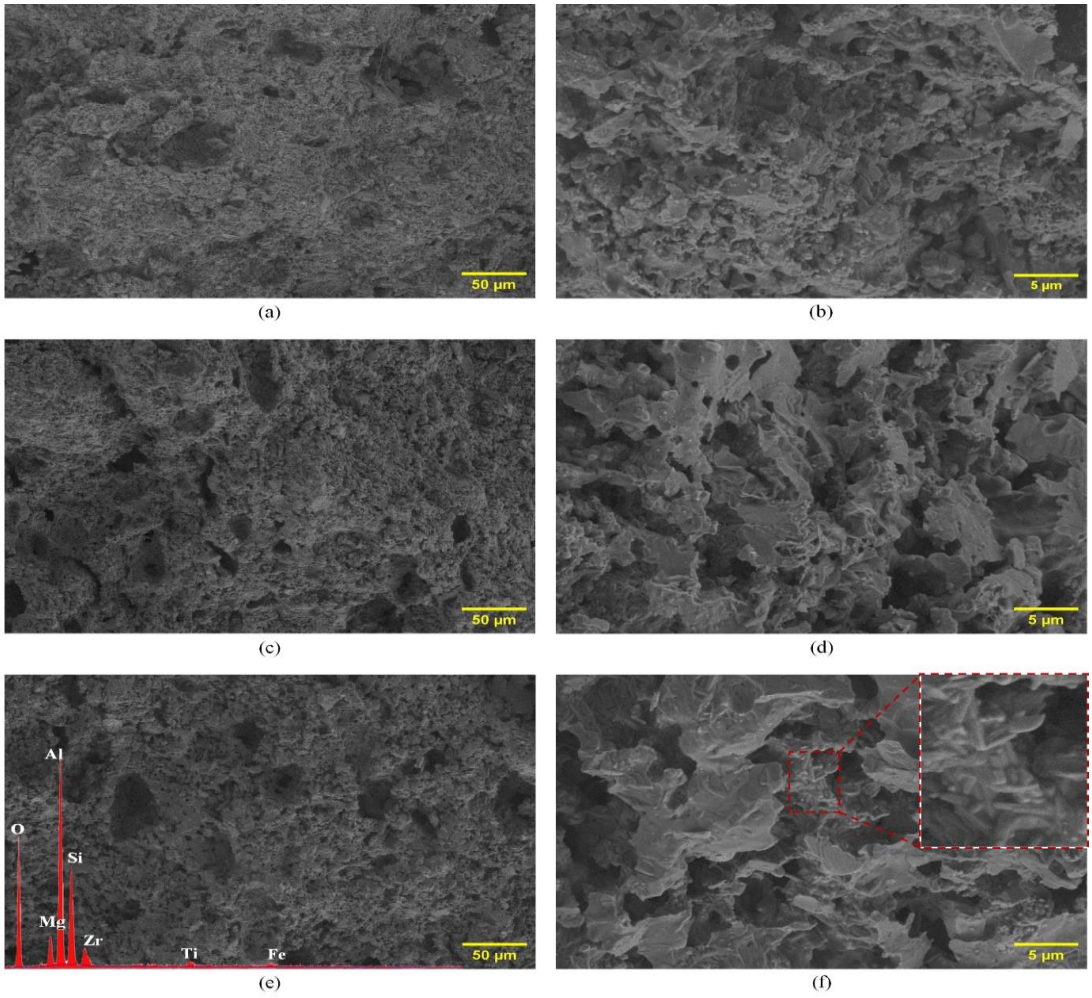


Figure 4.20 SEM images of (a,b) MAW-1250, (c,d) MAW-1300, (e,f) MAW-1350. Inset: EDS results for MAW-1350.

Figure 4.20 displays the SEM images of the MAW-1250, MAW-1300, and MAW-1350 composites. The addition of magnesia and alumina to investment casting shell waste had a notable influence on the microstructure and morphology. The images of MAW-1250 indicates the formation of fine cordierite crystals with sintering process. Additionally, sintering temperature plays an influensive role on the the microstructural and morphological evolution as particle size considerably increases with increasing sintering temperature.

4.3.3 Influence of La_2O_3 additive

4.3.3.1 XRD analysis

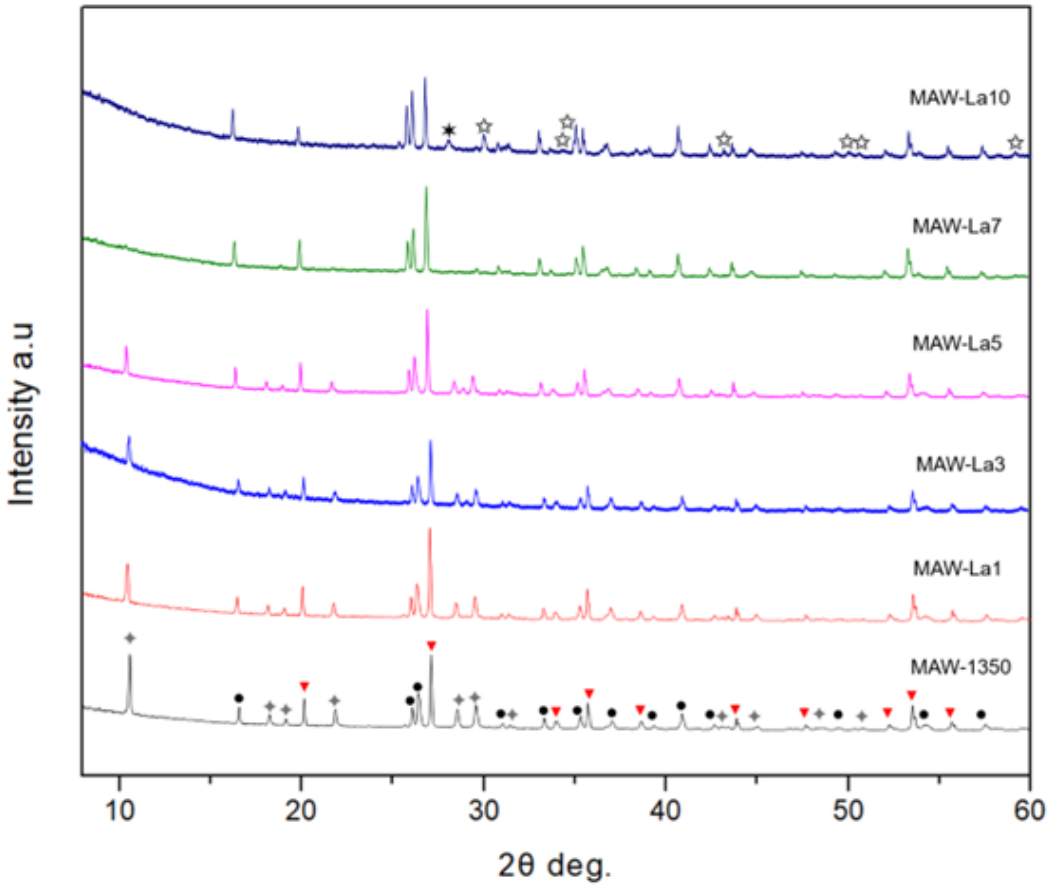


Figure 4.21. XRD patterns of the MAW-1350 and MAW-La1-10 samples. (✦ = cordierite, ● = mullite, ▼ = zircon, ✶ = m-ZrO_2, and ☆ = t-ZrO_2)

To study the effect of La_2O_3 additive on the phase compositions of ceramic composites, crystalline phases of MAW-1350-La1-10 samples containing different amounts of La_2O_3 additive sintered at 1350°C for 4 h and analyzed by XRD (Fig. 3). The main crystalline phases in MAW-1350-La1-5 samples are cordierite, zircon and mullite. The remaning small cordundum phase seen in MAW-1350 and MAW-1350-La1 samples completely disappears when La_2O_3 additive increased to 3% wt. Thereby, MAW-1350-La3 and MAW-1350-La5 samples contain only cordierite, zircon and mullite phases. Nonetheless, as the La_2O_3 additive content reaches to 7% wt. cordierite phase disappears. Meanwhile, the relative intensity of mullite peaks increases. Thereby, MAW-1350-La7 becomes a mullite-zircon composite. It is now well established that cordierite melts incongruently

between 1440-1460 °C, decomposing into mullite and liquid phases, suggesting that La_2O_3 has acceleration effects on the cordierite dissolution. When the La_2O_3 content reaches 10 wt.%, the intensity of mullite peaks further increases, whereas that of zircon decreases.

The decomposition temperature of zircon is about 1673±10ºC. Nevertheless, comprehensive studies revealed that sintering additives such as MgO and La_2O_3 may partially dissociate of zircon into zirconia and silica at lower temperatures. Nonetheless, no silica phase was detected for the sample containing 10 wt.% La_2O_3, indicating that it has combined with alumina to form mullite. Besides, peaks belonging to monoclinic and tetragonal zirconia appeared. The tetragonal phase is the stable phase of zirconia above 1170°C. However, further cooling below 1170°C tetragonal to monoclinic phase transformation occurs. The presence of the tetragonal zirconia phase in MAW-1350-La10 might be attributed to the stabilization effect of MgO.

4.3.3.2 Bulk density, apparent porosity, and linear shrinkage

The bulk densities, apparent porosity and linear shrinkage values of the samples containing different amounts of La_2O_3 additive are shown in Figure 4.22. The addition of La_2O_3 considerably enhances bulk density and reduces apparent porosity. Meanwhile, linear shrinkage increases as La_2O_3 additive content increases. The densification enhancement observed for these ceramic bodies might be attributed to the liquid phase formation ability of La_2O_3 additive and MgO.

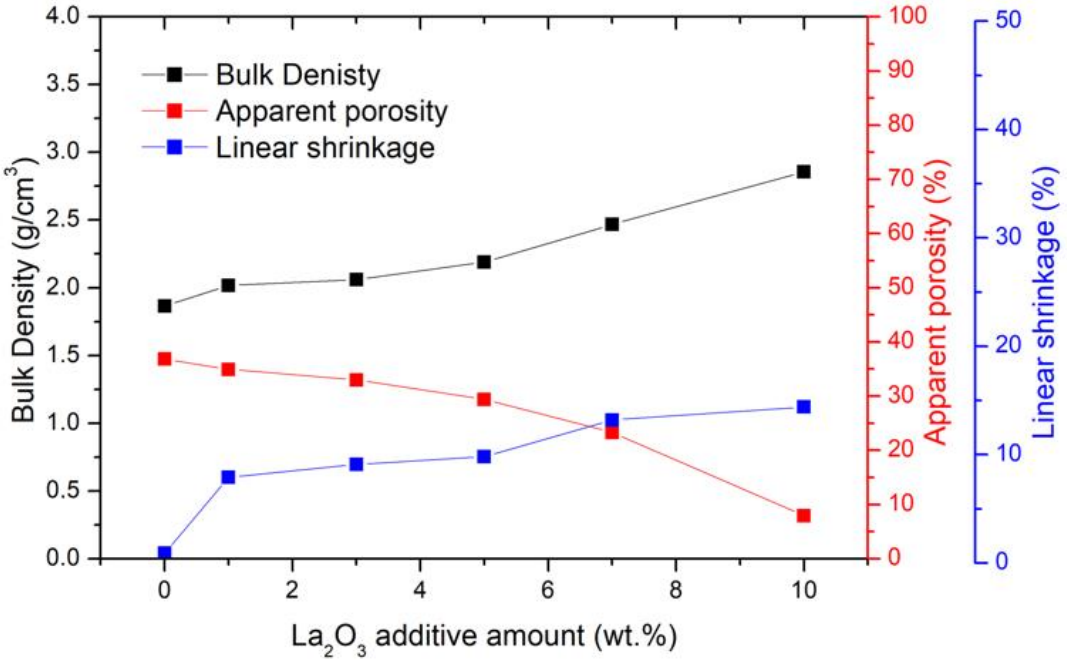


Figure 4.22. Variations of bulk density, apparent porosity, and linear shrinkage as a function of La_2O_3 additive content

4.3.3.3 Flexural strength

Flexural strength values of MAW-1350-La1-10 samples as a function of La_2O_5 additive amount illustrated in Figure 4.23. Flexural strength increases greatly from about 48 MPa to 192 MPa with the increase of La_2O_5 additive amount from 0 to 10 wt.%. The rate of increase at first was mild but accelerated at higher fractions of La_2O_5 additive. MAW-1350-La3 and MAW-1350-La5 composites having similar phase compositions exhibited comparable mechanical performance. On the other hand, a further 30% increase in flexural strength was observed when the La_2O_5 additive amount increased to 7 wt.%. Comparatively sharper enhancement detected for the MAW-1350-La10 might be attributed to crack deflection and propagation and Martensitic transformation toughening effect of the t-ZrO_2 as well as the formation of elongated mullite grains of interlocking structure [89–92]. Furthermore, the increase in the mechanical properties are also agrees well with the increasing densification of the samples and decreased porosities.

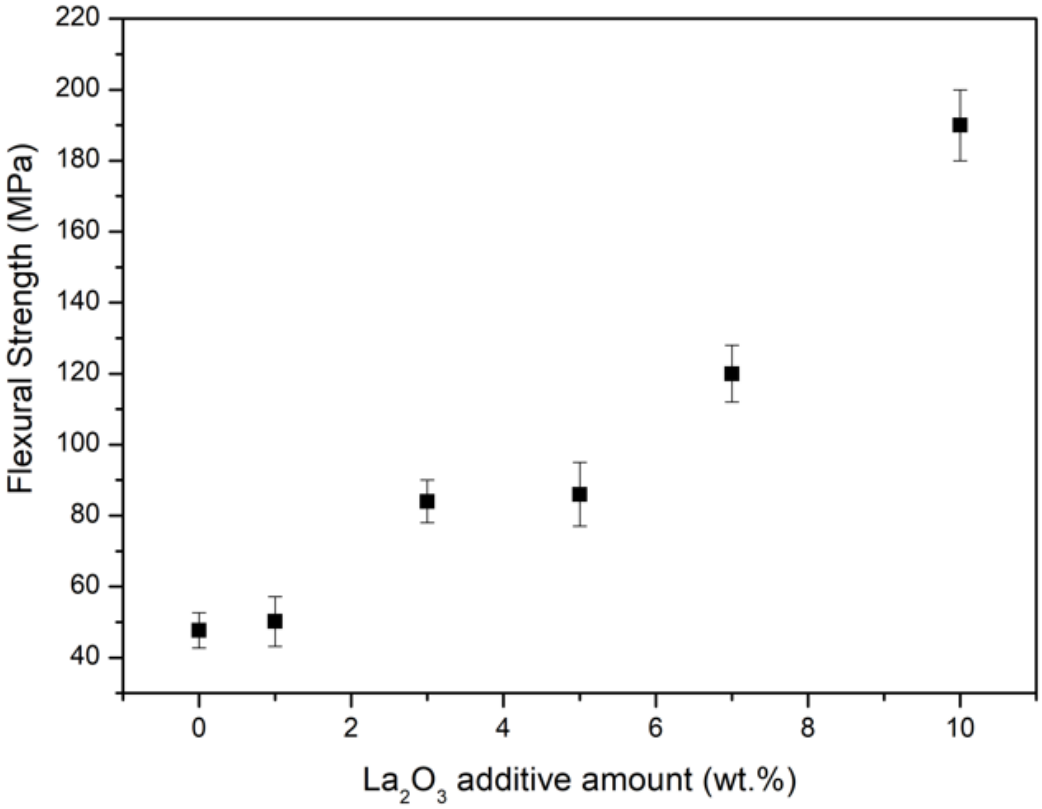


Figure 4.23. Variations of flexural strength as a function of La_2O_3 additive content

4.3.3.4 Microstructural analysis by SEM

SEM images of the fractured surfaces of MAW-1350-La1-10 samples are given below. It is clear that porosity is reduced with gradually with the increasing La_2O_3 additive content, which is in accordance with the density and linear shrinkage results. Besides, as the La_2O_3 additive content reaches to 7 wt.% elongated-shaped mullite crystals with interlocking structure becomes apparent. These mullite crystals possess curved edges and corners, indicating that their growth is realized in a liquid phase. Additionally, these mullite crystals become bigger and form an interlocking structure with further increasing La_2O_3 additive content to 10 wt.%.

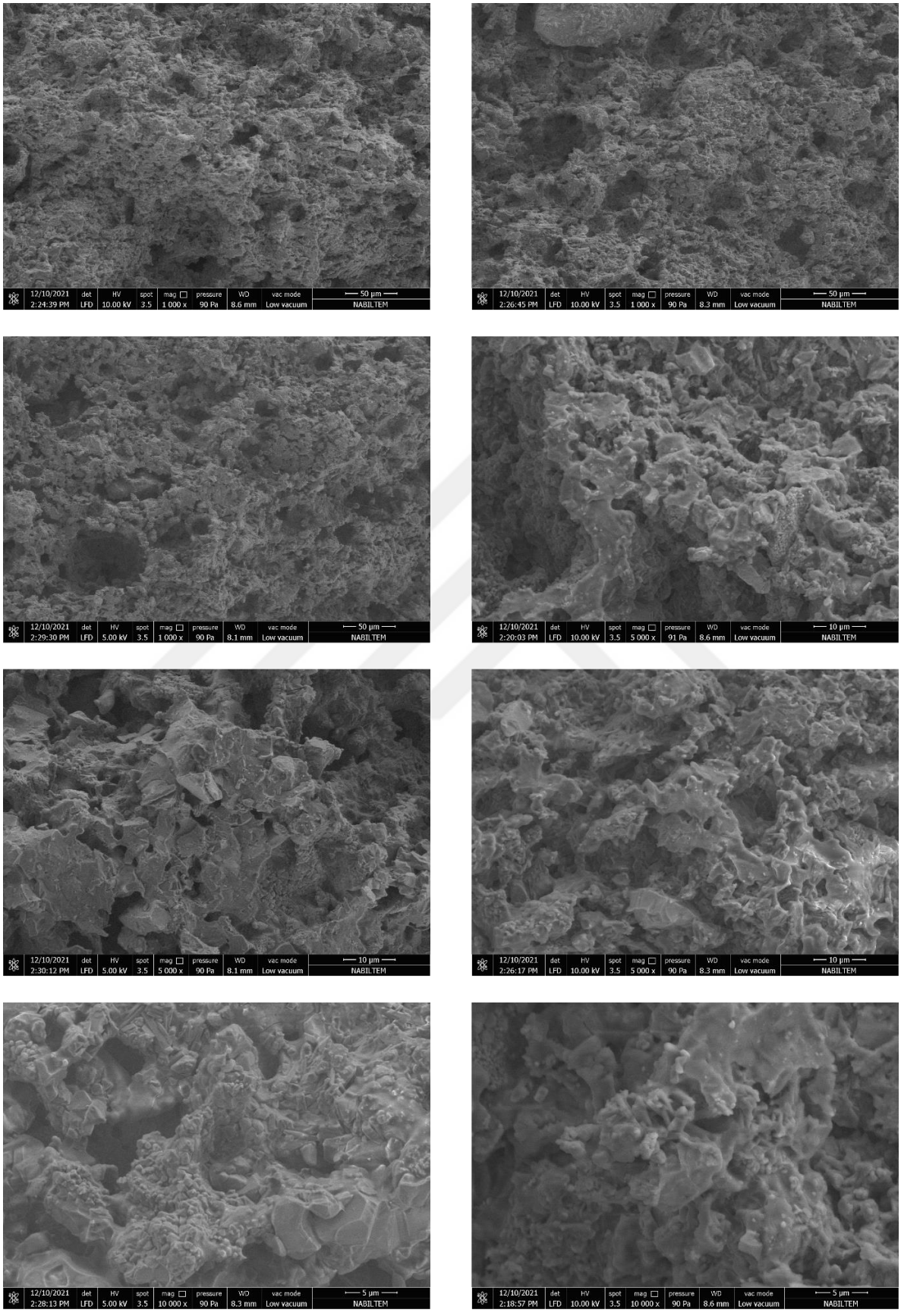


Figure 4.24. SEM images of MAW-1350-La1

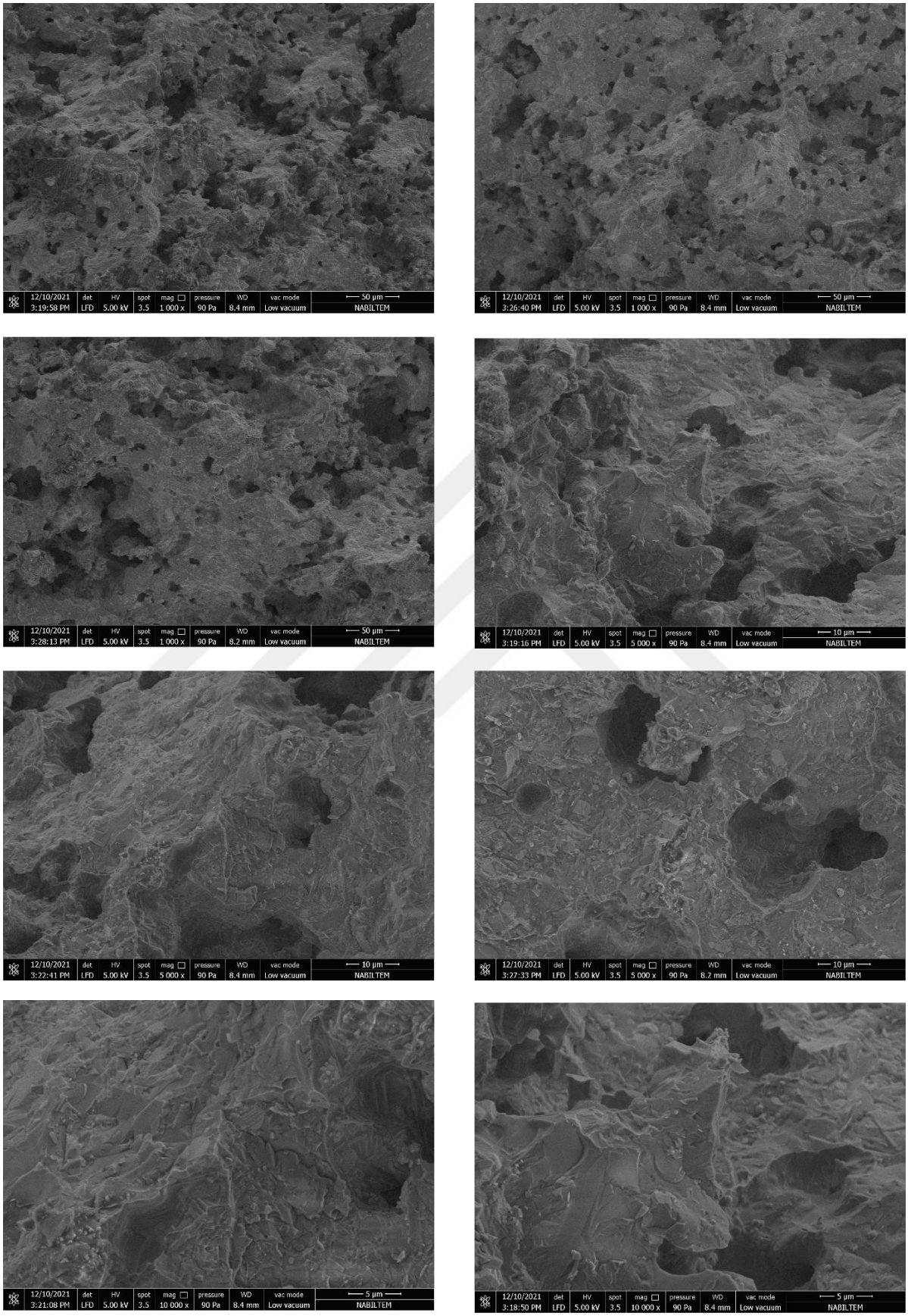


Figure 4.25. SEM images of MAW-1350-La3

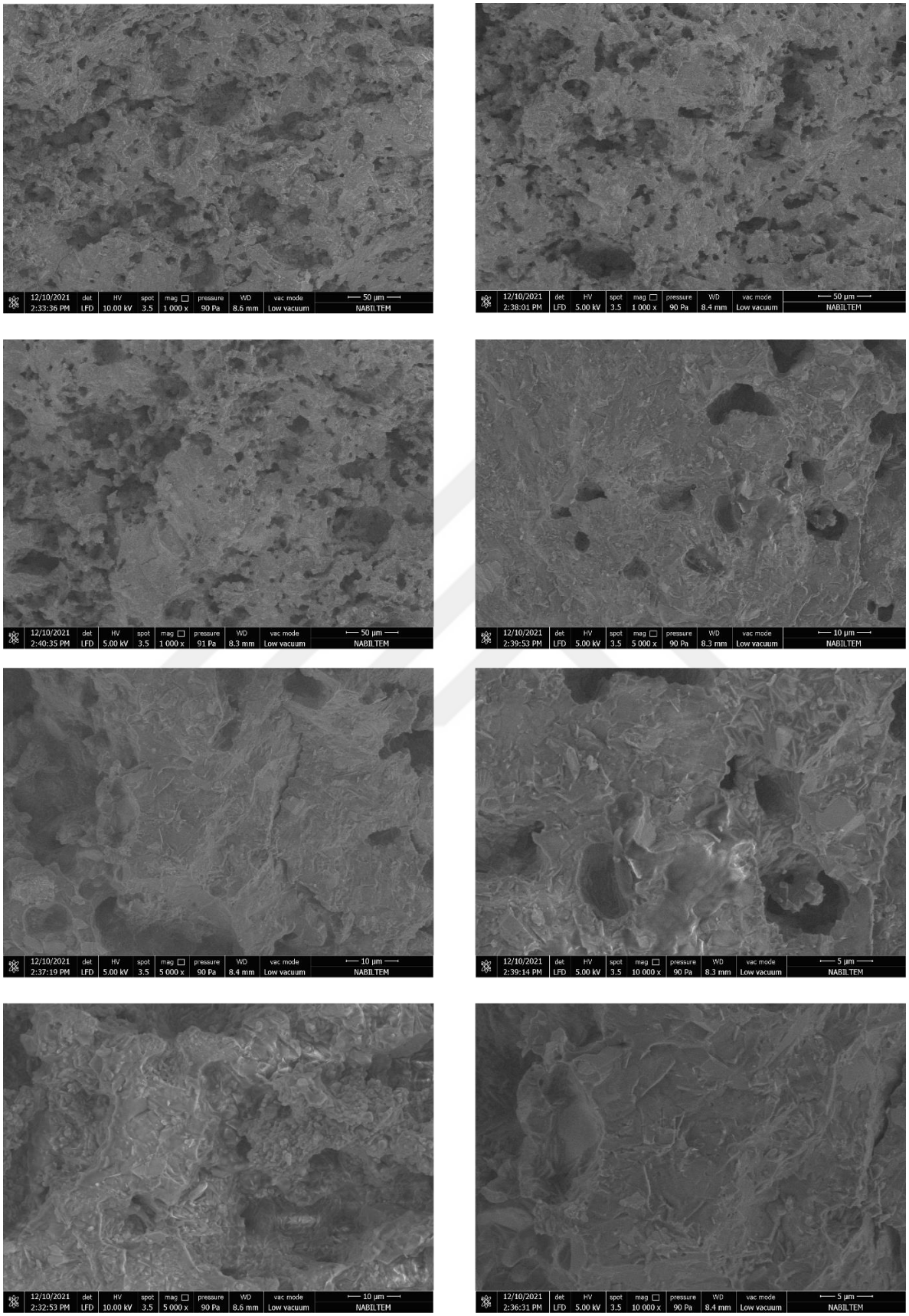


Figure 4.26. SEM images of MAW-1350-La5

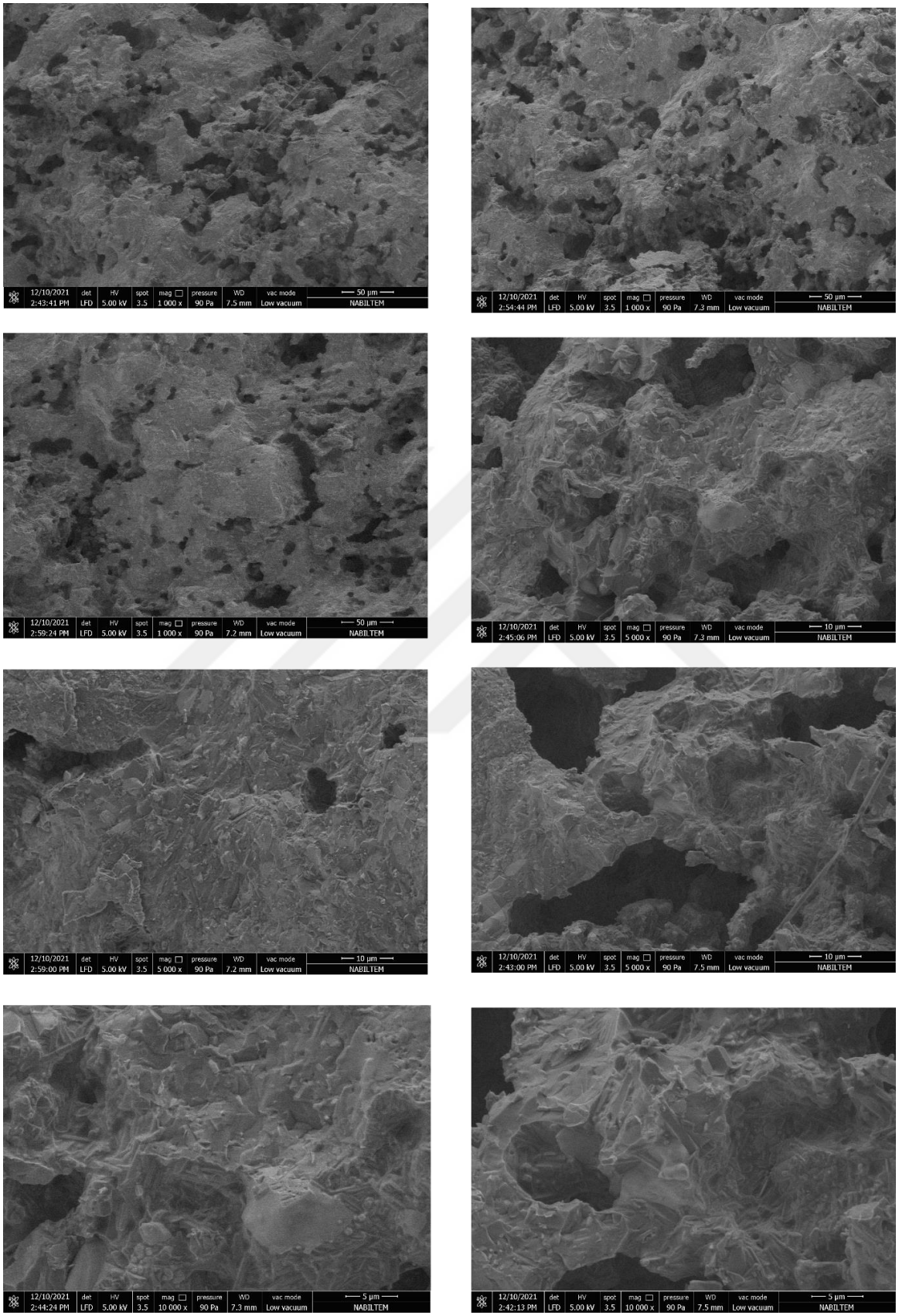


Figure 4.27. SEM images of MAW-1350-La7

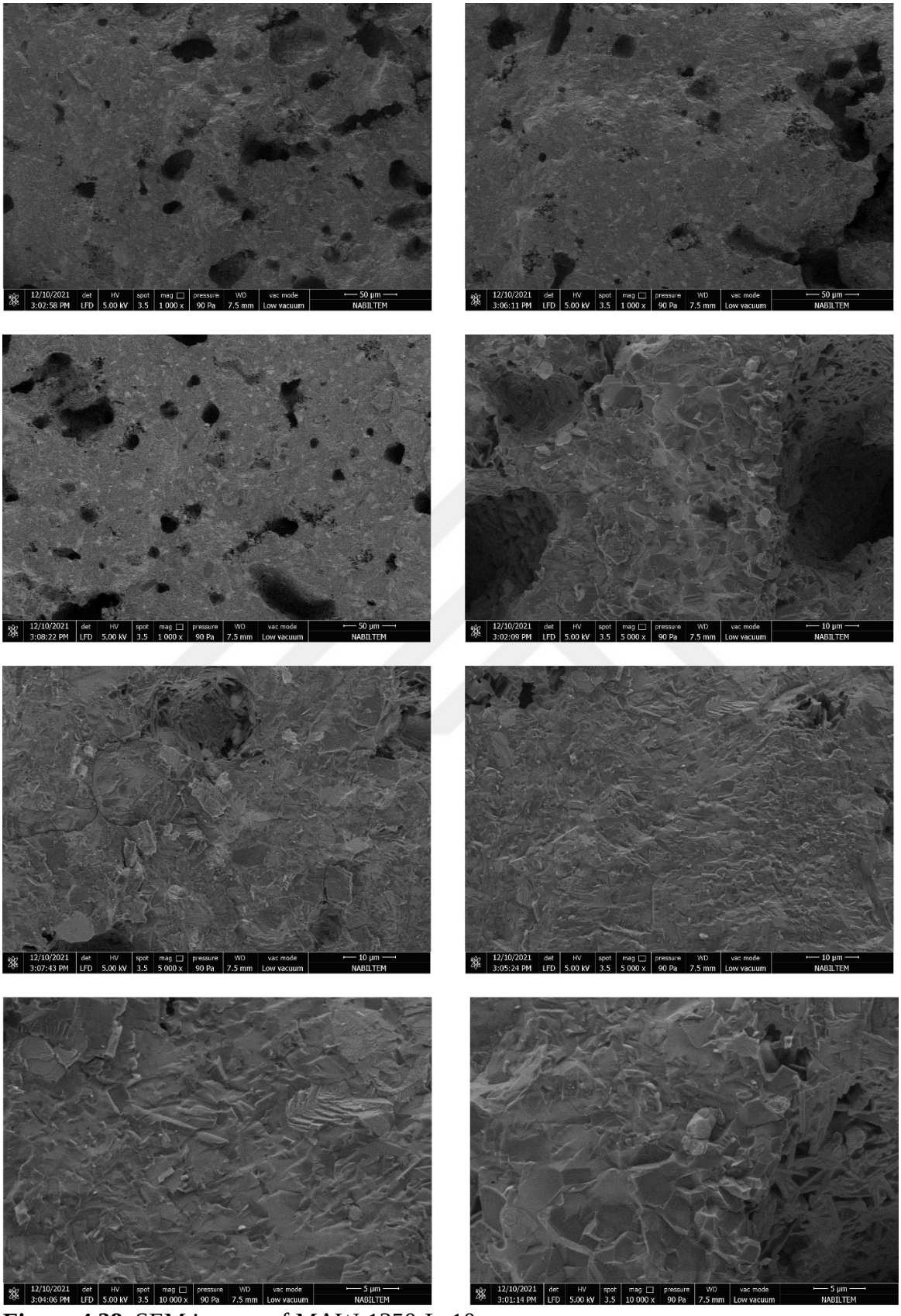


Figure 4.28. SEM images of MAW-1350-La10

4.3.4 Influence of Y_2O_3 additive

4.3.4.1 XRD analysis

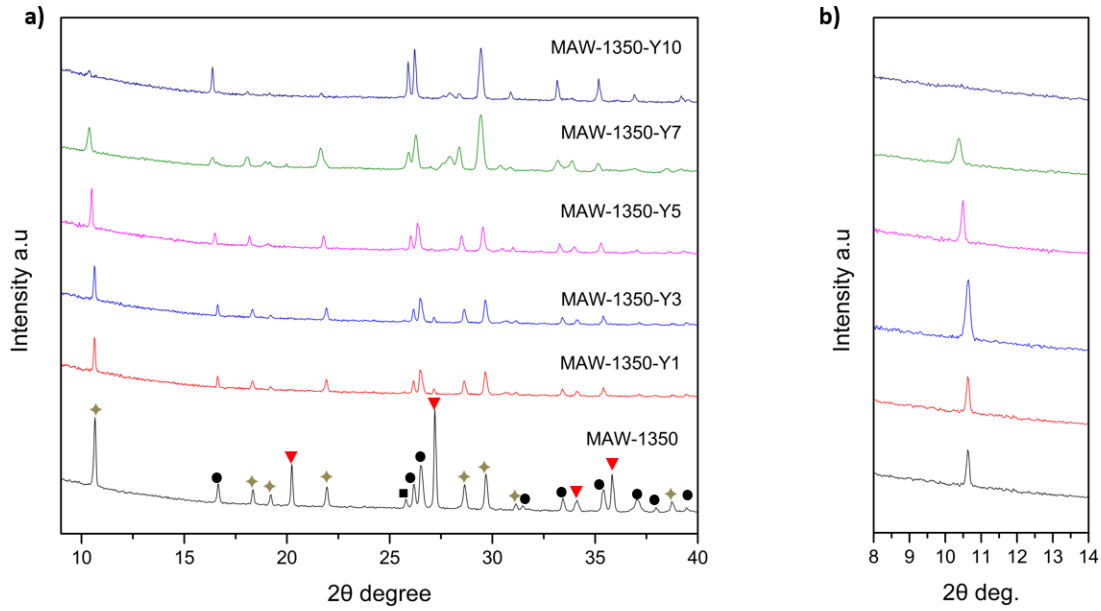


Figure 4.29. XRD patterns of the MAW-1350 and MAW-Y1-10 samples. (✦ = cordierite, ● = mullite, ▼ = zircon, and ■ = alumina)

To study the effect of the Y_2O_3 additive on the phase compositions of cordierite-based ceramic composites, five samples containing 1 to 10 wt.% of Y_2O_3 were prepared and sintered at 1350˚C for 3 h. As seen in Figure 4.29a**,** the crystalline phases in all samples containing Y_2O_3 additive are cordierite, zircon, and mullite, similar to that in the MAW-1350 composite sample.

The sharp peak observed at 2θ = 10.4° for the MAW-1350 sample belongs to the cordierite phase and is associated with the (100). This peak gradually shifted toward lower 2θ angles with the increasing Y_2O_3 additive amount in the composites **(**Figure 4.29b). This observation indicates that Y ions were doped into the cordierite lattice, leading to an increase in the unit cell volumes. Indeed, the size of Y^{3+} is considerably higher than all Al^{3+}, Si^{2+}, and Mg^{2+}. On the other hand, the intensity of the sharp peak at 2θ = 10.4° associated with the (100) plane decreases with an increasing amount of Y_2O_3 additive. This peak almost disappears for the MAW-1350-Y10 sample. Besides, the peak intensity at 2θ = 28.6° increases with the increasing Y_2O_3 additive amount. The peak at 2θ = 28.6° of the cordierite phase is associated with the (222) plane. Therefore, one can say that the

addition of the Y_2O_3 additive also alters the growth direction of the cordierite crystals. This observation becomes more pronounced when the Y_2O_3 additive content reaches 7 wt.%.

Meanwhile, the peak splitting characteristic of the cordierite phase becomes evident when Y_2O_3 additive content reaches 7 wt.% as seen from the peaks at around $2\theta = 26°$. This is due to the hexagonal to orthorhombic phase transformation. Moreover, the relative peak intensities of mullite to cordierite are also considerably increased for the MAW-1350-Y10 sample, indicating that using a large amount of Y_2O_3 additive also decreased the thermal decomposition temperature of cordierite into mullite from 1450°C.

4.3.4.2 Bulk density and apparent porosity

The bulk densities and apparent porosity for the composites containing different amounts of Y_2O_3 additive are demonstrated in Figure 4.30. The addition of Y_2O_3 noticeably improves bulk density and decreases porosity. The improved densification behavior of the composites can be ascribed to the liquid phase formation ability of the Y_2O_3 additive.

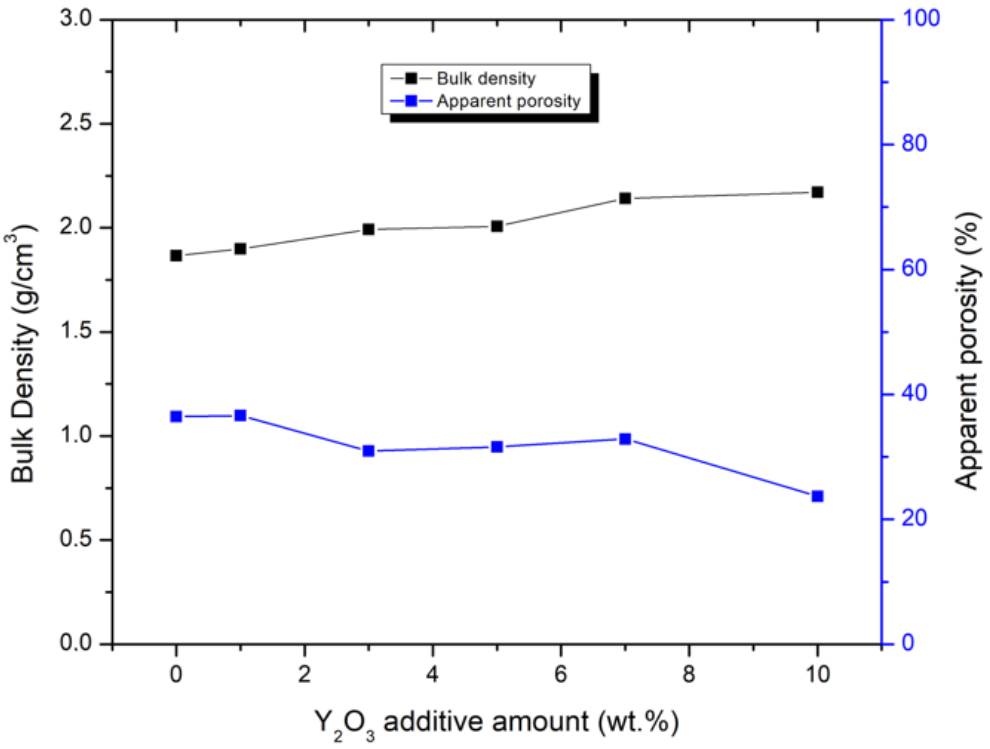


Figure 4.30. Variations of bulk density and apparent porosity as function of Y_2O_3 additive content

4.3.5 Influence of Bi_2O_3 additive

4.3.5.1 XRD analysis

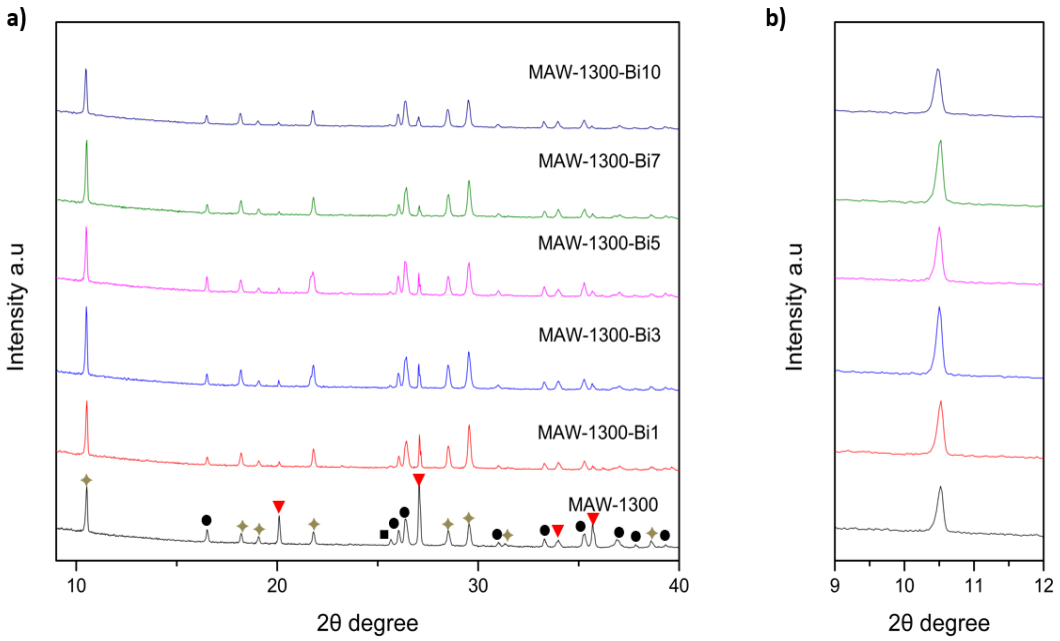


Figure 4.31. XRD patterns of the MAW-1300, and MAW-Bi1-10 samples. (✦ = cordierite, ● = mullite, ▼ = zircon, and ■ = alumina)

Figure 4.31a shows the XRD patterns of MAW-1350-Bi-1-10 samples prepared with varying amounts of Bi_2O_3 additive from 1 to 10 wt.%. The small peak belonging to the Al_2O_3 for the MAW-1300 sample clearly diminishes with the increasing amount of Bi_2O_3 additive. Meanwhile, the intensities of the peaks of the zircon phase also decrease considerably with the rising amount of the Bi_2O_3 additive in the composites. Therefore, the addition of Bi_2O_3 additive also promotes dissociation of zircon. On the other hand, one can observe from Figure 4.31b that the cordierite peaks slightly shift toward lower 2θ angles with the increasing Bi_2O_3 additive amount in the composites. This was due to the larger size of the Bi cation doped into the cordierite and enlarged unit cell volumes.

4.3.5.2 Bulk density and apparent porosity

The bulk density and apparent porosity values for the composites containing different amounts of Bi_2O_3 additive are shown in Figure 4.32. The addition of 1 wt.% Bi_2O_3 bulk

density of MAW-1300 increased from aproximately 1.7 g/cm^3 to 1.9 g/cm^3. Then, the bulk density remains almost non-altered up to 5 wt.% additive amount. Nevertheless, it gradually increases from 1.9 g/cm^3 to 2.15 g/cm^3 with a rising Bi_2O_3 additive amount. On the other hand, the apparent porosity decreases from approximately 36% to 29% with the Bi_2O_3 additive. The observed enhancement in the bulk density can be ascribed to the relatively higher atomic mass of the Bi cation and the improved densification behavior as demonstrated by the decreasing apparent porosity.

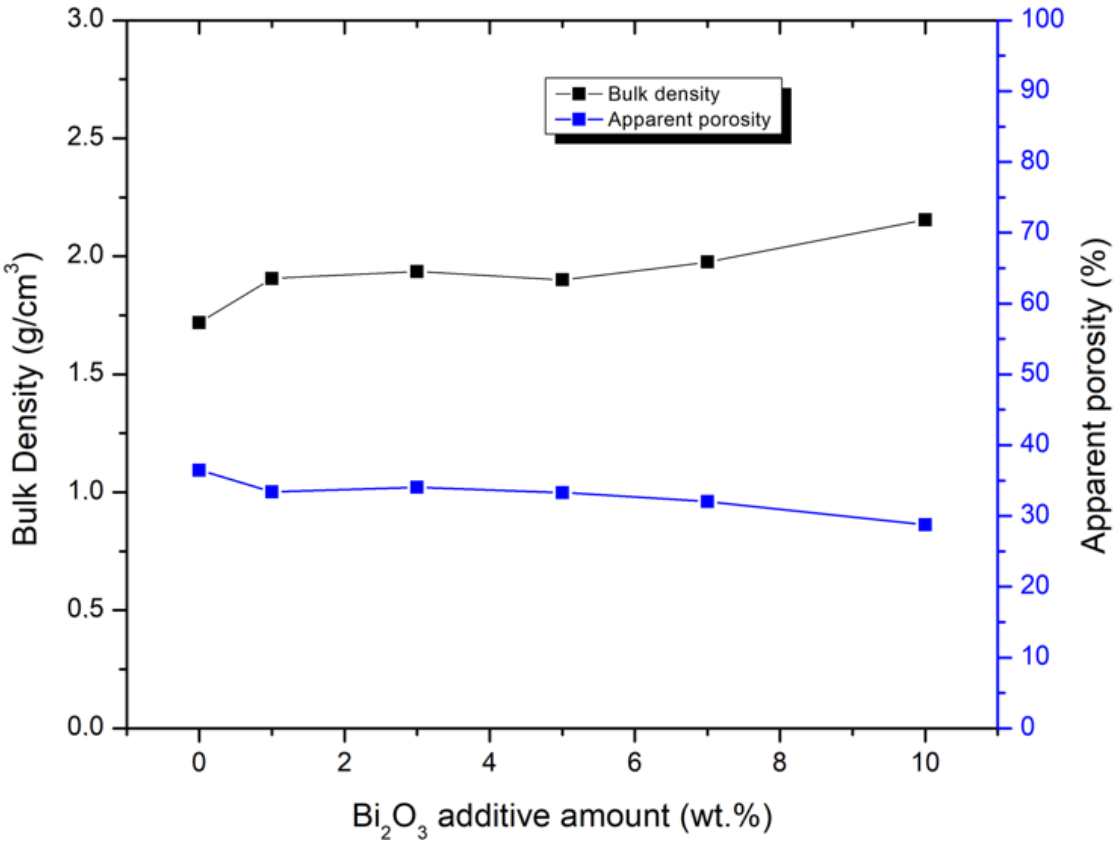


Figure 4.32. Variations of bulk density and apparent porosity as a function of Bi_2O_3 additive content

4.3.6 Influence of Ta_2O_5 additive

4.3.6.1 XRD analysis

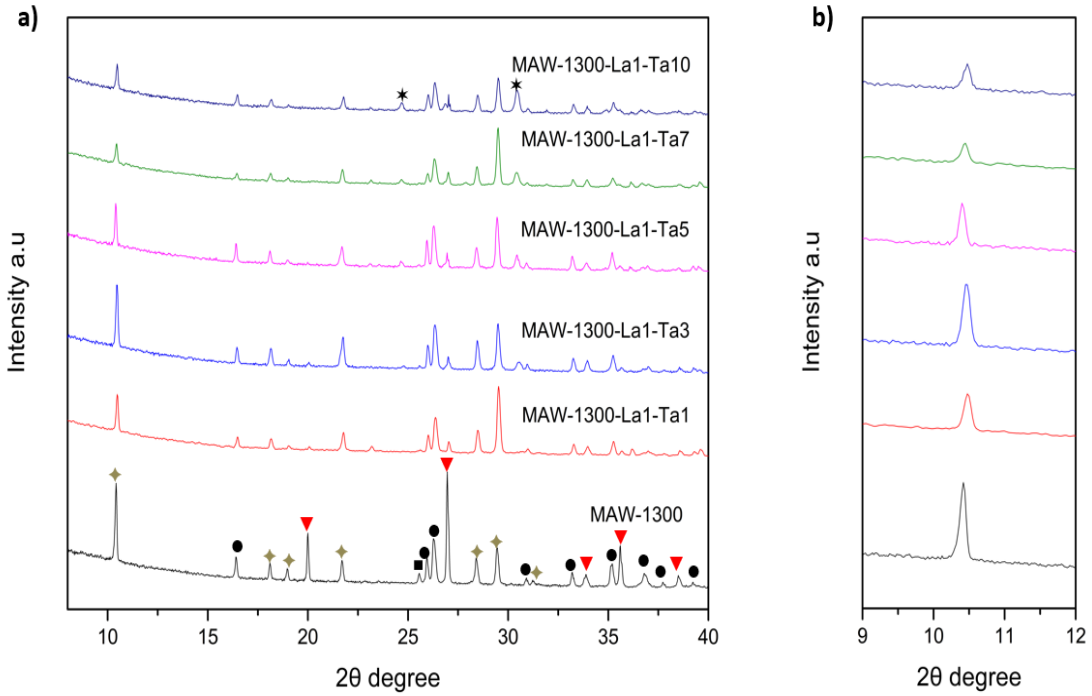


Figure 4.33. XRD patterns of the MAW-1300, and MAW-1300-La1-Ta1-10 samples. (✦ = cordierite, ● = mullite, ▼ = zircon, and ✶ = m-ZrO_2)

Figure 4.33a shows the XRD patterns of the sintered ceramic composites with the Ta_2O_5 additive. XRD patterns of the MAW-1300 and MAW-1300-La1-Ta1 composites are similar, and both mainly consist of zircon, mullite, and cordierite. With the increasing Ta_2O_5 additive amount, peaks belonging to the zircon phase diminish. When the additive amount reaches 3 wt.% peaks belonging to the monoclinic zirconia appear. Meanwhile, small alumina peaks completely disappear. This can be ascribed to the mullite formation from alumina and silica dissociated from the zircon. It is also worth noting that the intensities of the peaks belonging to the monoclinic zirconia enhanced with the increasing amount of Ta_2O_5 in the ceramic composites. On the other hand, there is no prominent peak position shifting observed for these samples because of the comparable size of the Ta cations with the other elements constituting mullite and cordierite phases.

4.3.6.2 Bulk density and apparent porosity

The influence of Ta_2O_5 additive amount on bulk density and apparent porosity values of the cordierite-based composites is shown in Figure 4.34. It is worth stressing that these samples have also been added with 1 wt.% La_2O_3. Bulk density sharply increases from approximately 1.7 g/cm^3 to about 2.17 g/cm^3 with the addition of each 1 wt.% La_2O_3 and Ta_2O_5. Then, gradually to 2.56 g/cm^3 with increasing Ta_2O_5 additive amount. Meanwhile, apparent porosity considerably decreases from 36% to almost 10% for the samples containing 7 and 10 wt.% Ta_2O_5.

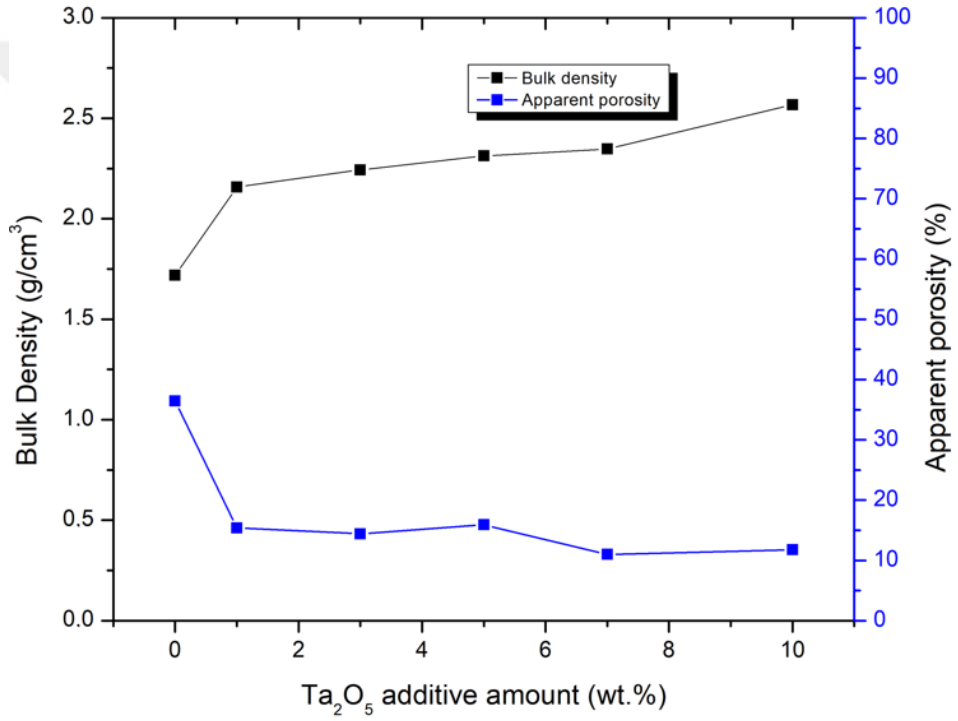


Figure 4.34. Variations of bulk density and apparent porosity as a function of Bi_2O_3 additive content

4.3.7 Influence of WO_3 additive

4.3.7.1 XRD analysis

XRD patterns of the MAW-1300-La1-W1-W10 samples are shown in Figure 4.35. It can be seen that the addition of each 1 wt.% La_2O_3 and WO_3 do not alter the phase composition of the MAW-1300 sample. Nonetheless, further increasing the WO_3 additive amount

leads to a decrease in the intensities of the peaks belonging to the zircon phase. Indeed, peaks belonging to the monoclinic zirconia are apparent for the samples containing more than 5 wt.% WO_3. Meanwhile, the peak splitting characteristic of cordierite is also evident for these samples, indicating a phase transformation towards a lower symmetry structure. Furthermore, peaks of the cordierite phase shift toward lower 2θ angles, suggesting that unit cell volumes increase with the increasing WO_3 additive amount. It is also evident that the addition of 10 wt.% WO_3 additive leads to the formation of the $MgWO_4$ phase in the composite.

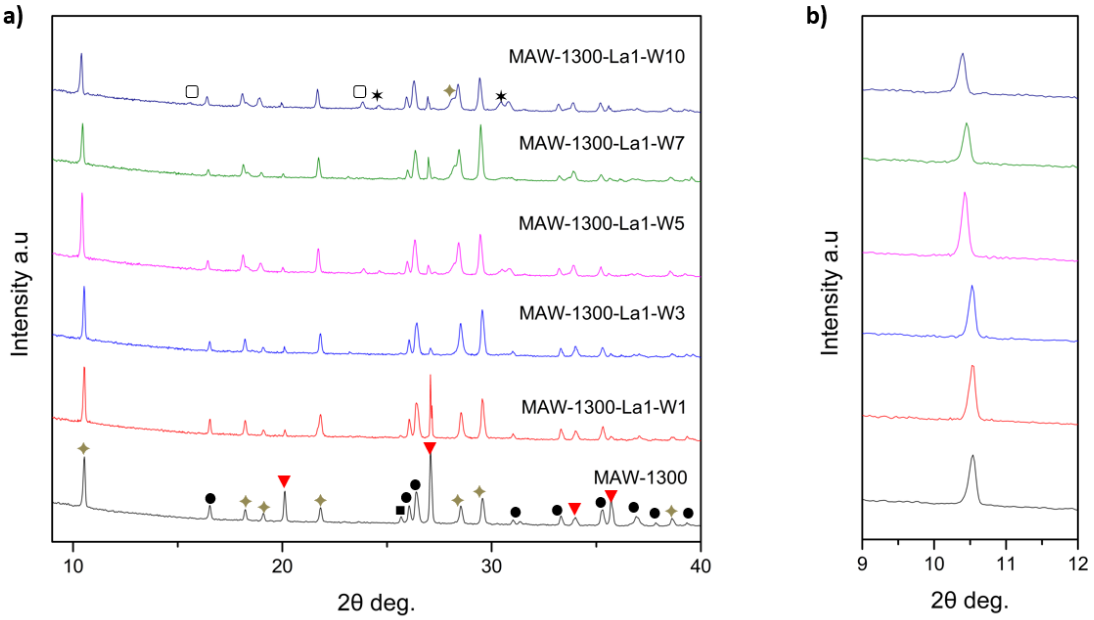


Figure 4.35. XRD patterns of the MAW-1300 and MAW-1300-La1-W1-10 samples. (✦ = cordierite, ● = mullite, ▼ = zircon, and ▢ = $MgWO_4$)

4.3.7.2 Bulk density and apparent porosity

Figure 4.36 demonstrates the bulk density variation and apparent porosity with the WO_3 additive amount. The bulk density increases gradually from approximately 1.7 g/cm^3 to 2.45 g/cm^3 with the increase of WO_3 additive from 0 to 7 wt.%. Nonetheless, further increasing the WO_3 additive amount to 7 wt.% did not significantly improve the bulk density. On the other hand, apparent porosity decreases sharply from about 36% to 11% with an increasing WO_3 additive amount to 5 wt.%. However, apparent porosity increases slightly by further increasing the WO_3 additive in the composites.

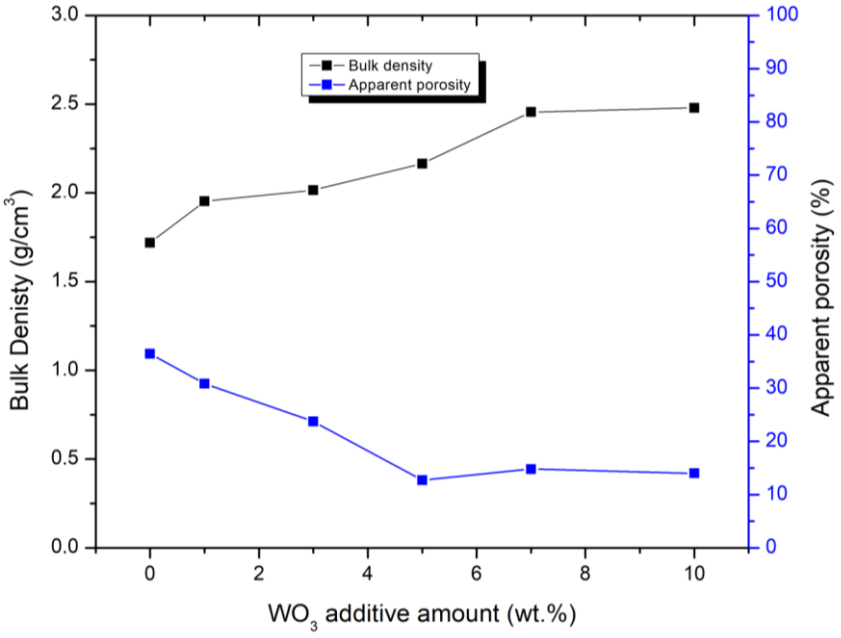


Figure 4.36. Variations of bulk density and apparent porosity as a function of WO_3 additive content

Figure 4.36 demonstrates the bulk density variation and apparent porosity with the WO_3 additive amount. The bulk density increases gradually from approximately 1.7 g/cm^3 to 2.45 g/cm^3 with the increase of WO_3 additive from 0 to 7 wt.%. Nonetheless, further increasing the WO_3 additive amount to 7 wt.% did not significantly improve the bulk density. On the other hand, apparent porosity decreases sharply from about 36% to 11% with an increasing WO_3 additive amount to 5 wt.%. However, apparent porosity increases slightly by further increasing the WO_3 additive in the composites.

4.3.8 Radiation shielding properties of cordierite-based composites

In this part of the thesis, the potential of using waste foundary sand as a starting raw material for ceramics as a radiation shield has been examined. The obtained results were evaluated comparatively for mullite and corierite ceramics.

The relative variations of mass attenuation coefficient (MAC) vs. photon energy for the cordierite-based composites in comparison with sintered waste foundry sand are presented in Figure 4.37.

The MAC of bulk samples fabricated by using only waste foundry sand at different sintering temperatures (Figure 4.37a; W-1250, W-1300, and W1350) was found to be

identical among the whole photon energy range. Since the mass attenuation coefficient (MAC) is a material-specific constant, and don't influence by density values, the obtained results are consistent. Because these samples have the same elemental composition.

The MAC variation of MAW series cordierite samples sintered at different heat-treatment temperatures (Figure 4.37b; MAW-1250, MAW-1300, and MAW1350) changes in a similar trend as W-series samples. The MAC changes of all MAW series samples were found to be the same for the whole photon energy range. The MAC changes of all MAW series samples were found to be the same for the whole photon energy range. Although the MAC changes were quite close when MAW series samples were compared to W series samples, W-series samples provided higher shielding compared to MAW series samples in regions where photoelectric effect and pair production mechanisms were dominant. The main reason for this is that some of the waste foundry sand in MAW series samples has been replaced with MgO and Al_2O_3, which have lower atomic weights.

The MAC variations of cordierite-based composites fabricated with the addition of various additives are presented in Figure 4.37c-g. The results are evidence that the MAC variation of ceramic composites increases directly proportional to the atomic number of additive elements (Y-88.9059 g, La -138.9055 g, Ta-180.9479 g, W-183.85 g, and Bi-208.9804 g). Among the all additives bismuth provided the best enhancement on the MAC because of its highest atomic number (Figure 4.37h). It is also notable that by increasing the additive amount from 1 wt.% to 10 wt.%, MAC of ceramics increased dramatically. Additionally, an extra absorption peak at around 0.1 keV photon energy was observed from Bi, Ta, and W-added ceramics MAC variation curves. This observation indicates that these elements have a K-shell absorption edge at this correlated energy level. The relative variations of linear attenuation coefficient (LAC) vs. photon energy for the cordierite-based composites are presented in Figure 4.38. The linear attenuation coefficients of the materials are related to the densities as well as the atomic weights of the elements they contain. For this reason, it is expected that the linear attenuation coefficients will differ depending on the densities of the ceramics with the same elemental composition. Graphics showing the change in linear attenuation coefficients against photon energy of W-series and MAW series samples, which have the same elemental composition are presented in Figure 4.38 a and b, respectively.

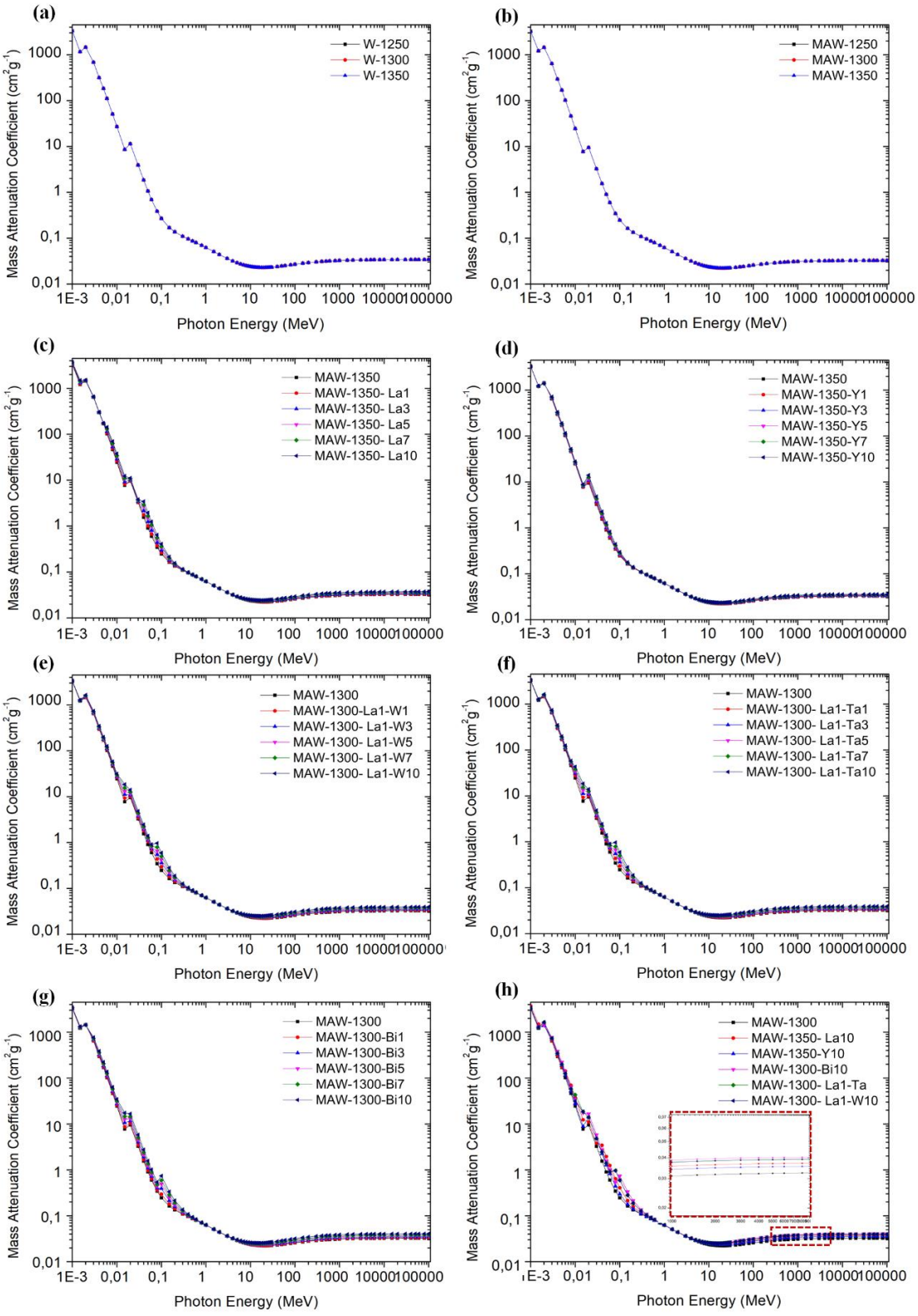


Figure 4.37. The relative variations of MAC for the cordierite based composites vs. photon energy. (a) W series, (b) MAW series, (c) MAW with La additive, (d) MAW with Y additive, (e) MAW with Bi additive, (f) MAW with La-Ta additive, (g) MAW with La-W additive, (h) camparison of MAC.

In the W-series and MAW-series samples, the best gamma atttenuation was detected in the samples coded W-1350 and MAW-1350, which had the highest density values in the series, respectively. However, the lowest gamma attenuation was observed in the samples coded W-1300 and MAW-1300, which are the samples with the lowest density in their series. As a result, it was determined that there was a direct proportional relationship between the density and gamma attenuation values in both sets, as expected.

The LAC variations of cordierite-based composites fabricated with the addition of La, Y, Bi, Ta and W elemets are presented in Figure 4.38 c-g. The results revealed that the LAC values of all element-doped samples were higher in the entire photon energy range than their undoped counterparts. The main reason for this increase is that in addition to the high atomic weight elements of the ceramic, the porous structure in the undoped samples has been removed and the density value has been increased. It was also observed that LAC values increased with the increase of elemental additive amount from 1 wt.% to 10 wt.% in all element added samples.

When single element doped samples were compared among themselves (La, Y and Bi), the highest increase in LAC value was detected in the samples produced with La additive. Although the Bi element has a higher atomic weight, the higher density of the samples produced with La addition resulted in higher gamma shielding. The main reason of observed increase in LAC of La added ceramics is the applied high sintering temperature with lanthanum oxide additive (when compared with Bi contaning ones), as well as the fact that lanthanum oxide is a very good sintering aid. When the LAC results of double-element doped samples (La-Ta and La-W) were evaluated, it was seen that both had higher shielding ability compared to mono-element samples.

Figure 4.38h shows a comparison of LAC values of ceramics according to the additive element type. It was found that La doped ceramic had higher LAC value compared to the others, followed by Ta, W and Bi added ceramics, respectively. It is seen that the addition of La increases the LAC of the ceramic at a higher rate than the elements with higher atomic weights. This finding reveals that the intensity value is the dominant parameter in radiation shielding. The relative variations of the atomic cross section and electronic cross section for the cordierite-based composites are presented in Figure 4.39 and Figure 4.40**,** respectively. The results presented in Figure 4.39 show that the atomic cross section of cordierite-based composites vary dramatically with elemental composition.

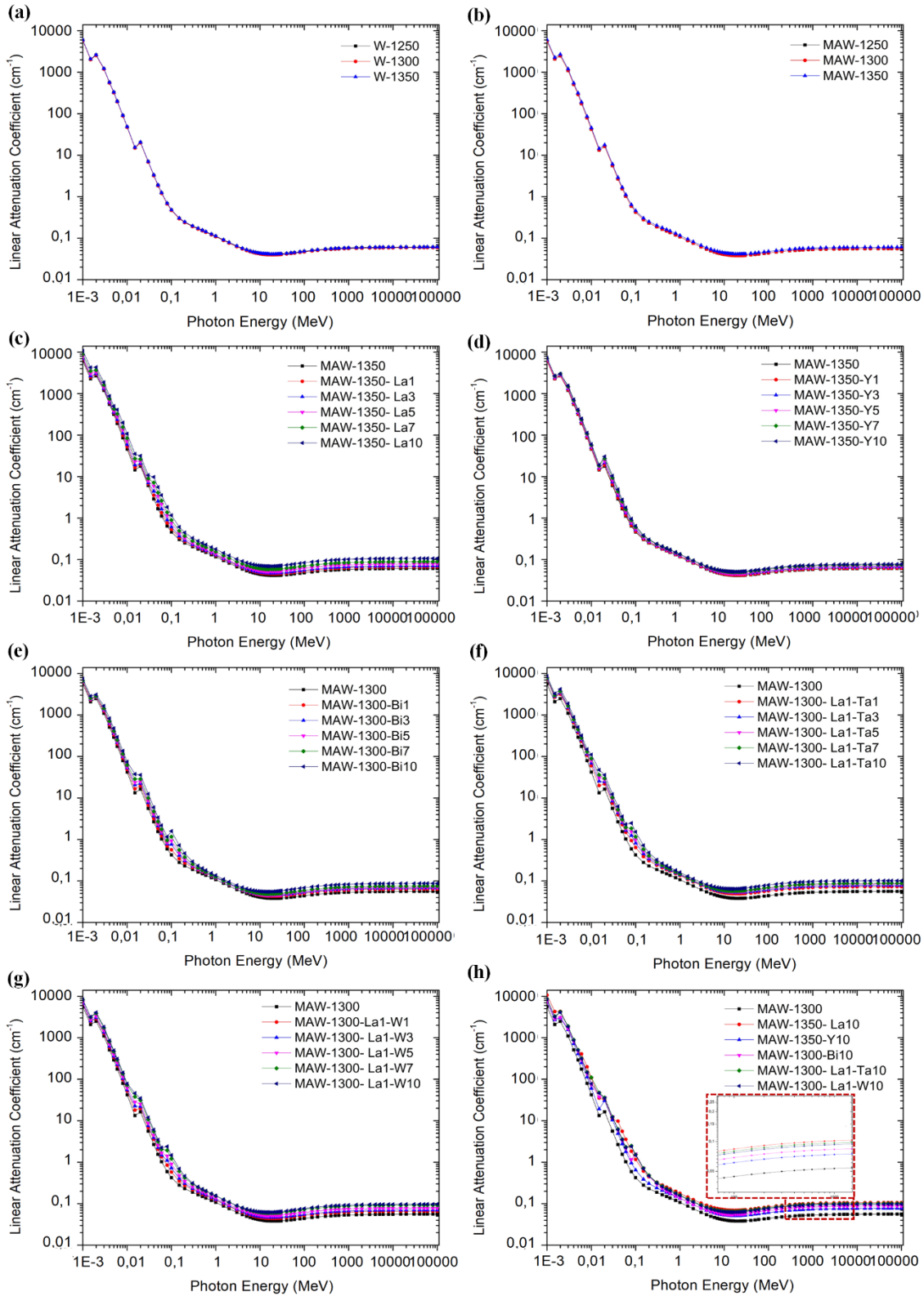


Figure 4.38. The relative variations of linear attenuation coefficient for the cordierite based composites vs. photon energy. (a) W series, (b) MAW series, (c) MAW with La additive, (d) MAW with Y additive, (e) MAW with Bi additive, (f) MAW with La-Ta additive, (g) MAW with La-W additive, (g) camparison of LAC.

It was determined that the ACS value increased with the increase in the atomic weight of the additive element and the amount in the composition. On the other hand, compositional differences caused negligible changes in the electronic cross section of cordierite-based composites (Figure 4.40). The electronic cross section values of all samples were found to be similar.

The effective atomic number (Z_{eff}) and electron density (N_{eff}) variations of ceramics are also investigated. The obtained results are presented in Figure 4.41and Figure 4.42, respectively. Z_{eff} and N_{eff} values are important parameters that give information about which photon energy of the produced material will exhibit the most effective shielding performance in radiation shielding applications. The results show that all ceramics exhibit maximum attenuation in the photon energy region of less than 1keV. The addition of additive elements to ceramics increased the effective atomic number (Z_{eff}) and electron density (Ne_{ff}) values and also increased the attenuation energy range. For all ceramics, the effective atomic number (Z_{eff}) and electron density (N_{eff}) values increased proportionally with the increase in the amount of additive in the composition. The highest effective atomic number (Z_{eff}) and electron density (N_{eff}) values were determined in MAW-Bi series samples as an additive of Bi element.

The mean free path (MFP) variations of cordierite-based composite ceramics against photon energy are presented in Figure 4.43**.** Same as fabricated mullite-based ceramics MFP values for all cordierite-based ceramic samples remain almost zero up to photon energies of roughly 30 keV. This means that photons with energies less than 30 keV cannot penetrate the fabricated ceramics. Although the MFP values steadily rise from photon energy of 30 keV to 100 keV, they remain lower than 2 cm for all ceramics. Beyond the photon energy of 100 keV, a sharper increase is observed. Meanwhile, the difference between the MFP values of the ceramic samples enlarged. For the photon energy at around 20 MeV, MFP values of W1250, W-1300, and W-1350 were determined as 24.71, 25.12, and 24.23 cm, respectively.

The MFP results of MAW-series samples show that at the same energy range, MFP values of MAW-1250, MAW-1300, and MAW-1350 are 26.15, 26.21, and 24.14 cm, respectively. Both of these findings indicate that, as a result of their higher density of W-1350 and MAW-1350, these samples prevent phonon advent in the ceramic body more effectively.

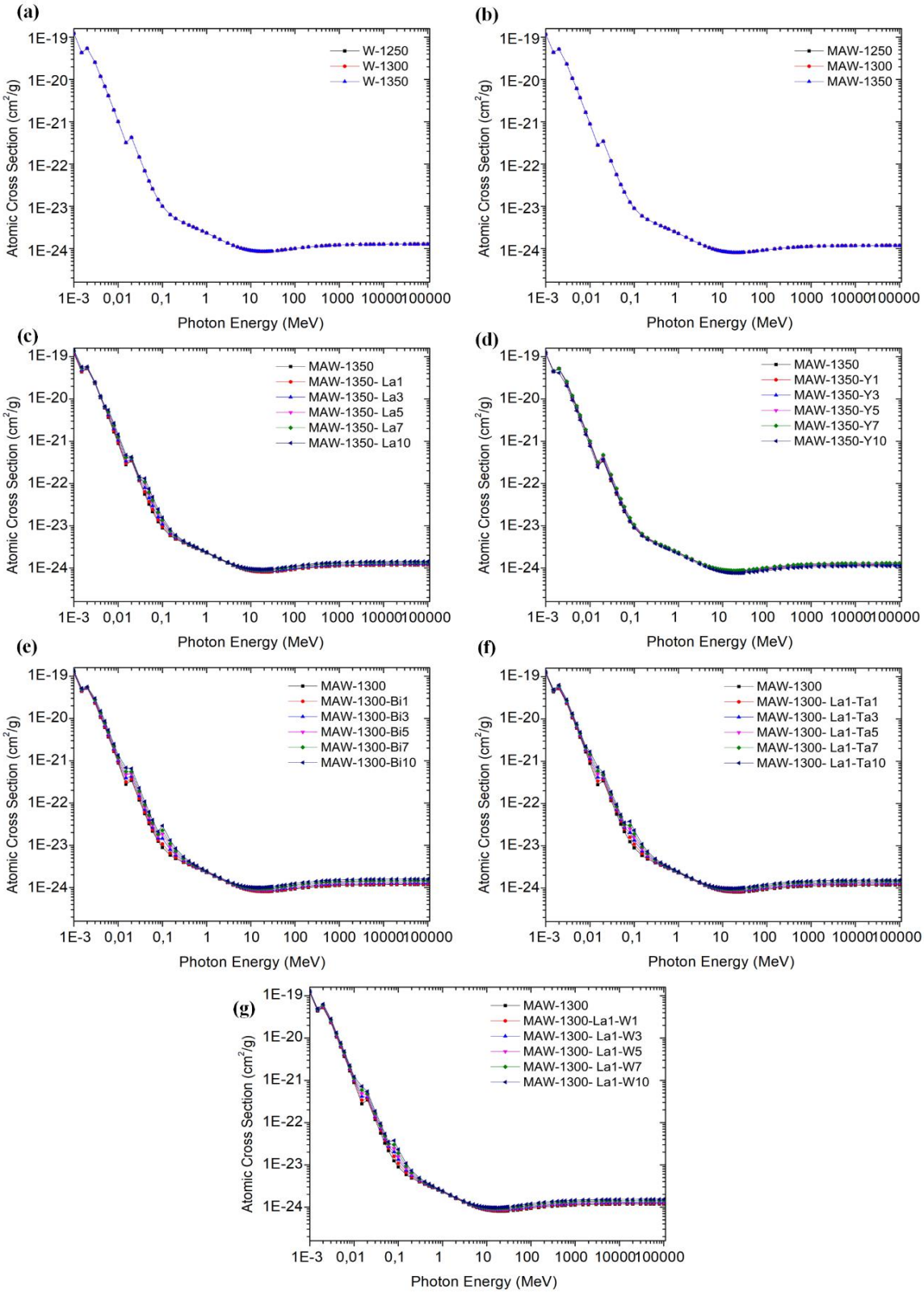


Figure 4.39. The relative variations of atomic cross section for the cordierite based composites vs. photon energy. (a) W series, (b) MAW series, (c) MAW with La additive, (d) MAW with Y additive, (e) MAW with Bi additive, (f) MAW with La-Ta additive, (g) MAW with La-W additive.

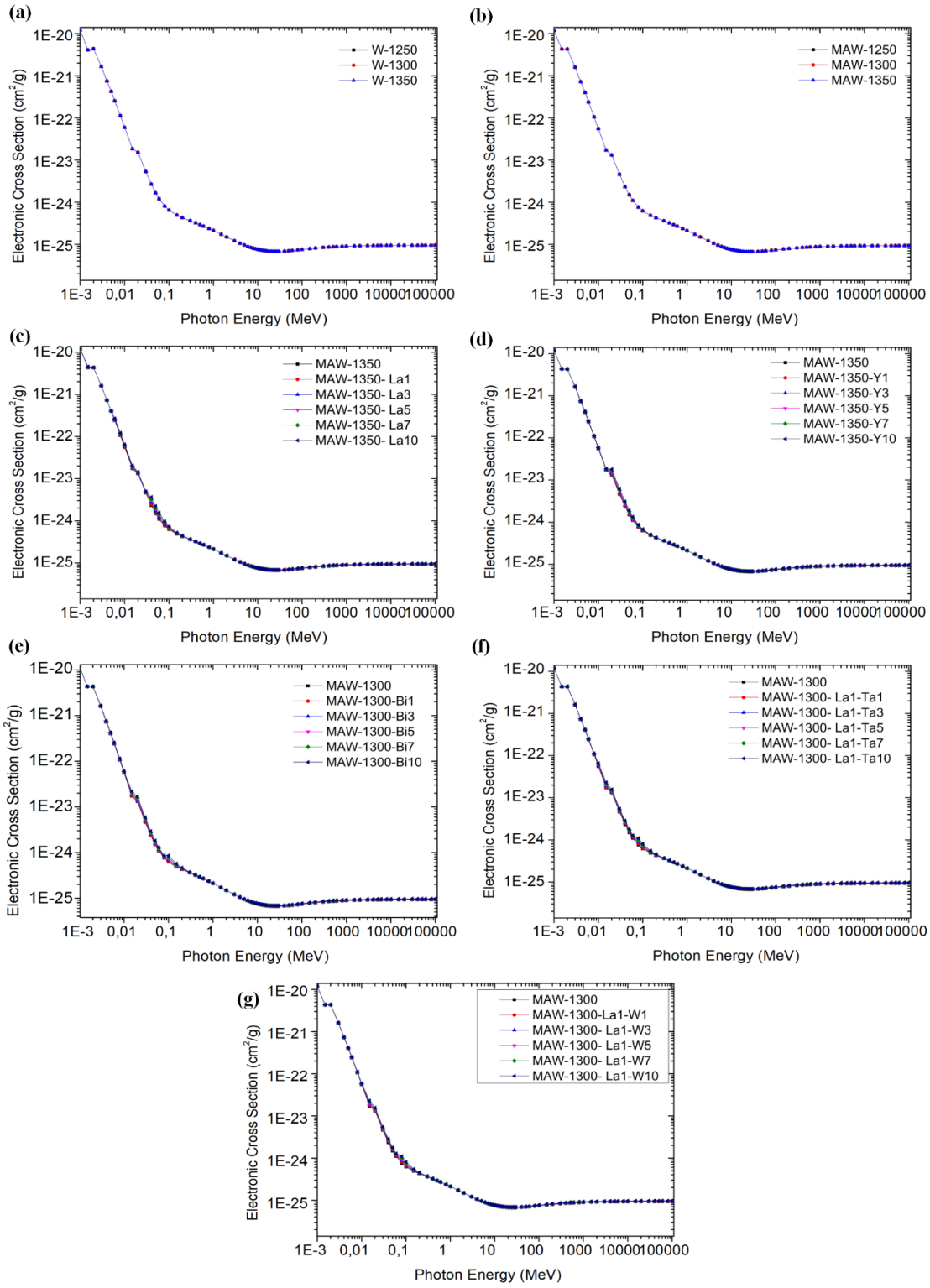


Figure 4.40 The relative variations of electronic cross section for the cordierite based composites vs. photon energy. (a) W series, (b) MAW series, (c) MAW with La additive, (d) MAW with Y additive, (e) MAW with Bi additive, (f) MAW with La-Ta additive, (g) MAW with La-W additive

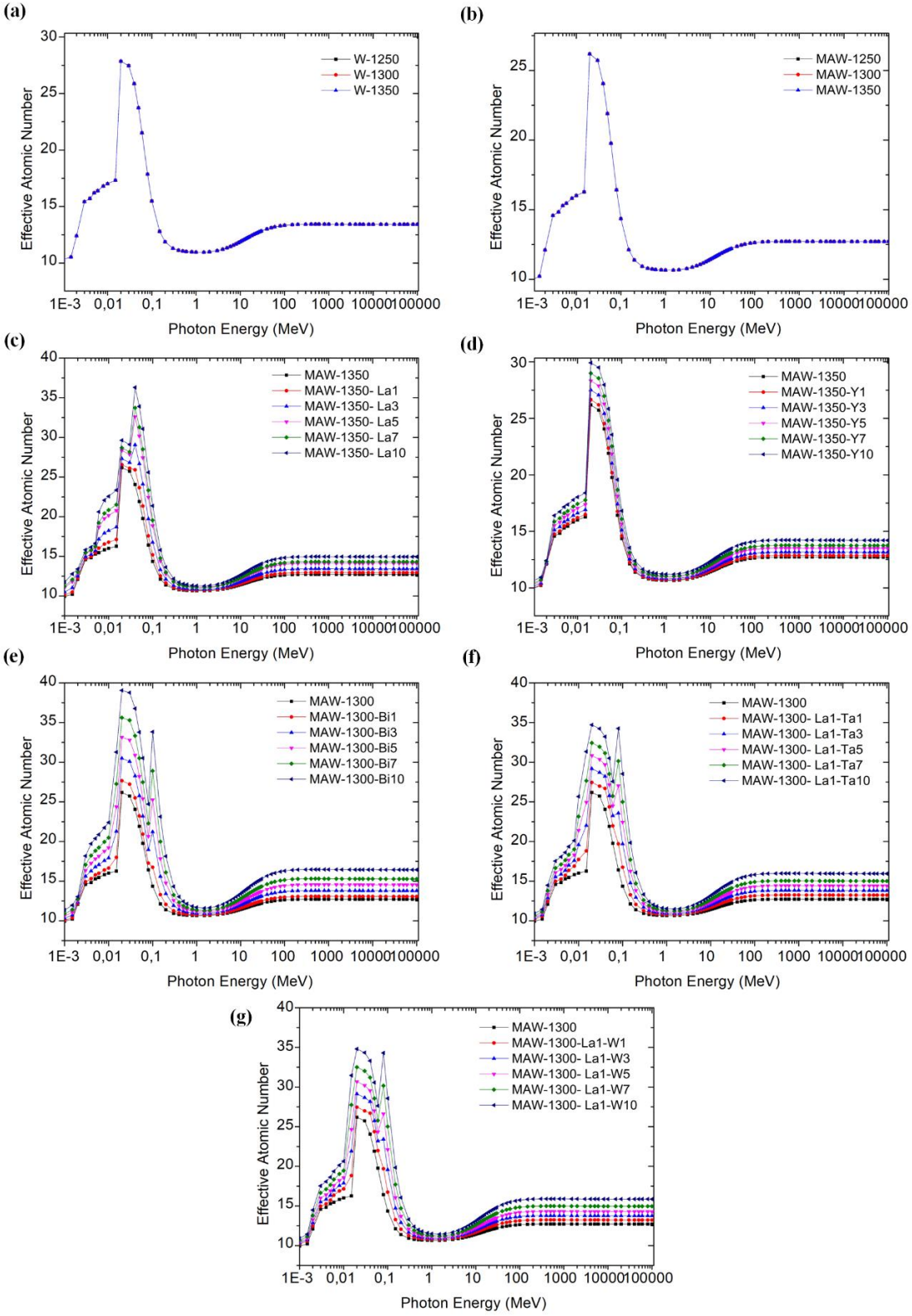


Figure 4.41. The relative variations of effective atomic number for the cordierite based composites vs. photon energy. (a) W series, (b) MAW series, (c) MAW with La additive, (d) MAW with Y additive, (e) MAW with Bi additive, (f) MAW with La-Ta additive, (g) MAW with La-W additive

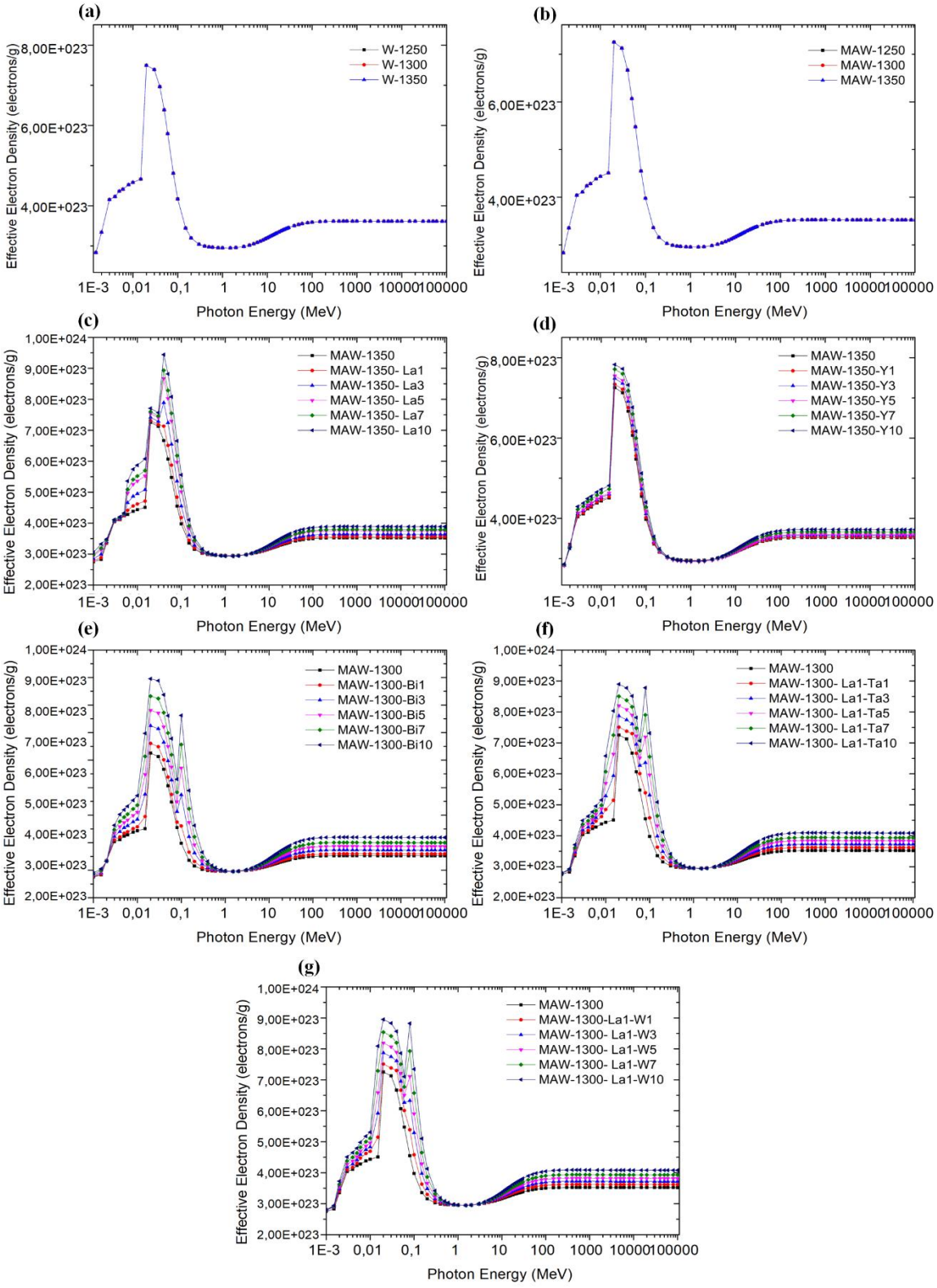


Figure 4.42. The relative variations of effective electron density for the cordierite based composites vs. photon energy. (a) W series, (b) MAW series, (c) MAW with La additive, (d) MAW with Y additive, (e) MAW with Bi additive, (f) MAW with La-Ta additive, (g) MAW with La-W additive

The “mean free path” (MFP) variations of additive-containing cordierite-based composite ceramics against photon energy are presented in Figure 4.43c-g. It was found that all additives decrease the MFP value of cordierite-based composite ceramics. This means that the addition of an additive element with a higher atomic weight to the ceramic body reduces the phonon movement efficiently. As seen from all MFP graphs, with the increase in the amount of additive material, the MFP values decreased. As seen from all MFP graphs, with the increase in the amount of additive material, the MFP values decreased. The addition of 10 wt.% La, Y, Bi, Ta, and W decrease the MFP value of ceramic to 14.38, 19.54, 18.11, 15.48, and 16.08 cm, respectively. Even though Bi is the highest atomic number element among all additives La, Ta and W prohibit phonon movement more effectively. Moreover, because La promotes the densification of waste foundry sand more than the other used additive elements, MAW-1350-La10 shows the lowest MFP value. The results reveal that the density of the ceramic body rather than the atomic weight of the element added to the ceramic body is more determinant of the MFP value.

Half- and tenth-value layers are the required material thickness to reduce incoming photon beam intensity to its %50 and %10 values, respectively. The results of the HVL and TVL examinations are presented in Figure 4.44 and Figure 4.45 It is seen that the HVL and TVL values of all W-series samples are close to each other. Among the W-series samples, W-1350 has the lowest HVL with 16.79 cm and TVL with 55.76 values at 20 MeV photon energy. The highest HVL with 17.41 cm and TVL with 57.84 cm values for the same photon energy were seen from the W-1300 sample in this series. At the same photon energy level MAW-1350 sample possesses the lowest HVL (16.73 cm) and TVL (55.6 cm) values among the MAW-series samples. The other two samples of this series show similar HVL and TVL values. At 20 MeV photon energy, MAW-1250, and MAW-1300 samples had 18.14 cm and 18.16 cm HVL values, respectively. The TVL values of MAW-1250 and MAW-1300 were found as 60.26 and 60.33 cm, respectively. The obtained results are consistent with the MFP measurement results.

The HVL and TVL variations of additive-containing cordierite-based composite ceramics were also found as consistent with MFP measurement results. From Figure 4.44c-g and Figure 4.45c-g, it is clearly seen that the incorporation of an additive element reduces the required HVL and TVL lengths. Moreover, HVL and TVL values decrease with increasing the additive amount from 1 wt.% to 10 wt.%.

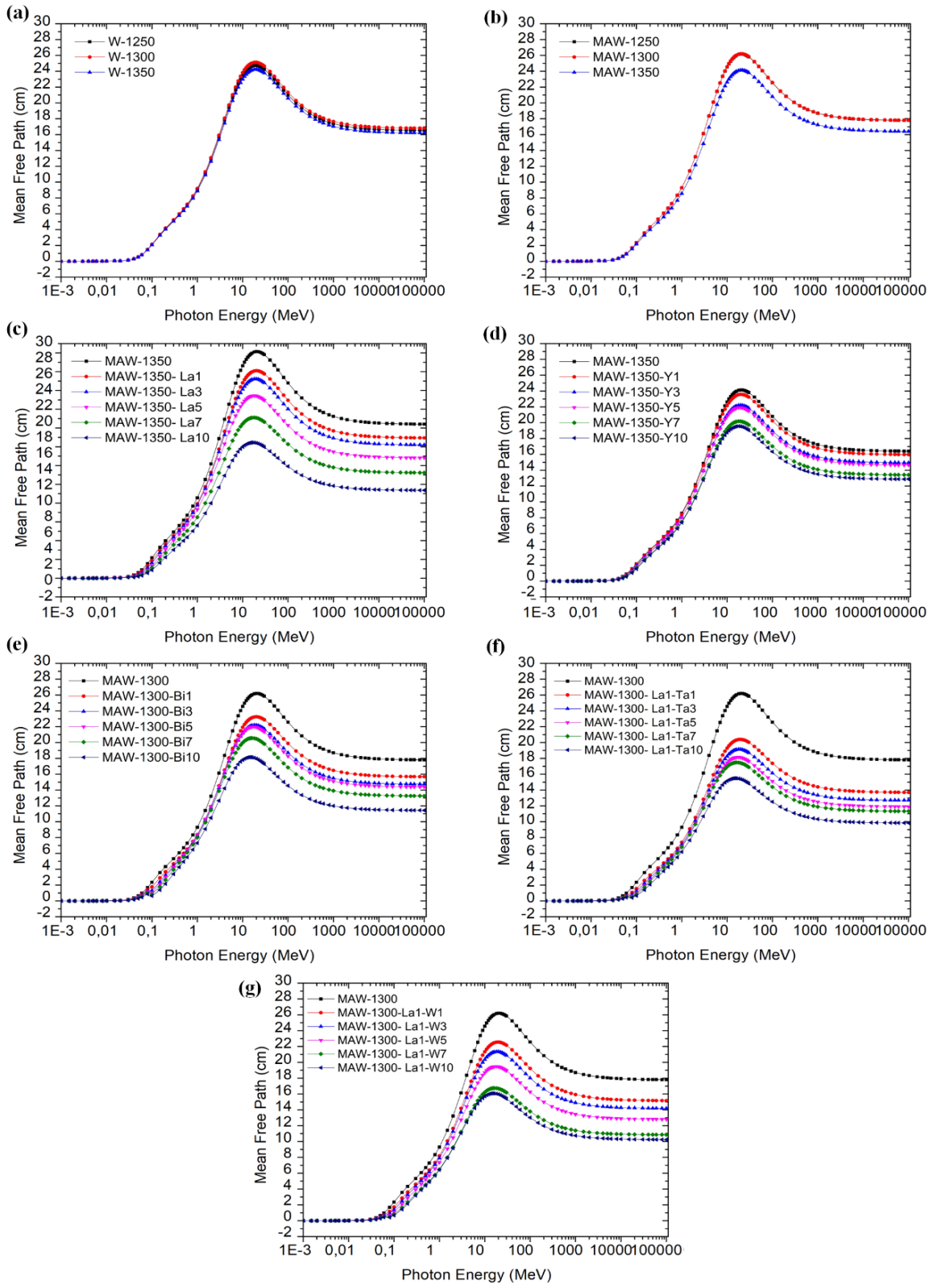


Figure 4.43. The relative variations of mean free path for the cordierite based composites vs. photon energy. (a) W series, (b) MAW series, (c) MAW with La additive, (d) MAW with Y additive, (e) MAW with Bi additive, (f) MAW with La-Ta additive, (g) MAW with La-W additive

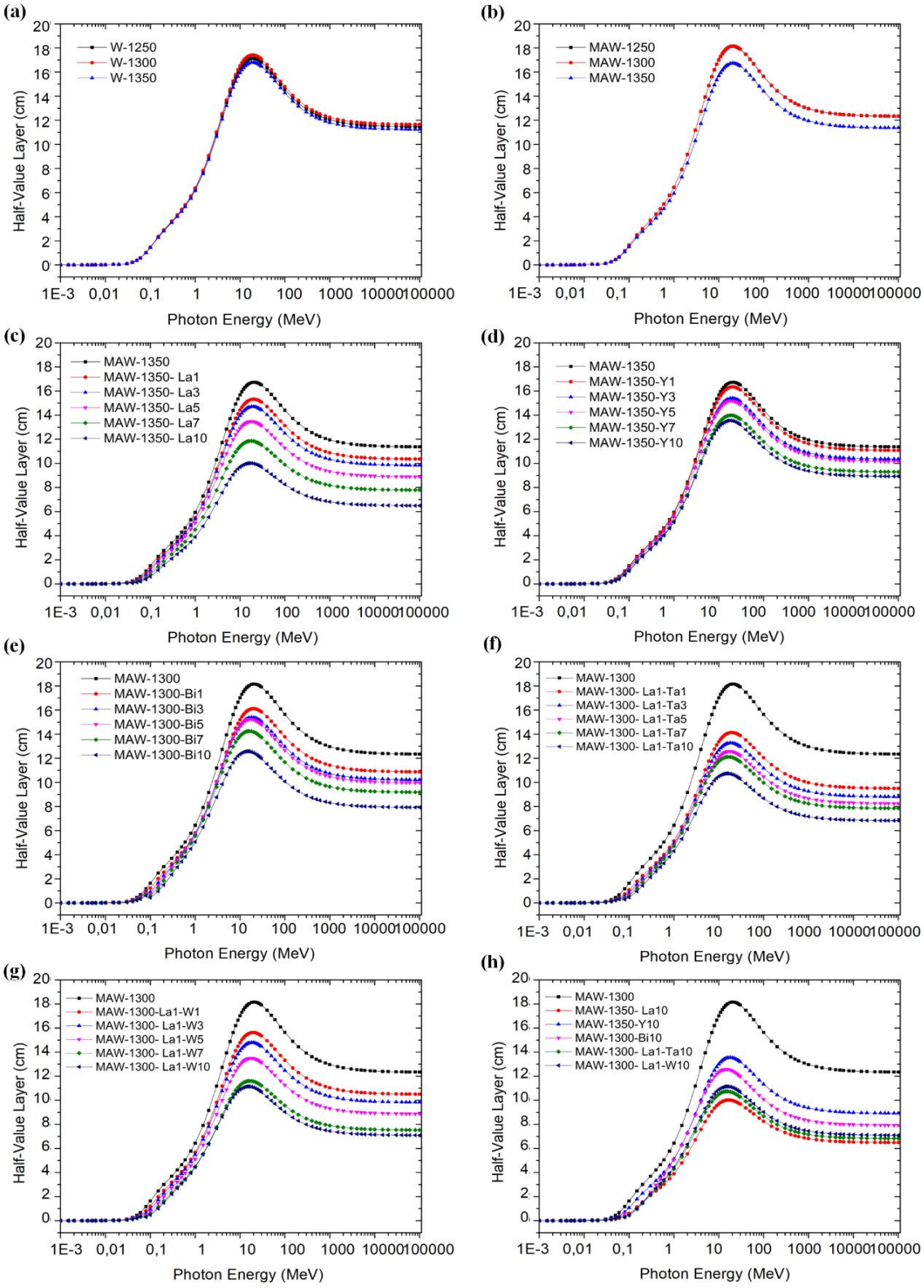


Figure 4.44. The relative variations of half-value layer (HVL) for the cordierite based composites vs. photon energy. (a) W series, (b) MAW series, (c) MAW with La additive, (d) MAW with Y additive, (e) MAW with Bi additive, (f) MAW with La-Ta additive, (g) MAW with La-W additive, (g) camparison of HVL.

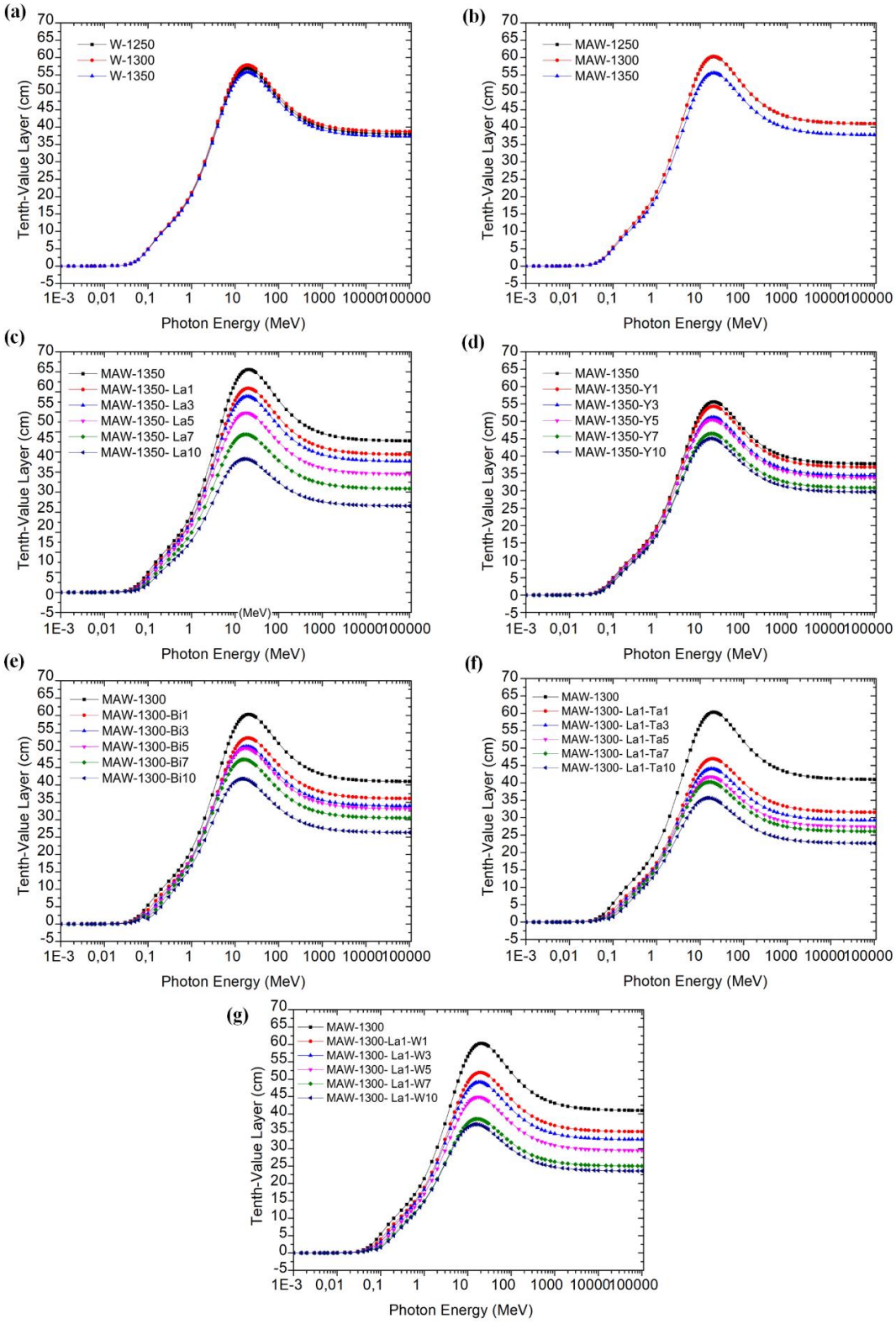


Figure 4.45. The relative variations of tenth-value layer (TVL) for the cordierite based composites vs. photon energy. (a) W series, (b) MAW series, (c) MAW with La additive, (d) MAW with Y additive, (e) MAW with Bi additive, (f) MAW with La-Ta additive, (g) MAW with La-W additive.

The results of a comparative analysis of the efficiency of the type of additive elements are presented in Figure 4.45h. The results showed that La was the most effective additive element in HVL and TVL values. At around 20 MeV photon energy, the measured HVL and TVL values of MAW-1350-LA10 are 9.99 cm and 33cm. Ta (10.6 cm), W (11.05 cm), Bi (12.46 cm), and Y (13.55 cm) elements are followed in this order to reduce the HVL value effectively.

Besides the gamma shielding performance of fabricated ceramics, neutron shielding capabilities are also investigated by simulation of their "fast neutron removal cross sections" (FNRC). The FNRC value of the material is a function of the total neutron absorption cross-sections of the elements contained in the material and the density of the material. And the FNRC constant changes in direct proportion to these variables. Comparative presentations of the fast neutron removal cross-sections of the fabricated ceramic samples are presented in Figures 46-52.

The relationship between the FNRC and the density value of fabricated W-series can be seen in Figure 4.46 W-1300 has the lowest FNRC value with 0.0566 among the w-series ceramics. In accordance with their relatively higher density values, W-1250 and W-1350 ceramics exhibit 0.0575 and 0.0586 FNRC values, respectively. A similar trend is also seen in MAW-series ceramics. As a result of the conversion of waste foundry sand to cordierite-based composite ceramics, their FNRC values slightly increased. Among the MAW-series ceramics, the highest FNRC was found in MAW-1350 with 0.0619, and the least FNRC was found in MAW-1300 with 0.0570.

Because all used additive elements have higher neutron absorption cross-sections than the elements waste foundry sand contains, all additive-containing ceramics exhibit relatively higher FNRC than their counterparts. It is clear that the FNRC value increase with increasing the additive element concentrations. However, the FNRC values of MAW-1300-Bi5 (with) and MAW-1350-La1-W10 samples were slightly lower than MAW-1300-Bi3 and MAW-1350-La1-W7, respectively. This phenomenon might be because the additive amount of these samples could not compensate for their relatively lower density values than their theoretical densities. Among all additive-containing cordierite-based ceramics, MAW-1350-La10 possesses the highest FNRC value with 0.0905. Among all 10 wt.% additives containing ceramics, Ta, W, Y, and Bi follow La with 0.0804, 0.0778, 0.0685, and 0.0671 FNRC values, respectively.

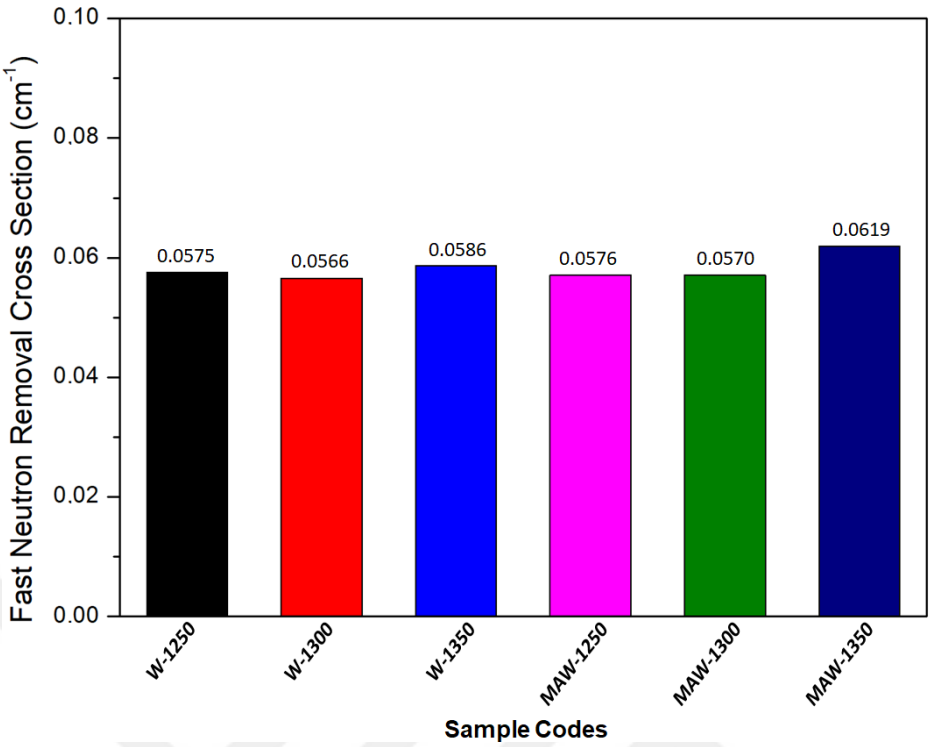


Figure 4.46. A comparative presentation of the fast neutron removal cross-sections of W- and MAW-series samples.

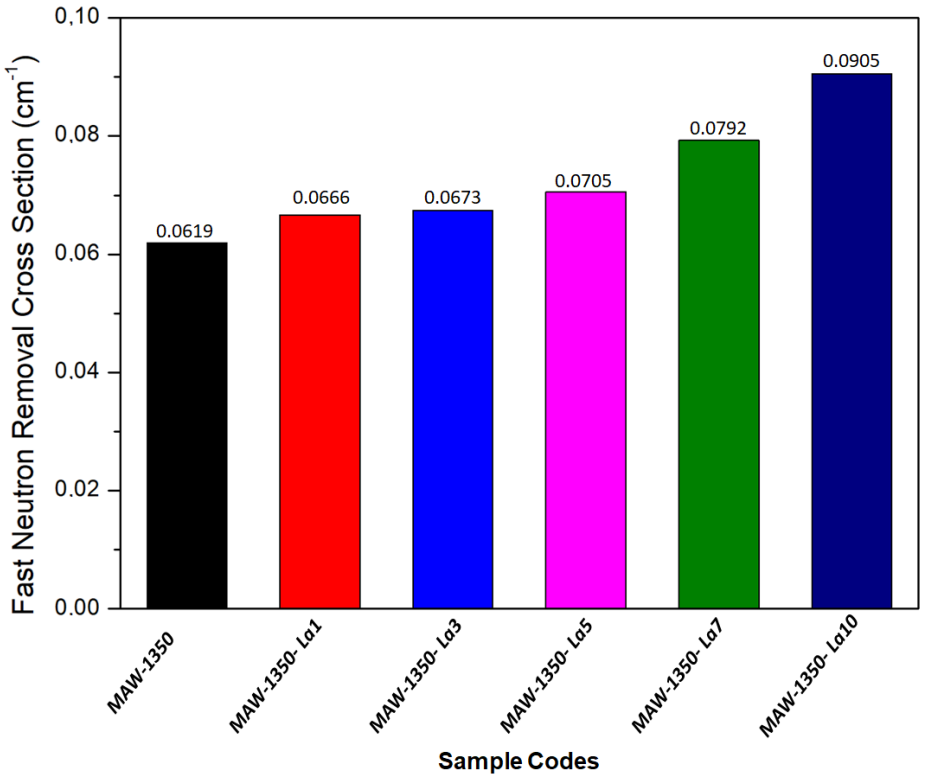


Figure 4.47. A comparative presentation of the fast neutron removal cross-sections of La containing samples.

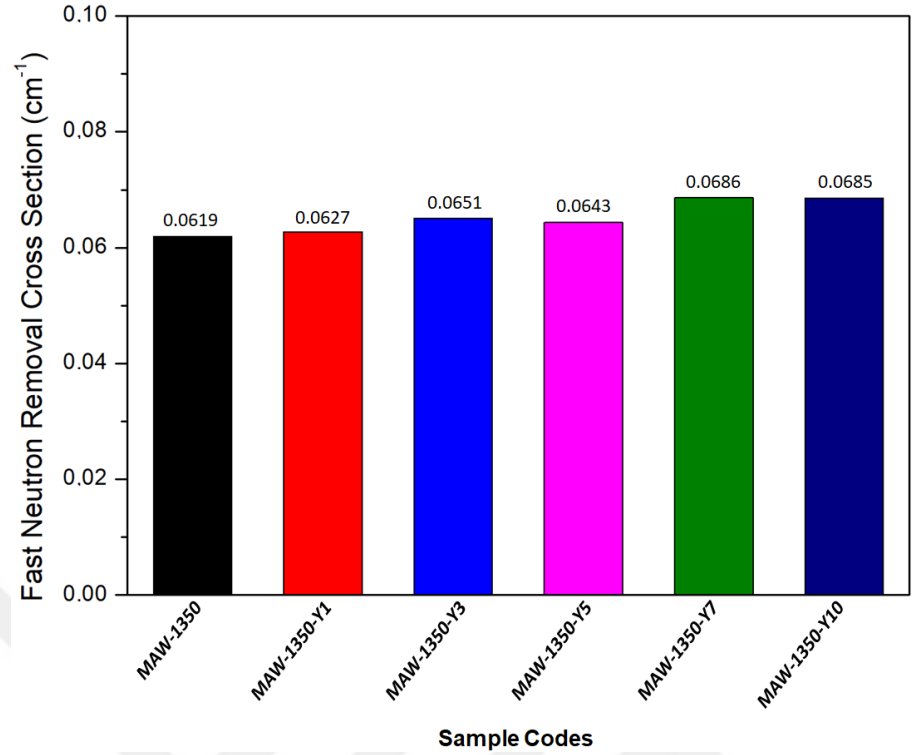


Figure 4.48. A comparative presentation of the fast neutron removal cross-sections of Y containing samples.

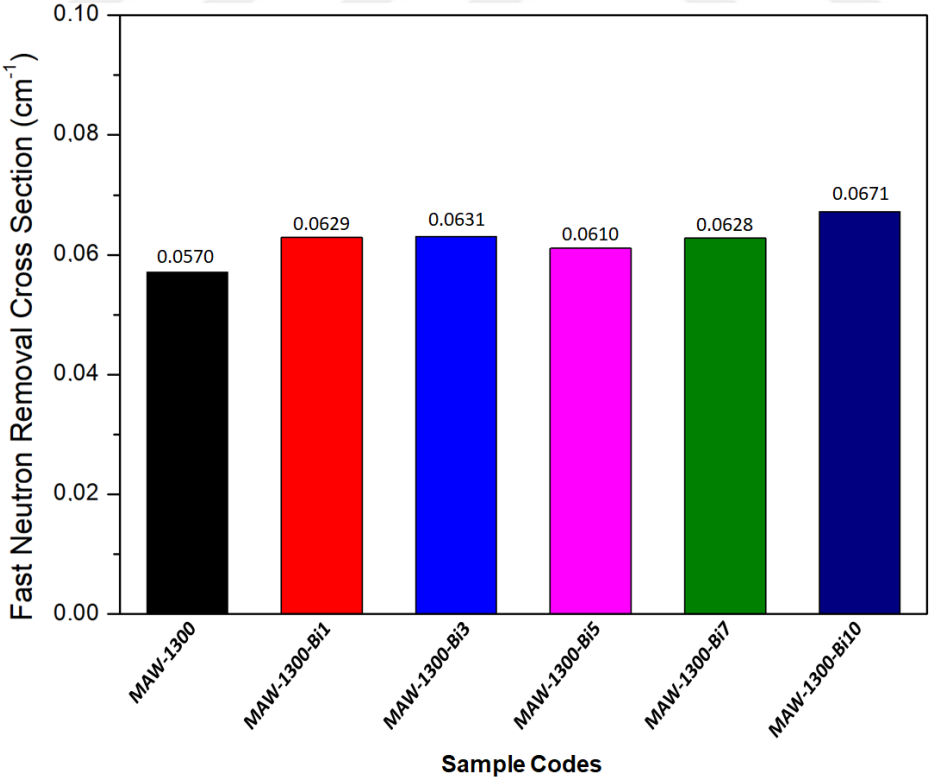


Figure 4.49. A comparative presentation of the fast neutron removal cross-sections of Bi containing samples.

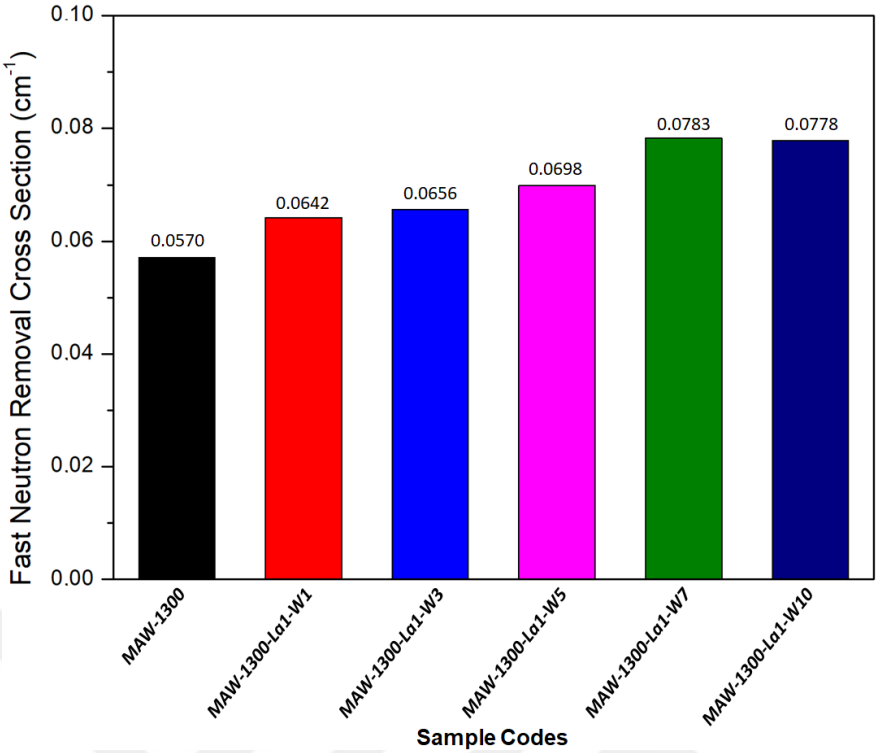


Figure 4.50. A comparative presentation of the fast neutron removal cross-sections of La-W containing samples.

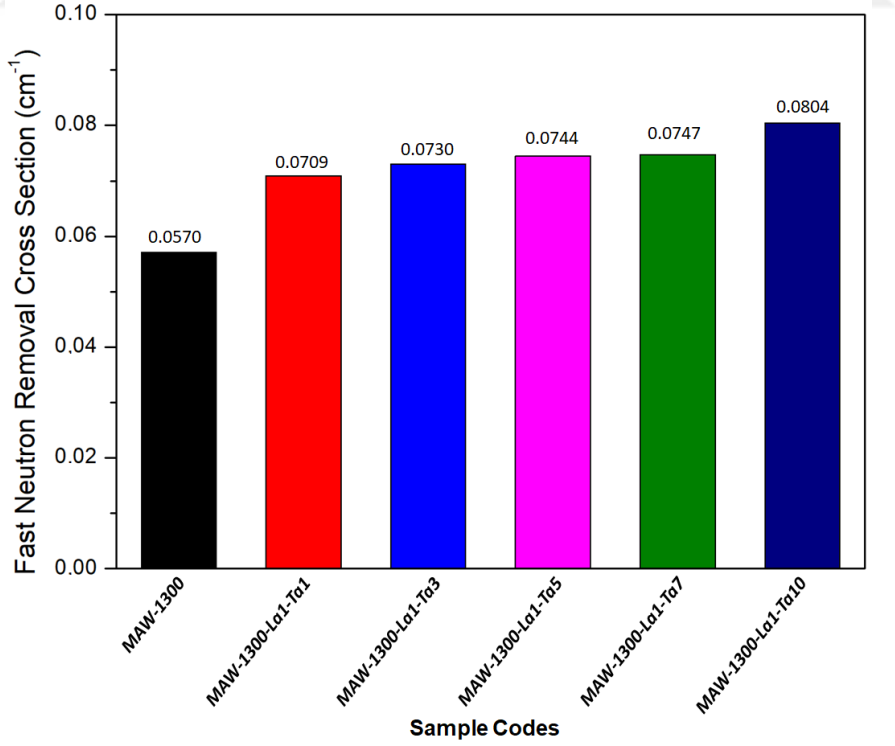


Figure 4.51. A comparative presentation of the fast neutron removal cross-sections of La-Ta containing samples.

Table 4.3. Experimental gamma shielding results of selected ceramics for Ba133-1, Ba133-2, and Cs-137 radioactive sources

Sample Names	Density (g/cm^3)	Thickness (cm)	Radiation Source		
			Ba133-1	Ba133-2	Cs-137
			Energy Values		
			81 keV	356 keV	662 keV
			Counts		
Empty Measurement	0	0	19411	127586	347515
			19274	127435	347536
			19371	127569	347632
W-1350	1.8019	0.6159	9842	106054	308807
			9927	106264	308941
			9748	106334	308774
MAW-1350	1.8658	0.627	9386	108094	309605
			9597	108035	309447
			10033	107814	309630
MAW-1350-La10	2.8564	0.5318	6938	106402	303173
			6924	106485	303838
			7130	105639	303915
MAW-1350-Y10	2.1709	0.5487	9848	104507	304642
			9513	105017	305639
			9639	104799	304503

Within the scope of the thesis, the gamma shielding parameters of four samples selected from the fabricated ceramics whose radiation shielding performance was examined theoretically and measured experimentally, and the linear and mass attenuation coefficients of these samples were calculated in light of the data obtained. Three measurements were taken from each sample using three different radioactive sources emitting photons at different energies.

Table 4.4. Experimentally obtained linear attenuation coefficient (μ) values of selected ceramics

	Linear Attenuation Coefficient (μ)-Experimental			
Energy (MeV)	**W-1350**	**MAW-1350**	**MAW-1350-La10**	**MAW-1350-Y10**
8.10E-02	1.0983	1.1062	1.9129	1.2650
3.56E-01	0.2969	0.2654	0.3446	0.3582
6.62E-01	0.1918	0.1847	0.2540	0.2385

Table 4.5. Experimentally obtained mass attenuation coefficient (μ/d) values of selected ceramics

	Mass Attenuation Coefficient (μ/d)-Experimental			
Energy (MeV)	**W-1350**	**MAW-1350**	**MAW-1350-La10**	**MAW-1350-Y10**
8.10E-02	0.6095	0.5929	0.6697	0.5827
3.56E-01	0.1648	0.1422	0.1206	0.1650
6.62E-01	0.1064	0.0990	0.0889	0.1099

In addition, the measurement was taken without placing the sample between the detector and the source in order to obtain the I_0 value. Obtained experimental data are presented in Table 4.3. In addition, the linear and mass attenuation coefficients were calculated by using the thickness and density values of the samples and the results are presented in Tables 4.4 and 4.5.

Comparative values of linear and mass attenuation coefficients calculated from experimental and computational data are presented in Figure 4.52 and Figure 4.53. The results obtained show that the experimental and computational data are consistent with each other. As in the computational results, the experimental data show that the linear and mass attenuation coefficients of W-1350 produced only from waste powder and MAW-1350 converted to cordierite are quite close to each other. In comparison, measurements with a low-energy radioactive source (Ba133-1; 81 keV) MAW-1350 showed better attenuation than W-1350. In addition, at higher photon energy (Ba133-2;356 keV and Cs-137;662 keV), W-1350 showed better attenuation than MAW-1350.

Similarly, comparative values of linear and mass attenuation coefficients calculated with experimental and computational data were found to be consistent. It was observed that both additives increased the gamma attenuation value of the ceramics. Especially in the measurements made with the low energy source (Ba133-1; 81 keV), the La doped sample showed much higher performance compared to the others.

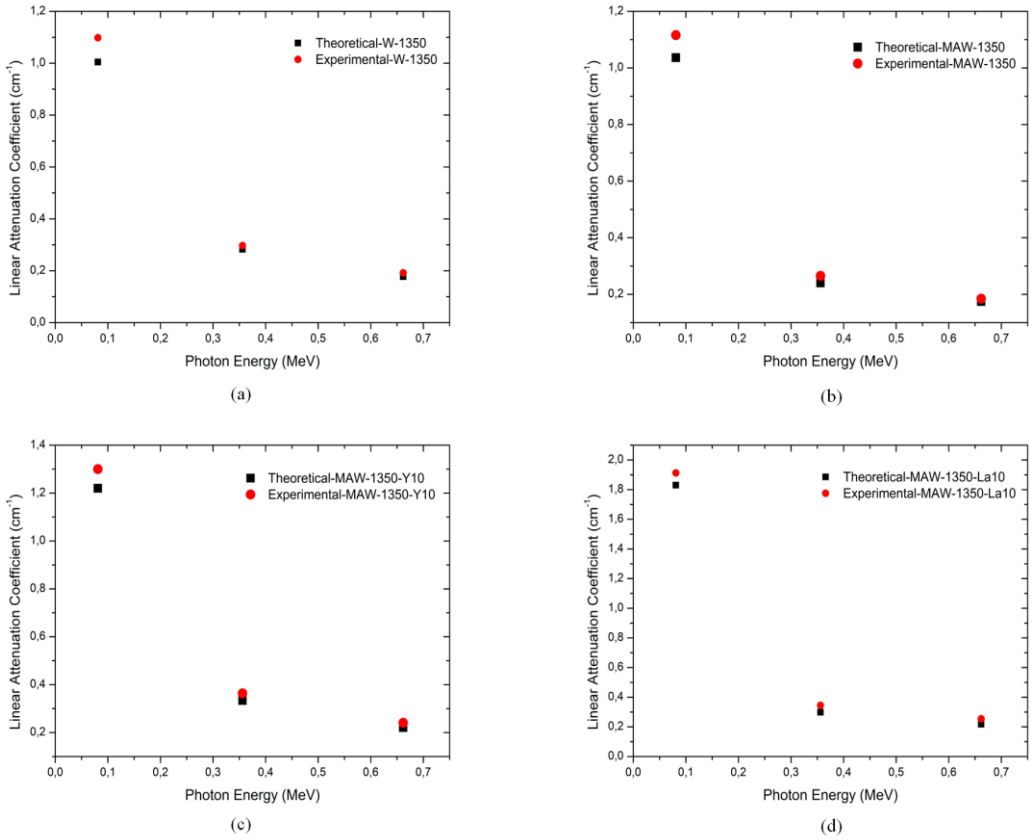


Figure 4.52 Comparative values of linear attenuation coefficients calculated with experimental and computational data. (a) W-1350, (b) MAW-1350, (c) MAW-1350-Y10 and (d) MAW-1350-La10

By using the experimental measurement results, the I/I0 and shielding percent values of the samples were also calculated and the results obtained are presented in Figure 4.54, comparatively. Against all radioactive sources, all of the samples provided shielding compared to the blank measurement. Both La and Y doped samples provided higher shielding than undoped ones at all energies. In the measurements made against the low-energy radioactive source (Ba133-1; 81 keV), W-1350, MAW-1350, MAW-1350-Y10 and MAW-1350-La10 showed 49.15, 50.02, 50.04 and 63.84% shielding, respectively.

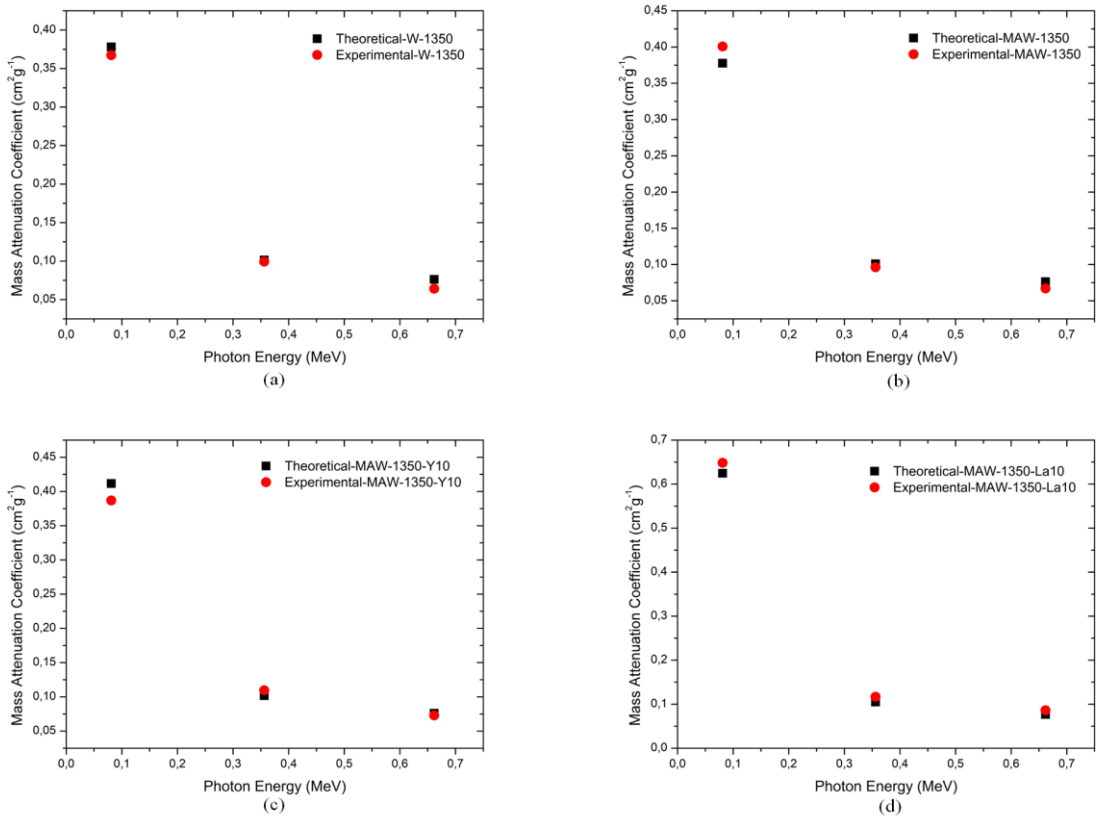


Figure 4.53 Comparative values of mass attenuation coefficients calculated with experimental and computational data. (a) W-1350, (b) MAW-1350, (c) MAW-1350-Y10 and (d) MAW-1350-La10

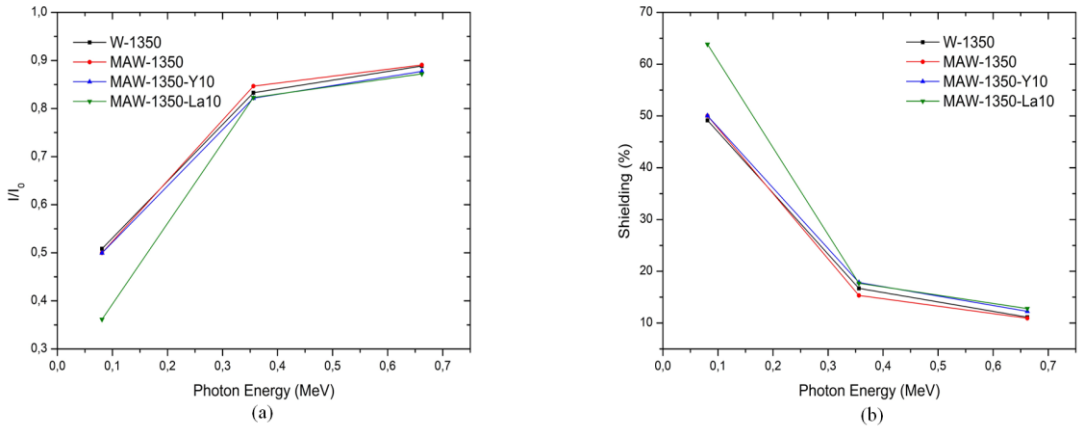


Figure 4.54 The I/I0 and shielding percent values of the samples

According to the highest energy source used in the measurements, W-1350, MAW-1350, MAW-1350-Y10 and MAW-1350-La10 samples showed 11.14, 10.93, 12.26, and 12.78 shielding, respectively.

5. CONCLUSION AND FUTURE SUGGESTIONS

In this thesis, a novel methodology has been proposed to utilize the investment casting shell waste for the production of two types of high performance ceramic composites. Firstly, large chunks of investment casting shell waste was ground into powders and its various properties such as, morphology, particle size, phase and elemental composition were characterized. XRD analysis revealed that investment casting shell waste mainly consists of mullite, silica, and zircon. Meanwhile, elemental composition determined by XRF analysis indicated that investment casting shell waste contains approximately 14.8 wt.% Al, 24.5 wt.% Si and 12.4 wt.% Zr elements. Based on the these results, two different ceramic composite systems, mullite-zirconia and cordierite-based composites were formulated. The former one required the addition of alumina into the investment casting shell waste powder to convert all the free silica from investment casting shell waste to mullite. Meanwhile, the latter one required the addition of both alumina and magnesia to convert all the free silica from investment casting shell waste to cordierite. Then, the influence of sintering temperature and various of additives on crystal phase composition, radiation shielding performance, morphology, mechanical and physico-chemical properties were investigated.

To produce mullite-zirconia composites from the investment casting shell waste powder, alumina was added with a 100:82 wt.% ratio. The added alumina reacted with the free silica from CW to increase the mullite content in the sintered bodies. Meanwhile, the influence of various additives including MgO, TiO_2 and V_2O_5 on zircon dissocation was also investigated. Among them, only MgO additive was found to be effective in promoting zircon decomposition into zirconia and silica. Therefore, a batch composition prepared with the addition of 1 wt.% MgO and sintered at three different temperatures, 1500, 1550 and 1600°C for 4 hours. The physical properties of the samples were enhanced with increasing sintering temperature. Indeed, the sample sintered at 1600°C for 4 h exhibited the comparatively better bulk density, flexural strength, and compressive strength values of 0.3%, 2.87 $g \cdot cm^{-3}$, 190, and 308 MPa, respectively. It is worth stressing that, these values are higher than most of the mullite ceramics produced from other waste materials. Furthermore, the sample sintered at 1600°C displayed greater shielding parameters than other samples, that was mainly ascribed to its higher density. Theoretical investigations demonstrated that the gamma- and neutron-shielding properties of the

CW1600-M sample are equivalent to or even better than some commonly used radiation shielding materials.

For the preperation of the cordierite-based composites, a batch composition with investment casting shell waste powder, alumina and magnesia in a 100 : 17.7 : 9.8 wt.% ratio was prepared. The added alumina and magnesia reacted with the free silica from investment casting shell waste powder to yield cordierite. Although cordierite phase formation observed for the sample sintered at 1250°C, a sintering temperature of at least 1300°C was required to consume all the free silica from investment casting shell waste to cordierite. Mechanical properties of the cordierite-based composites were enhanced with increasing sintering temperature from 1250 to 1350°C. Compared with the ceramic composites prepared solely from investment casting shell waste, cordierite-based composites demonstrated up to 6-fold enhanced flexural strength, with the MAW-1350 sample exhibiting the largest flexural strength of 47.69 MPa. Additionally, cordierite-based composites demonstrated relatively better radiation attenuation performance than ceramic composites prepared solely from investment casting shell waste. Additionally, the influence of five different sintering additives, including Bi_2O_3, La_2O_3, Y_2O_3, Ta_2O_5, and WO_3, with concentrations varying from 1 to 10 wt.% studied for cordierite-based composites. All these additives play positive roles in enhancing the densification and radiation shielding properties of the cordierite-based composites. Among them, La_2O_3 provided the best densification behavior. Considerable bulk density of 2.86 g/cm^3 and apparent porosity of 7.9% were recorded for the MAW-1350-La10 sample. Nonetheless, the use of La_2O_3 additive higher than 7 wt.% resulted in the decomposition of cordierite into mullite. Besides, the addition of La_2O_3 was also fruitful for improving mechanical strength. Flexural strength increased from about 48 MPa to 192 MPa with the increase of La_2O_5 additive from 0 to 10 wt.%. Furthermore, despite the slightly lower atomic number of lanthanum than tantalum, bismuth, and tungsten, La_2O_5 additive also provided best radiation shielding behaviour. This was because considerably greater densification of samples prepared with the La_2O_5 additive. The influence of additives on fast neutron removal cross-sections of cordierite-based composites followed the order of La_2O_3 > Ta_2O_5 > WO_3 > Bi_2O_3 > Y_2O_3. MAW-1350-La10 exhibited greatest fast neutron removal cross-section value of 0.0905, which was 55% higher than that obtained from the ceramic composite directly prepared from investment casting shell waste. Similar rates of

enhancements of experimentally determined linear and mass attenuation coefficient values have also been recorded for the MAW-1350-La10. Furthermore, despite its low density, this composite also exhibited good gamma-ray and neutron attenuation capability, comparable to some shielding materials commonly employed in nuclear applications. The results of this part of the work demonstrate the possibility of utilizing investment casting shell waste in producing lighter radiation shielding materials, with lower thickness and non-toxicity.

In conclusition, this thesis demonstrates a plausible way to utilize investment casting shell waste. Both mullite-zirconia composites and cordierite-based composites developed here exhibited comparable to or even better mechanical properties than those fabricated from other waste materials. Furthermore, as they outperformed various commonly used radiation shielding materials, they can be utilized as structural materials for shielding applications, especially when good mechanical properties are required.

Although this study provides a robust model for recycling investment casting shell waste for radiation shielding applications considering the refractory components of the developed ceramics further efforts can be devoted to exploring the refractory behavior of mullite-zircon and cordierite-mullite-zircon ceramics.

6. REFERENCES

[1] Reference Module in Materials Science and Materials Engineering, Elsevier, 2016.

[2] Xiang R, Li Y, Li S, Xue S, He Z, Ouyang S, Nana X, The potential usage of waste foundry sand from investment casting in refractory industry. Journal of Cleaner Production 2019;211:1322-27 https://doi.org/10.1016/j.jclepro.2018.11.280

[3] M.A.H. Abdullah, R.S.M. Rashid, M. Amran, F. Hejazii, N.M. Azreen, R. Fediuk, Y.L. Voo, N.I. Vatin, M.I. Idris, Recent Trends in Advanced Radiation Shielding Concrete for Construction of Facilities: Materials and Properties, Polymers 14 (2022) 2830. https://doi.org/10.3390/polym14142830.

[4] M. Asgari, H. Afarideh, H. Ghafoorifard, E.A. Amirabadi, Comparison of nano/micro lead, bismuth and tungsten on the gamma shielding properties of the flexible composites against photon in wide energy range (40 keV–662 keV), Nuclear Engineering and Technology 53 (2021) 4142–4149. https://doi.org/10.1016/j.net.2021.06.022.

[5] N.J. AbuAlRoos, N.A. Baharul Amin, R. Zainon, Conventional and new lead-free radiation shielding materials for radiation protection in nuclear medicine: A review, Radiation Physics and Chemistry 165 (2019) 108439. https://doi.org/10.1016/j.radphyschem.2019.108439.

[6] M. Kurudirek, Radiation shielding and effective atomic number studies in different types of shielding concretes, lead base and non-lead base glass systems for total electron interaction: A comparative study, 2014.

[7] B. Aygün, Neutron and gamma radiation shielding properties of high-temperature-resistant heavy concretes including chromite and wolframite, Journal of Radiation Research and Applied Sciences 12 (2019) 352–359. https://doi.org/10.1080/16878507.2019.1672312.

[8] M.I. Sayyed, G. Lakshminarayana, M.G. Dong, M.Ç. Ersundu, A.E. Ersundu, I.V. Kityk, Investigation on gamma and neutron radiation shielding parameters for BaO/SrO–Bi2O3–B2O3 glasses, Radiation Physics and Chemistry 145 (2018) 26–33. https://doi.org/10.1016/j.radphyschem.2017.12.010.

[9] W.-H. Lee, Y.-F. Wu, Y.-C. Ding, T.-W. Cheng, Fabrication of Ceramic Moulds Using Recycled Shell Powder and Sand with Geopolymer Technology in Investment Casting, Applied Sciences 10 (2020) 4577. https://doi.org/10.3390/app10134577.

[10] S. Pattnaik, D.B. Karunakar, P.K. Jha, Developments in investment casting process—A review, Journal of Materials Processing Technology 212 (2012) 2332–2348. https://doi.org/10.1016/j.jmatprotec.2012.06.003.

[11] S. Singh, R. Singh, Precision investment casting: A state of art review and future trends, Proceedings of the Institution of Mechanical Engineers, Part B: Journal of Engineering Manufacture 230 (2016) 2143–2164. https://doi.org/10.1177/0954405415597844.

[12] J.D. Booker, K.G. Swift (Eds.), Manufacturing process selection handbook, Elsevier, Amsterdam, Boston, Heidelberg [etc.], 2013.

[13] S. Singh, R. Singh, Precision investment casting: A state of art review and future trends, Proceedings of the Institution of Mechanical Engineers, Part B: Journal of Engineering Manufacture 230 (2016) 2143–2164. https://doi.org/10.1177/0954405415597844.

[14] V. N. Kaila, S. Engg, OPTIMIZATION OF CERAMIC SHELL MOLD MATERIALS IN INVESTMENT CASTING, International Journal of Research in Engineering and Technology (2014).

[15] T.M. Peters, D.L. Twarog, Feasibility of reclaiming shell material from investment castings.

[16] H. Schneider, R.X. Fischer, J. Schreuer, Mullite: Crystal Structure and Related Properties, J. Am. Ceram. Soc. 98 (2015) 2948–2967. https://doi.org/10.1111/jace.13817.

[17] A. Ripin, F. Mohamed, A. Aman, Synthesis of mullite (3Al2O32SiO2) from local kaolin for radiation shielding, AIP Conference Proceedings 1940 (2018) 20008. https://doi.org/10.1063/1.5027923.

[18] A. Ripin, F. Mohamed, T.F. Choo, M.R. Yusof, S. Hashim, S.K. Ghoshal, X-ray shielding behaviour of kaolin derived mullite-barites ceramic, Radiation Physics and Chemistry 144 (2018) 63–68. https://doi.org/10.1016/j.radphyschem.2017.11.014.

[19] A. Abdullayev, C. Avcioglu, T. Fey, A. Hilger, M. Osenberg, I. Manke, L.M. Henning, A. Gurlo, M.F. Bekheet, Fabrication and characterization of porous mullite ceramics derived from fluoride-assisted Metakaolin-Al(OH)3 annealing for filtration applications, Open Ceramics 9 (2022) 100240. https://doi.org/10.1016/j.oceram.2022.100240.

[20] A. Abdullayev, M.F. Bekheet, D.A.H. Hanaor, A. Gurlo, Materials and

Applications for Low-Cost Ceramic Membranes, Membranes 9 (2019) 105. https://doi.org/10.3390/membranes9090105.

[21] M.J. Ribeiro, D.U. Tulyagavov, J.M. Ferreira, J.A. Labrincha, High temperature mullite dissolution in ceramic bodies derived from Al-rich sludge, Journal of the European Ceramic Society 25 (2005) 703–710. https://doi.org/10.1016/j.jeurceramsoc.2004.03.028.

[22] J.S. Jung, H.C. Park, R. Stevens, Mullite ceramics derived from coal fly ash, Journal of Materials Science Letters 20 (2001) 1089–1091. https://doi.org/10.1023/A:1010934728570.

[23] Choo, M. Salleh, Kok, Matori, A Review on Synthesis of Mullite Ceramics from Industrial Wastes, Recycling 4 (2019) 39. https://doi.org/10.3390/recycling4030039.

[24] H. Tan, Preparation of mullite whiskers from coal fly ash using sodium sulfate flux, International Journal of Mineral Processing 100 (2011) 188–189. https://doi.org/10.1016/j.minpro.2011.05.008.

[25] S. Li, H. Du, A. Guo, H. Xu, D. Yang, Preparation of self-reinforcement of porous mullite ceramics through in situ synthesis of mullite whisker in flyash body, Ceramics International 38 (2012) 1027–1032. https://doi.org/10.1016/j.ceramint.2011.08.026.

[26] Y. Dong, J. Zhou, B. Lin, Y. Wang, S. Wang, L. Miao, Y. Lang, X. Liu, G. Meng, Reaction-sintered porous mineral-based mullite ceramic membrane supports made from recycled materials, Journal of Hazardous Materials 172 (2009) 180–186. https://doi.org/10.1016/j.jhazmat.2009.06.148.

[27] Y. Dong, J. Diwu, X. Feng, X. Feng, X. Liu, G. Meng, Phase evolution and sintering characteristics of porous mullite ceramics produced from the flyash-Al(OH)3 coating powders, Journal of Alloys and Compounds 460 (2008) 651–657. https://doi.org/10.1016/j.jallcom.2007.06.043.

[28] T.Y. Yang, H.B. Ji, S.Y. Yoon, B.K. Kim, H.C. Park, Porous mullite composite with controlled pore structure processed using a freeze casting of TBA-based coal fly ash slurries, Resources, Conservation and Recycling 54 (2010) 816–820. https://doi.org/10.1016/j.resconrec.2009.12.012.

[29] I.M. Martins, S. Vieira, V. Livramento, J.B. Sousa, F. Delmas, M. Oliveira, M.T. Vieira, Manufacture of Ceramic Products Using Inertized Aluminum Sludges, Advanced Materials Forum II 455-456 (2004) 822–826.

https://doi.org/10.4028/www.scientific.net/MSF.455-456.822.

[30] A. Francis, S. Vilminot, Crystallisation kinetics of mullite glass-ceramics obtained from alumina–silica wastes, International Journal of Sustainable Engineering 6 (2013) 74–81. https://doi.org/10.1080/19397038.2012.672478.

[31] F.C. Oliveira, V. Livramento, F. Delmas, Novel mullite-based ceramics manufactured from inorganic wastes, Journal of Materials Processing Technology 195 (2008) 255–259. https://doi.org/10.1016/j.jmatprotec.2007.05.010.

[32] F.C. Oliveira, V. Livramento, F. Delmas, Novel mullite-based ceramics manufactured from inorganic wastes, Journal of Materials Processing Technology 196 (2008) 101–108. https://doi.org/10.1016/j.jmatprotec.2007.05.011.

[33] H. Aripin, S. Mitsudo, E.S. Prima, I.N. Sudiana, H. Kikuchi, S. Sano, S. Sabchevski, Crystalline mullite formation from mixtures of alumina and a novel material—Silica xerogel converted from sago waste ash, Ceramics International 41 (2015) 6488–6497. https://doi.org/10.1016/j.ceramint.2015.01.092.

[34] M.F. Serra, M.S. Conconi, M.R. Gauna, G. Suárez, E.F. Aglietti, N.M. Rendtorff, Mullite (3Al 2 O 3 ·2SiO 2) ceramics obtained by reaction sintering of rice husk ash and alumina, phase evolution, sintering and microstructure, Journal of Asian Ceramic Societies 4 (2016) 61–67. https://doi.org/10.1016/j.jascer.2015.11.003.

[35] S. Sembiring, W. Simanjuntak, P. Manurung, D. Asmi, I.M. Low, Synthesis and characterisation of gel-derived mullite precursors from rice husk silica, Ceramics International 40 (2014) 7067–7072. https://doi.org/10.1016/j.ceramint.2013.12.038.

[36] T.F. Choo, J.A. Murshidi, N.U. Saidin, W. Paulus, Y. Abdullah, Production of Mullite Ceramic Bodies from Kaolin Processing Waste and Aluminum Hydroxide, Advanced Materials Forum II 888 (2017) 81–85. https://doi.org/10.4028/www.scientific.net/MSF.888.81.

[37] M. Vieira, L. Catarino, M. Oliveira, J. Sousa, J. Torralba, L. Cambronero, F. González-Mesones, A. Victoria, Optimization of the sintering process of raw material wastes, Journal of Materials Processing Technology 92-93 (1999) 97–101. https://doi.org/10.1016/S0924-0136(99)00186-7.

[38] Y. Dong, X. Feng, X. Feng, Y. Ding, X. Liu, G. Meng, Preparation of low-cost mullite ceramics from natural bauxite and industrial waste fly ash, Journal of Alloys and Compounds 460 (2008) 599–606. https://doi.org/10.1016/j.jallcom.2007.06.023.

[39] V. Viswabaskaran, F.D. Gnanam, M. Balasubramanian, Effect of MgO, Y2O3 and boehmite additives on the sintering behaviour of mullite formed from kaolinite-reactive alumina, Journal of Materials Processing Technology 142 (2003) 275–281. https://doi.org/10.1016/S0924-0136(03)00577-6.

[40] P.M. de Souto, R.R. Menezes, Kiminami, Ruth Herta Goldschmidt Aliaga, Evaluation of the Influence of MgO and La2O3 on the Fast Sintering of Mullite, Mat. Res. 18 (2015) 42–53. https://doi.org/10.1590/1516-1439.264814.

[41] U. Mücke, Ceramic microstructures. Property control by processing. von W. E. Lee und W. M. Rainforth, 590 Seiten, Zahlreiche Abbildungen, Chapman & Hall, London, Glasgow, Weinheim. New York, Tokio, Melbourne, Madras, 1994, £ 89.00, ISBN 0-412-43140-8, Materials and Corrosion 47 (1996) 346–347. https://doi.org/10.1002/maco.19960470617.

[42] M. Mizuno, Microstructure, Microchemistry, and Flexural Strength of Mullite Ceramics, Journal of the American Ceramic Society 74 (1991) 3017–3022. https://doi.org/10.1111/j.1151-2916.1991.tb04295.x.

[43] S. Prusty, D.K. Mishra, B.K. Mohapatra, S.K. Singh, Effect of MgO in the microstructure formation of zirconia mullite composites from sillimanite and zircon, Ceramics International 38 (2012) 2363–2368. https://doi.org/10.1016/j.ceramint.2011.10.089.

[44] S. Maitra, S. Pal, S. Nath, A. Pandey, R. Lodha, Role of MgO and Cr2O3 additives on the properties of zirconia–mullite composites, Ceramics International 28 (2002) 819–826. https://doi.org/10.1016/S0272-8842(02)00048-2.

[45] Y. Jing, X. Deng, J. Li, C. Bai, W. Jiang, Fabrication and properties of SiC/mullite composite porous ceramics, Ceramics International 40 (2014) 1329–1334. https://doi.org/10.1016/j.ceramint.2013.07.013.

[46] D. Ghahremani, T. Ebadzadeh, A. Maghsodipour, Densification, microstructure and mechanical properties of Mullite–TiC composites prepared by spark plasma sintering, Ceramics International 41 (2015) 1957–1962. https://doi.org/10.1016/j.ceramint.2014.07.146.

[47] H. Rajaei, M. Farvizi, I. Mobasherpour, M. Zakeri, Effect of spark plasma sintering temperature on microstructure and mechanical properties of mullite - WC composites, International Journal of Refractory Metals and Hard Materials 70 (2018)

197–201. https://doi.org/10.1016/j.ijrmhm.2017.10.012.

[48] S. Itoh, Y. Hirata, T. Shimonosono, S. Sameshima, Theoretical and experimental analyses of thermal conductivity of the alumina–mullite system, Journal of the European Ceramic Society 35 (2015) 605–612. https://doi.org/10.1016/j.jeurceramsoc.2014.09.034.

[49] O. Ertugrul, R. Dalmis, S. Akpinar, I.M. Kusoglu, E. Celik, Influence of zircon particle size on conventional and microwave assisted reaction sintering of in-situ mullite–zirconia composites, Ceramics International 42 (2016) 11104–11117. https://doi.org/10.1016/j.ceramint.2016.04.016.

[50] E. ghasali, E.K. Saeidabadi, M. alizadeh, A. Fazili, H. Rajaei, A. Jam, H. Kazemzadeh, T. Ebadzadeh, Preparation of mullite/B4C composites: A comparative study on the effect of heating methods, Ceramics International 44 (2018) 18743–18751. https://doi.org/10.1016/j.ceramint.2018.07.104.

[51] F. Sahnoune, N. Saheb, Mechanical behavior of mullite-zirconia composites, EPJ Web of Conferences 6 (2010) 20005. https://doi.org/10.1051/epjconf/20100620005.

[52] B.L. Mitra, N.C. Biswas, P.S. Aggarwal, Zirconia-mullite ceramics by reaction-sintering, Bull. Mater. Sci. 12 (1989) 457–460. https://doi.org/10.1007/BF02744914.

[53] L. Tiwari, S. Mishra, D. Kumar, R.K. Sinha, Reaction Sintering Behaviour of Alumina-Zircon System, Transactions of the Indian Ceramic Society 60 (2001) 130–136. https://doi.org/10.1080/0371750X.2001.10799986.

[54] A. Kaiser, M. Lobert, R. Telle, Thermal stability of zircon (ZrSiO4), Journal of the European Ceramic Society 28 (2008) 2199–2211. https://doi.org/10.1016/j.jeurceramsoc.2007.12.040.

[55] G.G. Kenny, M.A. Pasek, The response of zircon to the extreme pressures and temperatures of a lightning strike, Sci Rep 11 (2021) 1560. https://doi.org/10.1038/s41598-021-81043-8.

[56] W. Burger, G. Kiefer, Alumina, Zirconia and Their Composite Ceramics with Properties Tailored for Medical Applications, J. Compos. Sci. 5 (2021) 306. https://doi.org/10.3390/jcs5110306.

[57] Effect of Minor Additives on Sintering of Zircon, Journal of the Korean Ceramic Society 15 3.

[58] L.B. Garrido, E.F. Aglietti, L. Martorello, M.A. Camerucci, A.L. Cavalieri,

Hardness and fracture toughness of mullite–zirconia composites obtained by slip casting, Materials Science and Engineering: A 419 (2006) 290–296. https://doi.org/10.1016/j.msea.2006.01.035.

[59] H. OHSATO, J.-S. KIM, C.-I. CHEON, I. KAGOMIYA, Millimeter-wave dielectrics of indialite/cordierite glass ceramics: Estimating Si/Al ordering by volume and covalency of Si/Al octahedron, J. Ceram. Soc. Japan 121 (2013) 649–654. https://doi.org/10.2109/jcersj2.121.649.

[60] Y. Kobayashi, M. Katayama, M. Kato, S. Kuramochi, Effect of Microstructure on the Thermal Expansion Coefficient of Sintered Cordierite Prepared from Sol Mixtures, J. Am. Ceram. Soc. 96 (2013) 1863–1868. https://doi.org/10.1111/jace.12195.

[61] D. Kuscer, I. Bantan, M. Hrovat, B. Malič, The microstructure, coefficient of thermal expansion and flexural strength of cordierite ceramics prepared from alumina with different particle sizes, Journal of the European Ceramic Society 37 (2017) 739–746. https://doi.org/10.1016/j.jeurceramsoc.2016.08.032.

[62] M. Valášková, Clays, clay minerals and cordierite ceramics - a review (2015).

[63] Q. Hou, X. Luo, X. Liu, Z. Xie, Preparation of cordierite powder by chemical coprecipitation–rotation evaporation and solid reaction sintering, J Aust Ceram Soc 56 (2020) 1575–1582. https://doi.org/10.1007/s41779-020-00496-8.

[64] A. Aşkın, İ. Tatar, Ş. Kılınç, Ö. Tezel, The Utilization of Waste Magnesite in the Production of the Cordierite Ceramic, Energy Procedia 107 (2017) 137–143. https://doi.org/10.1016/j.egypro.2016.12.151.

[65] E.P. de Almeida, I.P. de Brito, H.C. Ferreira, H.d.L. Lira, L.N. de Lima Santana, G. de Araújo Neves, Cordierite obtained from compositions containing kaolin waste, talc and magnesium oxide, Ceramics International 44 (2018) 1719–1725. https://doi.org/10.1016/j.ceramint.2017.10.102.

[66] H. Hajjou, L. Saâdi, M. Waqif, Synthesis of cordierite using industrial waste fly ash, Arab J Geosci 10 (2017) 1–9. https://doi.org/10.1007/s12517-017-3156-0.

[67] R.M. Khattab, H.H. Abo-Almaged, N.A. Ajiba, H.A. Badr, A.A. Gaber, M.A. Taha, H. Sadek, Sintering, physicomechanical, thermal expansion and microstructure properties of cordierite ceramics based on utilizing silica fume waste, Materials Chemistry and Physics 270 (2021) 124829. https://doi.org/10.1016/j.matchemphys.2021.124829.

[68] S. Wang, H. Wang, Z. Chen, R. Ji, L. Liu, X. Wang, Fabrication and characterization of porous cordierite ceramics prepared from fly ash and natural minerals, Ceramics International 45 (2019) 18306–18314. https://doi.org/10.1016/j.ceramint.2019.06.043.

[69] N. Obradović, N. Đorđević, S. Filipović, N. Nikolić, D. Kosanović, M. Mitrić, S. Marković, V. Pavlović, Influence of mechanochemical activation on the sintering of cordierite ceramics in the presence of Bi2O3 as a functional additive, Powder Technology 218 (2012) 157–161. https://doi.org/10.1016/j.powtec.2011.12.012.

[70] S. Wang, H. Wang, Z. Chen, R. Ji, L. Liu, X. Wang, Fabrication and characterization of porous cordierite ceramics prepared from fly ash and natural minerals, Ceramics International 45 (2019) 18306–18314. https://doi.org/10.1016/j.ceramint.2019.06.043.

[71] Z.M. Shi, Sintering Additives to Eliminate Interphases in Cordierite Ceramics, Journal of the American Ceramic Society 88 (2005) 1297–1301. https://doi.org/10.1111/j.1551-2916.2005.00287.x.

[72] S. Wu, K. Song, P. Liu, H. Lin, F. Zhang, P. Zheng, H. Qin, Effect of TiO 2 Doping on the Structure and Microwave Dielectric Properties of Cordierite Ceramics, J. Am. Ceram. Soc. 98 (2015) 1842–1847. https://doi.org/10.1111/jace.13549.

[73] J.-M. Wu, S.-P. Hwang, Effects of (B2O3, P2O5) Additives on Microstructural Development and Phase-Transformation Kinetics of Stoichiometric Cordierite Glasses, Journal of the American Ceramic Society 83 (2000) 1259–1265. https://doi.org/10.1111/j.1151-2916.2000.tb01364.x.

[74] R. Xiang, Y. Li, S. Li, Y. Li, S. Sang, Effect of Excess Magnesia on the Preparation of Cordierite Based on Waste Foundry Sand, Int. J. Appl. Ceram. Technol. 13 (2016) 603–608. https://doi.org/10.1111/ijac.12509.

[75] Z. Sun, J. Yu, H. Zhao, S. Sang, H. Zhang, Effects of partial substitution of calcium alumino-titanate on the properties and microstructure of mullite–cordierite composites, Ceramics International 48 (2022) 36056–36065. https://doi.org/10.1016/j.ceramint.2022.08.034.

[76] F.A. Costa Oliveira, J.A. Franco, J. Cruz Fernandes, D. Dias, Newly developed cordierite–zircon composites, British Ceramic Transactions 101 (2002) 14–21. https://doi.org/10.1179/096797801225000815.

[77] V.K. Marghussian, O. Balazadegan, B. Eftekhari-yekta, Crystallization behaviour, microstructure and mechanical properties of cordierite–mullite glass ceramics, Journal of Alloys and Compounds 484 (2009) 902–906. https://doi.org/10.1016/j.jallcom.2009.05.080.

[78] R.M. Khattab, A.M. EL-Rafei, M.F. Zawrah, In situ formation of sintered cordierite–mullite nano–micro composites by utilizing of waste silica fume, Materials Research Bulletin 47 (2012) 2662–2667. https://doi.org/10.1016/j.materresbull.2012.04.036.

[79] I.P. Brito, E.P. Almeida, G. Araújo Neves, H. Lucena Lira, R.R. Menezes, V.J. Silva, L.N. Lima Santana, Development of cordierite/mullite composites using industrial wastes, International Journal of Applied Ceramic Technology 18 (2021) 253–261. https://doi.org/10.1111/ijac.13622.

[80] I.P. Brito, E.P. Almeida, G. Araújo Neves, H. Lucena Lira, R.R. Menezes, V.J. Silva, L.N. Lima Santana, Development of cordierite/mullite composites using industrial wastes, Int. J. Appl. Ceram. Technol. 18 (2021) 253–261. https://doi.org/10.1111/ijac.13622.

[81] E. Şakar, Ö.F. Özpolat, B. Alım, M.I. Sayyed, M. Kurudirek, Phy-X / PSD: Development of a user friendly online software for calculation of parameters relevant to radiation shielding and dosimetry, Radiation Physics and Chemistry 166 (2020) 108496. https://doi.org/10.1016/j.radphyschem.2019.108496.

[82] F.C. Hila, A. Asuncion-Astronomo, C.A.M. Dingle, J.F.M. Jecong, A.M.V. Javier-Hila, M.B.Z. Gili, C.V. Balderas, G.E.P. Lopez, N.R.D. Guillermo, A.V. Amorsolo, EpiXS: A Windows-based program for photon attenuation, dosimetry and shielding based on EPICS2017 (ENDF/B-VIII) and EPDL97 (ENDF/B-VI.8), Radiation Physics and Chemistry 182 (2021) 109331. https://doi.org/10.1016/j.radphyschem.2020.109331.

[83] M. Bozkurt, N. Şahin, Y. Karabul, M. Kılıç, Z.G. Özdemir, Radiation shielding performances of Na2SiO3 based low-cost micro and nano composites for diagnostic imaging, Progress in Nuclear Energy 143 (2022) 104058. https://doi.org/10.1016/j.pnucene.2021.104058.

[84] R.S. Pavlik, H.J. Holland, E.A. Payzant, Thermal Decomposition of Zircon Refractories, Journal of the American Ceramic Society 84 (2001) 2930–2936.

https://doi.org/10.1111/j.1151-2916.2001.tb01117.x.

[85] E.-M. Köck, M. Kogler, T. Götsch, L. Schlicker, M.F. Bekheet, A. Doran, A. Gurlo, B. Klötzer, B. Petermüller, D. Schildhammer, N. Yigit, S. Penner, Surface chemistry of pure tetragonal ZrO2 and gas-phase dependence of the tetragonal-to-monoclinic ZrO2 transformation, Dalton Trans. 46 (2017) 4554–4570. https://doi.org/10.1039/C6DT04847A.

[86] D.L. PORTER, A.H. HEUER, Microstructural Development in MgO-Partially Stabilized Zirconia (Mg-PSZ), J American Ceramic Society 62 (1979) 298–305. https://doi.org/10.1111/j.1151-2916.1979.tb09484.x.

[87] P. Suhasinee Behera, S. Bhattacharyya, Sintering and microstructural study of mullite prepared from kaolinite and reactive alumina: Effect of MgO and TiO 2, Int. J. Appl. Ceram. Technol. 18 (2021) 81–90. https://doi.org/10.1111/ijac.13637.

[88] C.S. Huang, J.C. Liu, A.R. Guo, L. Yang, Di Song, Effects of SiO2 and Fe2O3 on Morphological of Mullite, High-Performance Ceramics VI 434-435 (2010) 64–65. https://doi.org/10.4028/www.scientific.net/KEM.434-435.64.

[89] D. Glymond, M.J. Vick, F. Giuliani, L.J. Vandeperre, High-temperature fracture toughness of mullite with monoclinic zirconia, Journal of the American Ceramic Society 100 (2017) 1570–1577. https://doi.org/10.1111/jace.14637.

[90] C. Mochales, A. Maerten, A. Rack, P. Cloetens, W.D. Mueller, P. Zaslansky, C. Fleck, Monoclinic phase transformations of zirconia-based dental prostheses, induced by clinically practised surface manipulations, Acta biomaterialia 7 (2011) 2994–3002. https://doi.org/10.1016/j.actbio.2011.04.007.

[91] M. Rühle, A.G. Evans, R.M. McMeeking, P.G. Charalambides, J.W. Hutchinson, Microcrack toughening in alumina/zirconia, Acta Metallurgica 35 (1987) 2701–2710. https://doi.org/10.1016/0001-6160(87)90269-0.

[92] X. Zhu, L. Chen, F. Zhao, J. Gao, K. Li, X. Liu, E. Xu, T. Ge, L. Yang, A novel strategy to fabricate high-strength mullite by the reaction sintering method using Al3+/Ce4+-doped SiO2, Ceramics International 47 (2021) 13129–13138. https://doi.org/10.1016/j.ceramint.2021.01.177.

[93] J.S. Jung, H.C. Park, R. Stevens, Mullite ceramics derived from coal fly ash, Journal of Materials Science Letters 20 (2001) 1089–1091. https://doi.org/10.1023/A:1010934728570.

[94] J.-H. Li, H.-W. Ma, W.-H. Huang, Effect of V2O5 on the properties of mullite ceramics synthesized from high-aluminum fly ash and bauxite, Journal of Hazardous Materials 166 (2009) 1535–1539. https://doi.org/10.1016/j.jhazmat.2008.11.059.

[95] J. Cao, X. Dong, L. Li, Y. Dong, S. Hampshire, Recycling of waste fly ash for production of porous mullite ceramic membrane supports with increased porosity, Journal of the European Ceramic Society 34 (2014) 3181–3194. https://doi.org/10.1016/j.jeurceramsoc.2014.04.011.

[96] A.I. Abdallah, M. Sayed, M. Awaad, A.H.E. Yousif, S.M. Naga, Characterization of in-situ zirconia/mullite composites prepared by sol-gel technique, Journal of Asian Ceramic Societies (2021) 1–7. https://doi.org/10.1080/21870764.2021.1929738.

[97] R.M. Khattab, A.M. EL-Rafei, M.F. Zawrah, In situ formation of sintered cordierite–mullite nano–micro composites by utilizing of waste silica fume, Materials Research Bulletin 47 (2012) 2662–2667. https://doi.org/10.1016/j.materresbull.2012.04.036.

[98] B. Lin, S. Li, X. Hou, H. Li, Preparation of high performance mullite ceramics from high-aluminum fly ash by an effective method, Journal of Alloys and Compounds 623 (2015) 359–361. https://doi.org/10.1016/j.jallcom.2014.11.023.

[99] G. Sedmale, I. Sperberga, N. Zilinska, I. Steins, Spark Plasma Sintering (SPS) to the Mullite –Zirconia Ceramics Development, ms 21 (2015) 96–99. https://doi.org/10.5755/j01.ms.21.1.5501.

[100] School of High Temperature Materials and Magnesium Resource Engineering, University of Science and Technology Liaoning, Anshan 114051, China, State Key Laboratory of New Ceramics and Fine Processing, School of Materials Science and Engineering, Tsinghua University, Beijing 100084, China, Zirconia-Mullite Obtained from Co-Precipitated Zirconia-Mullite Composite Powders by SPS, Journal of Ceramic Science and Technology 7 (2016) 417–422.

[101] K. Hemra, P. Aungkavattana, Effect of zirconia content on mechanical and thermal properties of mullite–zirconia composite, Advances in Applied Ceramics 113 (2014) 323–327. https://doi.org/10.1179/1743676114Y.0000000164.

[102] N.M. Rendtorff, L.B. Garrido, E.F. Aglietti, Zirconia toughening of mullite–zirconia–zircon composites obtained by direct sintering, Ceramics International 36 (2010) 781–788. https://doi.org/10.1016/j.ceramint.2009.11.010.

[103] P. KUMAR, M. NATH, A. GHOSH, H.S. TRIPATHI, Synthesis and characterization of mullite–zirconia composites by reaction sintering of zircon flour and sillimanite beach sand, Bull Mater Sci 38 (2015) 1539–1544. https://doi.org/10.1007/s12034-015-0890-3.

[104] D.H.A. Besisa, E.M.M. Ewais, Investigation of mechanical strength of the functionally graded zirconia-mullite/alumina ceramics tailored for high temperature applications, Mater. Res. Express 6 (2019) 75516. https://doi.org/10.1088/2053-1591/ab177e.

[105] N.M. Rendtorff, L.B. Garrido, E.F. Aglietti, Mechanical and fracture properties of zircon–mullite composites obtained by direct sintering, Ceramics International 35 (2009) 2907–2913. https://doi.org/10.1016/j.ceramint.2009.03.040.

[106] H. Yu, Y. Chen, X. Guo, L. Luo, J. Li, W. Li, Z. Xu, T. Li, G. Wu, Study on mechanical properties of hot pressing sintered mullite-ZrO2 composites with finite element method, Ceramics International 44 (2018) 7509–7514. https://doi.org/10.1016/j.ceramint.2018.01.146.

[107] X. Chen, L. Luo, L. Liu, J. Li, H. Yu, W. Li, Y. Chen, Microstructure and mechanical properties of hot-pressed Al2O3–mullite–ZrO2–SiC composites, Materials Science and Engineering: A 740-741 (2019) 390–397. https://doi.org/10.1016/j.msea.2018.10.118.

[108] E.B. Podgoršak, Interactions of Photons with Matter, in: Radiation Physics for Medical Physicists, Springer, Berlin, Heidelberg, 2009, pp. 277–375.

[109] S. Avcıoğlu, M. Buldu, F. Kaya, C.B. Üstündağ, E. Kam, Y.Z. Menceloğlu, H.Y. Kaptan, C. Kaya, Processing and properties of boron carbide (B4C) reinforced LDPE composites for radiation shielding, Ceramics International 46 (2020) 343–352. https://doi.org/10.1016/j.ceramint.2019.08.268.

[110] S. Avcıoğlu, M. Buldu, F. Kaya, C. Kaya, Chapter 20 - Synthesis of nuclear-grade nano-sized boron carbide powders and its application in LDPE matrix composites for neutron shielding, in: I.-M. Low, Y. Dong (Eds.), Composite materials manufacturing, properties and applications, Elsevier, uuuu-uuuu, pp. 543–579.

[111] S. Chen, M. Bourham, A. Rabiei, Applications of Open-cell and Closed-cell Metal Foams for Radiation Shielding, Procedia Materials Science 4 (2014) 293–298. https://doi.org/10.1016/j.mspro.2014.07.560.

[112] E. Şakar, Ö.F. Özpolat, B. Alım, M.I. Sayyed, M. Kurudirek, Phy-X / PSD: Development of a user friendly online software for calculation of parameters relevant to radiation shielding and dosimetry, Radiation Physics and Chemistry 166 (2020) 108496. https://doi.org/10.1016/j.radphyschem.2019.108496.

[113] M.I. Sayyed, M.Y. AlZaatreh, M.G. Dong, M. Zaid, K.A. Matori, H.O. Tekin, A comprehensive study of the energy absorption and exposure buildup factors of different bricks for gamma-rays shielding, Results in Physics 7 (2017) 2528–2533. https://doi.org/10.1016/j.rinp.2017.07.028.

[114] S. AVCIOĞLU, LDPE matrix composites reinforced with dysprosium-boron containing compounds for radiation shielding applications, Journal of Alloys and Compounds 927 (2022) 166900. https://doi.org/10.1016/j.jallcom.2022.166900.

[115] E. Ilik, E. Kavaz, G. Kilic, S.A. Issa, H.M. Zakaly, H.O. Tekin, A closer-look on Copper(II) oxide reinforced Calcium-Borate glasses: Fabrication and multiple experimental assessment on optical, structural, physical, and experimental neutron/gamma shielding properties, Ceramics International 48 (2022) 6780–6791. https://doi.org/10.1016/j.ceramint.2021.11.229.

[116] O.I. Sallam, A.M. Madbouly, N.L. Moussa, A. Abdel-Galil, Impact of radiation on CoO-doped borate glass: lead-free radiation shielding, Appl. Phys. A 128 (2022) 1–16. https://doi.org/10.1007/s00339-021-05190-5.

[117] X. Xu, Y. Zhang, J. Wu, C. Hu, Z. Tang, Preparation and performance study of cordierite/mullite composite ceramics for solar thermal energy storage, Int. J. Appl. Ceram. Technol. 14 (2017) 162–172. https://doi.org/10.1111/ijac.12626.

CURRICULUM VITAE

Celal AVCIOĞLU

EXPERIENCE

05.2017-On Hold **Academic/Lecturer**
Usak University, Turkey

- Ceramic Research and Application Center
- Scientific Research Projects Unit

EDUCATION PROFILE

2011 **Bachelor of Science in Ceramic Engineering**
Dumlupınar University, Turkey

Two semesters abroad at the AGH University of Science and Technology (Faculty of Materials Science and Ceramics) (ERASMUS) Krakow, Poland.

2014 **Master of Science in Metallurgical and Materials Engineering, Ceramics Program, Istanbul Technical University, Turkey**

2014 **Associate Degree in Foreign Trade and Marketing**
Anadolu University, Turkey

2017 **Bachelor of Business Administration**
Anadolu University, Turkey

SEMINARS & CERTIFICATIONS

- **Ceramic Coatings**
  University of British Columbia

- **Applied Entrepreneurship Training Certificate**
  Kosgeb

- **Participation in Erasmus Program Operation for Improving Adaptability of Employers and Employees in TR33 Region**
  Zaferin

PUBLICATIONS

- C. Avcıoğlu, S. Avcıoğlu, M. Bekheet, A. Gurlo**, Photocatalytic Overall Water Splitting by SrTiO3: Progress Report and Design Strategies**, ACS Applied Energy Materials, https://doi.org/10.1021/acsaem.2c03280, 2023

- C. Avcıoğlu, S. Avcıoğlu, M. Bekheet, A. Gurlo**, Solar Hydrogen Generation using Niobium-based Photocatalysts: Design Strategies, Progress, and Challenges**, Materials Today Energy, 24(38):100936, 2022

- A. Abdullayev, C. Avcioglu, T. Fey, A. Hilger, M. Osenberg, I. Manke, L. Henning, A. Gurlo, M. Bekheet, **Fabrication and characterization of porous mullite ceramics derived from fluoride-assisted Metakaolin-Al(OH)3 annealing for filtration applications,** Open Ceramics, (9) 100240, 2022

- LH Poudeh, C Avcioglu, S Duman, B Özkal, **Preparation and Characterization of Ceramic Oxide Granules by Spray Drying Technique,** Indian Journal of Engineering and Materials Sciences, 26 (1), 2020

- C Avcioglu, B Özkal**, Study on the Granulation Behavior of TiO_2-PVA Composite Powders Prepared Via Spray Drying Technique,** Journal of the Korean Ceramic Society 56 (5), 2019

- S Ozeskici, C Avcioglu, M Nükte, **Experimental Ceramic Tile Design and Implementation by Inkjet Digital Printing Technology** Dumlupınar University Journal of Social Sciences, Special Issue, 67-80, 2019

CONFERENCES

- **The Effect of Transition Metal Oxides on Anatase-Rutile Phase Transformation of Titanium Dioxide,** ISMSIT2017

- **Effects of Granulation on the Processing of TiO_2 Ceramics,** ICTE 2017

- **A review of Hydrogen Production by Photocatalytic Water Splitting Using TiO_2,** IMSMATEC 2018

- **Nanostructured systems for Hydrogen Storage Applications, International Conference on Energy and Thermal Engineering,** IMSMATEC 2018

- **Tailoring the morphology of $SrSnO_3$ crystals by flux method for solar energy conversion,** IWAM 2020

SCHOLARSHIPS & AWARDS

- **Selection & Placement of Students to be sent abroad for post graduate studies (YLSY)**
  Turkish Ministry of National Education

- **Erasmus Program**
  AGH University-Krakow/Poland

- **Travel Grand**
  For IWAM 2020, materials science conference organised in Dubai/UAE.